MEMS based solutions for magnetless RF nonreciprocal circuits

A thesis presented by

Giuseppe Michetti

Matricola 859101

For the Master Degree in Electronics Engineering

POLITECNICO
DI MILANO

Dipartimento di Elettronica, Informazione e Bioingegneria,
Politecnico di Milano, 25 Luglio 2018

Relatori:
Prof. Giacomo Langfelder, Politecnico di Milano
Prof. Matteo Rinaldi, Northeastern University

Index

Introduction

Motivation

This work presents a research conducted on a novel class of nonreciprocal circuits based on *Linear Periodically Time Variant networks* (LPTV) which exhibit nonreciprocal functionalities at RF. They are all based on the recently-introduced *Angular Momentum Bias* (AMB) concept, which ultimately aims at mimicking micro scale magnetic resonances typical of ferromagnetic materials through a time varying resonant loops coupling.

All of these features may enable a new generation of VLSI-compatible nonreciprocal components, which might have a role into the development of 5G communication networks. At the same time the strongly nonlinear behaviour of the circuit constitutes a very interesting case study, where classic Linear Time Invariant (LTI) circuit limits can be overcome. Modeling the response of circuits is still a partially open question and their full potentialities might still be hidden.

Moreover, as will become evident throughout the discussion, the performances required by these classes of circuit are hardly compatible with lumped components.
As the frequencies of operations scale to higher and higher values, multi-physical design domains are required: in particular the use of RF Micro Electro Mechanical Systems (MEMS) Piezoelectric Resonators is highly desirable for these applications.
Among the advantages of using MEMS resonators, this application benefits of their high Quality(Q) Factors, of the planar lithographic tunability of some modes of vibration and the use of piezoelectric materials such as AlN, which can be integrated with CMOS processes.

Generalities on nonreciprocal circuits

Nonreciprocal circuits can be defined as a class of N-port networks with the main function of transferring signals from a port to the other according to their *direction of propagation*. These kinds of network are ubiquitous in optical [1] and electrical [2] domain.
The most popular devices based on reciprocal components are the *isolator*, which is a 2 port device, and the *circulator*, which is a multi-port device (usually 3 or 4). A graphic representation of both is proposed in Fig. A.

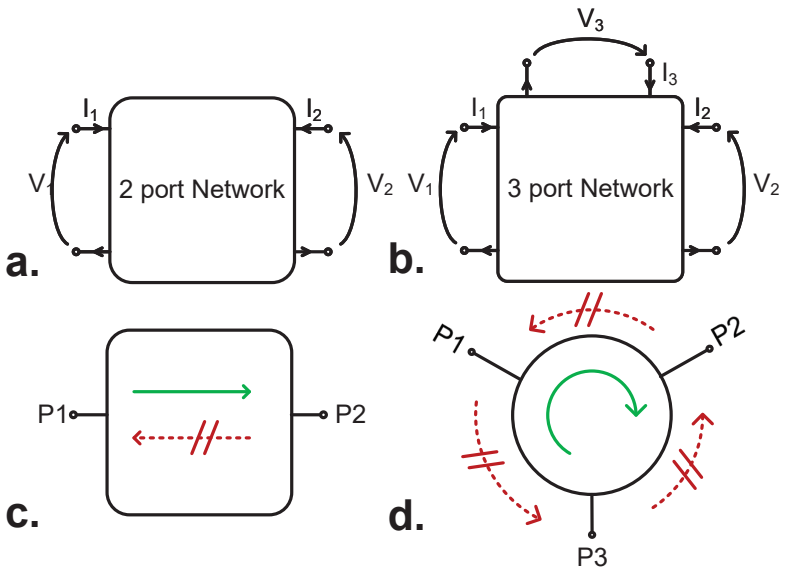

Fig. A: *Electrical two port networks (**a**) and three port networks (**b**) can operate respectively as an isolator (**c**) or as a circulator (**b**). In an isolator (**a**,**c**) a signal incoming from P1 propagates to P2, but a signal incoming from P2 is not propagated back to P1. Similarly, in an circulator (**b**,**d**) a signal incoming from P1 is transferred to P2, a signal instead incoming from P2 is transferred to P3 and so on.*

Applications for isolators can be found in testing apparatus, where sensitive signal sources or references might be affected by D.U.T mismatches: in this case an isolator prevents damages and ensures correct measurements. Moreover, an isolator would be desirable at the output of Power Amplifiers (PA) , where environment induced load mismatch could lead to overheating and reduced efficiency: an isolator would guarantee a stable termination, and so a stable operation.

Circulators, on the other hand, are desirable in Radio Frequency (RF) communication systems: they are typically used to route strong RF signals from the transmitter to the antenna (typical values range from 20 to 30dBm), and to route faint signals from the antenna to the receiver (typical values here range from -80dBm to -90dBm). In this way a single

antenna can be shared to simultaneously transmit and receive RF signals (Fig. B) without using switches or duplexers, that inherently decreases spectral efficiency, bit-rate and losses of RF systems ([3]).
The introduction of *integrated circulators* could pave the way for a new communication protocol,the so-called *Full Duplex* radio paradigm ([4]), where the same frequency could be used to transmit and receive at the same time (Signal Transmit And Receive (STAR) paradigm).
In this communication scheme neither time multiplexing or frequency multiplexing are required, and spectral efficiency would be doubled just by introducing a nonreciprocal device such as a circulator.
However, as explained in [4], tight constraints in terms of self interference cancellation and distortion are required by this communication protocol, so both analog and digital compensation techniques are required ([5]). The circulator would be a crucial component in the analog domain of cancellation of leakage signals from the Power Ampifier to the Low Noise Amplifier (Fig. B).

Other applications worth mentioning are mobile ranging sensors such as radars ([6]), where the chance of routing the reflected signal to a different path would improve the range sensitivity, and similarly to isolators, it could be used to reduce load-mismatch induced nonidealities in PAs.

Schematics for these simple yet appealing networks can be found in Fig. B.

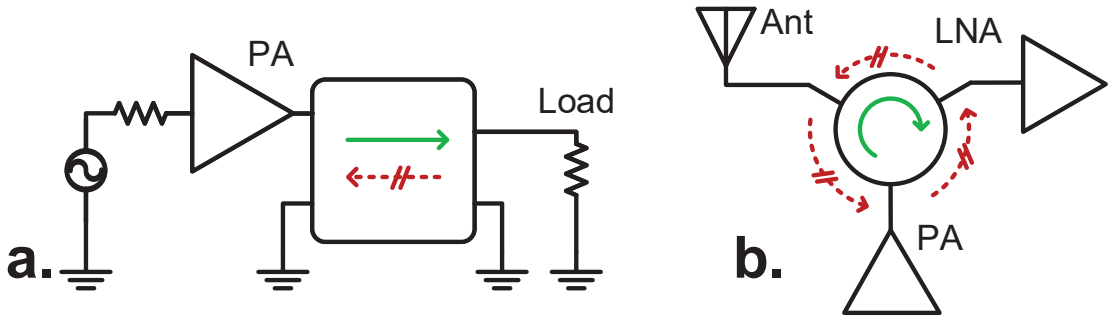

Fig. B: *Application for nonreciprocal devices: an isolator (**a**) prevents reflected signal from a load to go back to the signal source. A circulator instead (**b**), routes signals from the antenna(Ant) to the receiver (LNA) and from the transmitter (PA) to the antenna, so that it can be shared between the two components with no interference.*

Background analysis of nonreciprocal circuits

A full N-port network approach to isolators and circulators can be expressed from an *input/output* point of view thanks to the comprehensive *scattering matrix* representation (referred herefrom as *S-matrix*, or *S-parameters* as the elements of the matrix).

The ideal S-parameters matrix for both components is here reported:

$$S_{isolator} = \begin{bmatrix} 0 & 1 \\ 0 & 0 \end{bmatrix}$$
$$S_{circulator} = \begin{bmatrix} 0 & 1 & 0 \\ 0 & 0 & 1 \\ 1 & 0 & 0 \end{bmatrix} \quad (1)$$

From the S matrix, one can see the asymmetry of this system: for the circulator in Eq. 1, $S_{21} = 1$, which means that an electric signal incoming from *port 1* would have unitary transmission towards *port 2*, and $S_{12} = 0$, which means that an electric signal incoming from *port 2* would have no transmission towards *port 1* but an unitary transmission towards *port 3* ($S_{32} = 1$).

It is not hard to argue at this point that for a system to have this kind of response, some of the common hypothesis of linear passive circuits have to be removed.
These considerations can be done resorting to a fundamental and generic network analysis in the electrical domain ([7, chap.4]).
In fact, some very generic characteristics of these networks can be shown in terms of the *scattering parameters* (S-parameters) of an N-port network.

Specifically, by applying Maxwell's equations and energy conservation theorems under the hypothesis of a *linear* medium with no *inner sources* and no *dissipative* elements, it can be proved that:

$$Y_{i,j} = Y_{j,i} \qquad \text{for i} \neq j \qquad (2a)$$
$$Re\{Y_{m,n}\} = 0 \qquad \text{for any m,n} \qquad (2b)$$

Of course both equations might have been written in the impedance form without loss of generality.

Furthermore, using the relation between S-parameters and Z-parameters

$$\overline{S} = \frac{(\overline{Z^*} - Z_0)}{(\overline{Z^*} + Z_0)}$$

it is possible to derive an compact set of equations in terms of S-parameters:

$$S_{i,j} = S_{j,i} \qquad \text{for i} \neq j \tag{3a}$$

$$\sum_{j=1}^{N} S_{j,i} = 1 \qquad \text{for each i}^{\text{th}} \text{ port} \tag{3b}$$

Eq. 3a is the mathematical proof that under these conditions the transmission *cannot* be nonreciprocal. Eq. 3b is a rearrangement of the energy conservation in terms of S-parameters: the sum of reflected power and transmitted power in a system without losses must not be different than the input power.

The consequences of Eq. 3 is that it is not possible to build a nonreciprocal circuit *at the same time* lossless, passive and linear.

For these reasons, one of these three hypotheses must be removed when trying to implement such a functionality, increasing the design complexity and the trade-off limits when assessing the performances of such systems.

Nonreciprocal devices technologies

Some of the most popular solutions explored so far to break the limits imposed by energy conservation include :

(a) The use of ferromagnetic materials.

(b) The use of active devices such as transistors.

Solution (a) is widely adopted in a number of commercial applications, based on a very mature technology and in an advanced stage of research. However these components can be realistically employed only in applications such as base stations, testing laboratories and all the applications where area and volume occupation is not a concern: these devices have bulky magnetic materials at the cores of operations, which are essentially incompatible with mobile devices, small sensors and all the communication applications where a small footprint is required. Moreover, the integration of magnetic materials in CMOS processes is still under preliminary research stage [8].

Solution (b) has been investigated in the past [9], due to the huge development of CMOS technologies in the communication spectrum and the industry appeal to miniaturize these devices, so to make them available to the tool set of electrical engineers in Very Large Scale of Integration (VLSI) technologies.
In spite of good overall S-parameters performances, these class of circuits suffer from the typical CMOS trade-offs between power consumption and noise figure [10], as well as the one between area consumption and linearity, thus limiting the practical use of these devices in integrated RF front ends.

The growing interest in nonreciprocal functionalities based on time-variant networks ([11–14]) can be explained as follows:

- They make no use of ferromagnetic materials or DC biased magnetic materials. This makes these networks potential candidates as integrated circuits.
- They make no use of DC biased CMOS transistors working as transconductors. This breaks the limits of CMOS based circulator in terms of power consumption and noise figure (described e.g. in [10]), making them appealing in low power RF transceivers.
- They exploit *parametric* nonlinearities in order to induce nonreciprocity on a bandwidth proportional to the resonator one.
- The frequency of operation is potentially scalable up to millimeter waves [13] when using MEMS resonators ([15]).

This work has been divided in the following way:

Chapter 1 introduces the Angular Momentum Bias (AMB) circuit, from the first physical picture to the current implementations. The original derivation is reported, commented in detail and the practical circuit nonidealities are reported. Specifically the need for MEMS resonators in this context is highlighted thanks to an analytical model approach. Moreover, an experiment is reported in this section, so to highlight the feasibility of an AMB circulator with a novel implementation based on switches and capacitors.

Chapter 2 is a review of RF MEMS Microacoustic Resonators, which are used as main components in the circuits presented: piezoelectric effect is analyzed from an electro-mechanical perspective, the most used modes of vibration are introduced and characterized.
Some of the devices introduced in the chapter were laid out and fabricated in the Northeastern University facilities, so a full report on fabrication process of these components is presented. Through the use of these devices, multi frequency circulators are envisioned, and state-of-the-art devices were achieved for this application.

Chapter 3 proposes two circuits, designed with all the techniques analyzed in the previous chapters. Two different strategies to modulate the MEMS resonance frequency to obtain nonreciprocal transmission are proposed, and, for each of them, simulation performances are reported, as well as PCB testing results. For each topology, a parametric analysis shows trends predicted in Chap. 1. Practical limitations are also discussed when assessing performances such as intermodulation products and power handling.

Chapter 4 proposes another topology which aims at conjugate narrow band RF MEMS based filtering and nonreciprocal propagation. First a generalized dynamic S parameters formulation is presented, so to introduce *multi pole* modulation in AMB circuits. With this approach the main limits of the circuits implemented in Chapter 3 can be overcome thanks to the use of MEMS filters. Finally, experimental proof of the proposed circuit showing ultra low harmonic distortion is reported as a conclusion of the work.

Chapter 1

Angular Momentum Bias

1.1 Concept and First Demonstrations

The first use of Angular Momentum Bias (AMB) to implement a 3 port device with nonreciprocal transmission is documented in [16], and is applied in the acoustic domain. The idea at the core of this technology is to mimic the microscopic mechanism underlying the operation of magnetic circulators. A DC magnetic field, in fact, is able to split a given electronic state in two levels (Fig. 1.1) with counter rotating spin in certain materials. This induces different refractive index properties for waves propagating in opposite directions, and that is the physical foundation of nonreciprocal transmission.
This idea can be scaled into a macroscopic level in the structure descripted in Fig. 1.1 in the domain of acoustic waves propagating in air.
A ring cavity of radius R_{ave} connects three sources of acoustic pressure: by modulating its resonance frequency ω_0, the counter propagating waves in the cavity are going to be sustained by two different modes. This modulation is obtained by modifying the nominal sound velocity c_0 into $c_0 \pm \nu$ when an angular rate ν of fluid rotates within the cavity.
Under these conditions, the two modes will be respectively given by :

$$\omega^{\pm} = \omega_0 \pm \frac{\nu}{R_{av}} \tag{1.1}$$

For a given condition of rate ν one of the two waves is going to be subject to destructive interference at one port, constructive at the other.
Note that the interference is generated according to the flow *direction* of the external fluid *biasing* the cavity, so that nonreciprocal transmission can be achieved between the three ports.
In fact, following the analytical discussion reported in [16], it is found that the transfer function

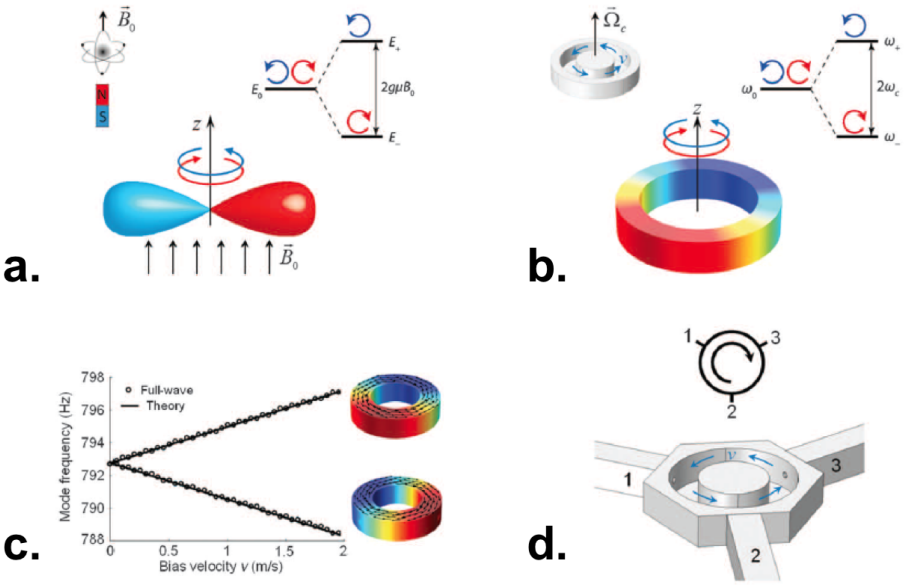

Fig. 1.1: *In **a** and **b** the physical analogy of a modulated ring and the atomic level splitting under $\vec{B}$ field is highlighted: as a magnetic field $\vec{B}$ is able to split energy levels in atomic states, so a rotational flow in a ring is able to split two counterrotating modes within the junction.*
*In **c** a simulation is highlighting the linear trend of the frequency splitting as in Eq. 1.1,while in **d** is a schematic representation of the acoustic circulator, where a rotational pressure flow with velocity $\vec{v}$ is up/down lifting the two modes. Copyright belongs to the authors of [16].*

from port 1 to port 2 ($T_{1\to2}$) and from port 2 to port 1 ($T_{2\to1}$) are respectively given by Eq. 1.2.
In Eq. 1.2, γ is the decay rate of the cavity, which following the more common resonators conventions in electrical engineering it would be reported in terms of Quality factor Q(in fact $\gamma = \omega_0/(2Q)$). In Fig. 1.2 a plot of the transfer functions is shown for a normalized $\omega_0 = 1rad/s$, $\gamma = 0.18$ and $\omega^{\pm} = \omega_0(1 \pm 0.1)$.

In these formulas the factor 2/3 takes into account the *static* transfer function: in fact all of these systems act as symmetric power splitters when not biased.
This system can be regarded as a sort of *directional* interferometer: the signal incoming from *port 1* will excite two modes propagating a different speeds. As one could derive from Eq. 1.2, the two modes supports different destructive interferometric conditions, so that after proper manipulation of Eq. 1.2, one can find that there is an optimal condition for ν to have $T_{1\to2} = 0$ and $T_{1\to3} = 1$, which is

$$\nu_{opt} = c_0/(2Q\sqrt{3}) \tag{1.3}$$

Even if the system is realized in another physical domain, it has been chosen to report it,

$$T_{1\to 2} = \left|\frac{2}{3}\left[\frac{e^{-i4\pi/3}}{1-i(\omega-\omega^-)/\gamma}+\frac{e^{-i2\pi/3}}{1-i(\omega-\omega^+)/\gamma}\right]\right|^2 \tag{1.2a}$$

$$T_{2\to 1} = \left|\frac{2}{3}\left[\frac{e^{-i2\pi/3}}{1-i(\omega-\omega^-)/\gamma}+\frac{e^{-i4\pi/3}}{1-i(\omega-\omega^+)/\gamma}\right]\right|^2 \tag{1.2b}$$

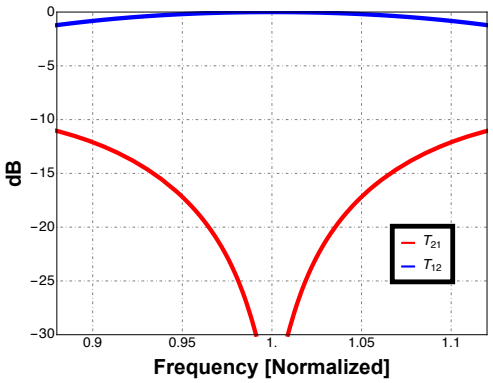

Fig. 1.2: *Transfer function described in Eq. 1.2.*

since it already shows all the typical features of the RF circulators implemented in this work.

Recent works [17, 18] have shown that similar performances can be achieved using the AMB concept when proper modulation of a nano-ring resonator is actuated with spaced electro-optical modulators in order to locally change the wave velocity.

However, when the aim is to replicate such functions in the RF waves domain, controlling the medium velocity is not as straightforward as in other domains. The first attempt to realize a similar device in electrical domain was relying on *varactors* in order to induce a modulation of the line impedance $Z_{0,i}(t) = \sqrt{L/2C_i(t)}$ in three different LC section coupled through capacitors (Fig. 1.3). Specifically, it is worthwhile to observe in Fig. 1.3 that:

- Three sources of modulation are required to achieve system symmetry.

The perfect symmetry guarantees that the transmission path follows the *direction* of modulation. This is really the reason why the reverse isolation ($T_{3\to 1}$) is exactly the same as the transmission from port 1 to the isolated port 2 ($T_{1\to 2}$).

- The optimal modulation rate ν_{opt} is inversely proportional to the cavity Q.

This last property shows one of the typical features of this system where the bandwidth of operation (thus its Q) is directly proportional to the modulation frequency ν. This feature will impose tight design constraints to RF implementations.

In this network three AC sources are required to properly bias the three stages of varactors as follows:

$$V^{(i)} = V_{dc} + V_m \cos\left(\omega_m t - \frac{i2\pi}{3}\right) \quad \text{for } i = 0, 1, 2. \tag{1.4}$$

where V_{dc} is needed to bias the device in a reverse region, so to fix the average value of capacitance C_{ave}; moreover each AC signal is applied with a $T_m/3$ time delay with respect to the adjacent port, so to effectively impart a Momentum Bias effect.

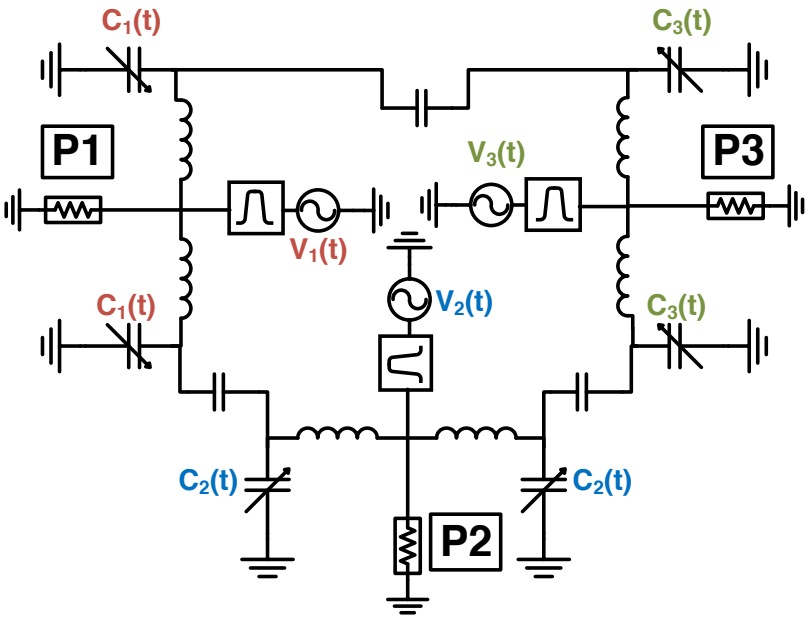

Fig. 1.3: *First proposed schematic of an RF circulator based on Angular Momentum Bias. Three RF ports P1,P2 and P3 are terminated to LC sections, which are coupled through capacitors. On each LC section an AC signal is superimposed to the RF path so to modulate the capacitance of a varactor, as in Eq. 1.4. This is a possible way of modulating the resonance frequency of a resonators loop, in a similar way of what was proposed in [16] in the acoustical domain.*

This early work shows already the advantages of using AMB circuits with respect to magnetic based circulators:

- Size. The active area of this device is contained in a diameter of 2cm, and operating around 200 MHz, it proves a deep sub-wavelength operation ($\lambda/75$).
- Tunability. By controlling the DC voltage applied on the varactors, C_{ave} changes, so the center frequency of the circulator can be tuned. When also the V_m is properly adjusted, a 25% tunability is measured.
- Control. The use of varactor requires low DC voltages ($1.5V < V_{dc} < 4.5V$) and very low control voltages($V_m \approx 0.6V$) thus proving to be a on-chip compatible technology.
- Giant Nonreciprocity. Even in this first work 40dB of IX were proven at the center frequency, proving better performances than commercially available magnetic based circulators [19].

On a side note, it is worth to mention that this whole circuit is composed of *reactive* elements, which are ideally non dissipative and thus potentially low-loss. In practice, because of the relatively low reported Q (10), as expected from Eq. 1.3, a modulation frequency $\nu_m = 15MHz$ (almost 10% of the RF signal) is needed, thus increasing the modulation branch complexity in order to avoid RF leakage. On top of that, as frequencies of operations scale up, figures of merit of inductors, such as Self Resonance Frequency (SRF) and Q per becomes more and more challenging. Commercially available inductors[20] for RF application where SRF has to be above 1GHz, maximal Q factor is typically around 40, so the use of inductors limit the practical Insertion Loss (IL) that can be introduced by these system, and most importantly, their power consumption, throught the fast pumping rate required by the circuit.

On the other hand, a number of very consolidated techniques are available to implement RF resonators, such as resonant cavities[7, chap.6][21, chap.5], lumped and distributed LC networks and most importantly for this work, MEMS based resonators[22, 23]. The choice of resonator structure and technology is crucial, when the aim is to find a feasible way to induce a *resonance frequency modulation* in a similar way to the one proposed in Eq. 1.1. For piezoelectric MEMS resonators, strategies to induce such a modulation will be covered in Chap. 3.

1.2 Angular Momentum Bias Circulator Model

The need for a more compact AMB network has been driven in the last years to achieve low IL to and fill the gap towards integrated technologies by minimizing the size and number of inductors required in the circuit.

More mature examples of AMB based circuit that move toward that direction are the ones reported in [24–27], and they are all based on either one of two main circuit topologies, that we will refer to as *Wye* and *Delta* topologies (Fig. 1.4).

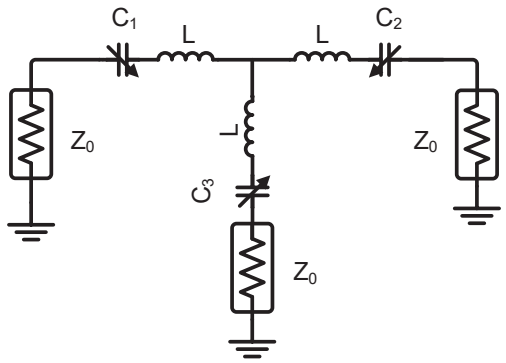

(a) *Wye implementation of an AMB circulator.*

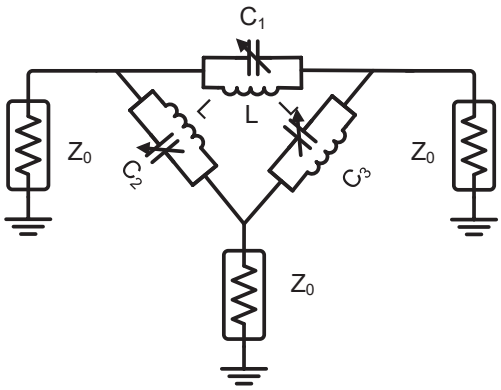

(b) *Delta implementation of an AMB circulator.*

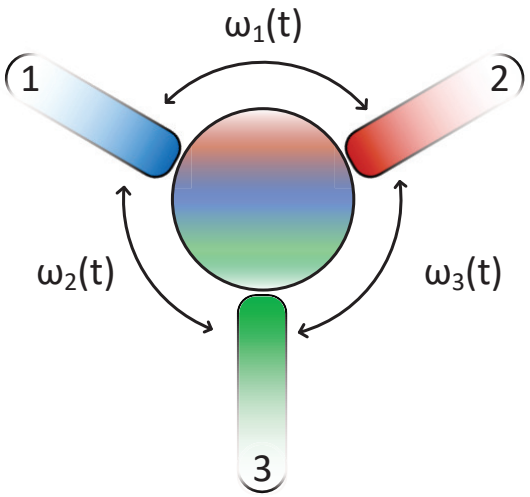

(c) *In an AMB circuit, time-variant resonant coupling described in Eq. 1.5 between three different RF ports induces strong nonreciprocity.*

Fig. 1.4

It is well known in fact that the two easier resonant impedances can be obtained by combining an inductor and a capacitor: a *series* resonator shows low impedance when excited close

to its natural frequency; a *parallel* resonator, which on the contrary tends to show high impedance at resonance.
Both of the circuits can be used, with a varactor diode, to implement a circulator. A *series* resonator can be used in a wye topology, a *parallel* resonator in a delta topology; both of them have been shown in recent works ([24] and [25] respectively).

It can be seen that thanks to the varactor $C(V)$ dependence, for both the circuits in Fig. 1.4, the resonance frequency of each branch is modulated in time, and the pattern of modulation follows the spacial distribution (Fig. 1.4) of the three ports.
For this reason it is possible to classify the circuit as a *spatiotemporal* modulator, among others recently investigated[12, 13].
The modulated resonant modes are excited as follows, when a sinusoidal excitation (Eq. 1.9) is applied:

$$\omega(t) = \omega_0 + \Delta\omega \cos\left(\omega_m t - i\frac{2\pi}{3}\right) \quad \text{for } i = 0, 1, 2. \tag{1.5}$$

Where $\omega_0 = 1/\sqrt{LC_{ave}}$ both in Fig. 1.4a and in Fig. 1.4b, and C_{ave} is the static part of the capacitance, like in Eq. 1.9.
In order to have a grasp of the system response, an analytical approach has been investigated in this work. The analysis was conducted on the wye configuration, but the delta configuration could have been treated in an analogous way.

For the electrical circuit shown in Fig. 1.4a a possible starting point in the analysis is a KCL set of equations written as functions of the *charge* on each of the three branches. In this way the problem of treating integro-differential equations with time-varying coefficient is simplified into a simpler differential equations set.

Once recognized the two state variables as the charge q_1, q_2 it is possible to study the dynamic evolution of the autonomous system with the following system of 2 equations of 2^{nd} order differential equations:

$$\frac{C_{ave}}{C_1(t)}q_a(t) + \frac{C_{ave}}{C_2(t)}q_b(t) + \frac{q_a'(t) + q_b'(t)}{\omega_0 Q_L} + \frac{q_a''(t) + q_b''(t)}{\omega_0^2} = 0 \tag{1.6a}$$

$$\frac{C_{ave}}{C_1(t) + C_3(t)}q_a(t) - \frac{C_{ave}}{C_2(t)}q_b(t) + \frac{2q_a'(t) - q_b'(t)}{\omega_0 Q_L} + \frac{2q_a''(t) - q_b''(t)}{\omega_0^2} = 0 \tag{1.6b}$$

In these equations and in the following, $\omega_0 = 1/\sqrt{LC_{ave}}$ and Q_L is the loaded quality factor of each branch.

Specifically, these kind of networks have two sources of damping: one is due to the ohmic losses of the inductor (R_{ind}), the other is due to the 50 Ω termination (Z_0).

To each of them a quality factor can be associated, nominally

$$Q_{ind} = \frac{\omega_0 L}{R_{ind}} \quad Q_0 = \frac{\omega_0 L}{Z_0}$$

Through standard circuit analysis it can be shown that the overall damping factor (that is the impedance seen from the central node to each ground) can be expressed as:

$$Q_L = \left(\frac{1}{Q_{ind}} + \frac{1}{Q_0} \right)^{-1} = \frac{Q_{ind} Q_0}{Q_{ind} + Q_0} \tag{1.7}$$

From the previous equation, since Z_0 is assumed to be 50 Ω, it is always desirable to have $Q_{ind} \gg Q_0$. When this condition is not met, Insertion Loss (IL) degradation will be given by the resistive voltage drop across the inductor.

Extensive work was done in order to find a time domain solution to this autonomous system, but no easy general solution exists for differential problems where the state matrix A(t) is time varying.

Some interesting approaches based on Floquet Theory are reported in classic control theory books like [28, chap.2-3], but no analytical solution was found for this system.

On the other hand, once the system is recast in the so called *state* space, it is possible to make some comments on the stability, as reported for example in some circuit theory papers such as [28, chap.5][29], regarding very similar topologies excited in another region of ω_m where the varactor acts as a *parametric amplifier*. The main result of the stability analysis is that as long as ω_m is much smaller than the condition

$$\omega_m = 2\omega_0 \tag{1.8}$$

The system does not show parametric instability, even in the lossless case where $Q_L \to \infty$. For AMB the typical operation is found when $\omega_m \ll 0.2\omega_0$, far away from unstable conditions. Moreover, the damping provided by the 50 Ω termination is enough to suppress any other unstable region.

When trying to find a closed form solution for the circuit in Fig. 1.4a, the C(V) modulation makes the problem too difficult to be treated analytically. A realistic approximation of the problem can be treated analytically, instead, if the modulation C(V) curve of the varactor is linearized around a bias point V_{dc}.
Under these assumptions, when the control voltage on the varactors is the sum of a DC

term and a sinusoidal term at ω_m as in Eq. 1.4 the capacitances can be expressed as:

$$C_i(t) = C_{ave}(1 + \delta \cos(\omega_m t - i\frac{2\pi}{3})) \quad \text{for } i = 0, 1, 2 \tag{1.9}$$

Where C_{ave} is the bias point capacitance, and $\delta = \Delta C / C_{ave}$ is the first order expansion of the capacitance sensitivity with respect with the modulation voltage.
It is straightforward in this way to see that the resonance frequency of each branch follow the trend of Eq. 1.5. Under this assumptions, by expanding the terms $1/(1+\delta) \approx 1 - \delta$ and by considering an excitation V_{in} at one port, it is possible to rewrite one can consider the Eq. 1.6 in a more useful way:

$$\begin{cases} q_a(t)(1 - \delta \cos(\omega_m t)) + q_b(t)(1 - \delta \sin(\omega_m t - \frac{\pi}{6}))+ \\ \frac{q_a'(t) + q_b'(t)}{\omega_0 Q_L} + \frac{q_a''(t) + q_b''(t)}{\omega_0^2} = C_{ave} V_{in}(t) \\ 2q_a(t)(1 - \frac{\delta}{2} \sin(\omega_m t - \frac{\pi}{6})) - q_b(t)(1 + \delta \sin(\omega_m t - \frac{\pi}{6}))+ \\ \frac{2q_a'(t) - q_b'(t)}{\omega_0 Q_L} + \frac{2q_a''(t) - q_b''(t)}{\omega_0^2} = C_{ave} V_{in}(t) \end{cases}$$

When the system is written in such a way, it is possible to find a closed form solution in its frequency domain representation (through a suitable Fourier Transform) since in this case elementary harmonic functions are multiplied in the time domain and they can be transformed into frequency domain convolutions.

In fact, since a *sinusoidal* steady state solution is assumed, the derivation, although very lengthy, becomes just a matter of algebraic manipulation.

For example, a reasonable solution might be found assuming that charge q_1, q_2 can be found at the fundamental tone ω and at the two closest Inter Modulation(IM) products $\omega \pm \omega_m$ and $\omega \pm 2\omega_m$. Using phasor notation, a solution will be imposed as a sum of 5 complex variables $q_i(\omega)$, that is

$$q(\omega) = \sum_{i=-2}^{2} q_i(\omega - i\omega_m) \tag{1.10}$$

Each of the two charges distribution in the system are expressed using Eq. 1.10.

The analytical proposed solution is graphically shown in Fig. 1.5, and can be derived when it is assumed that:

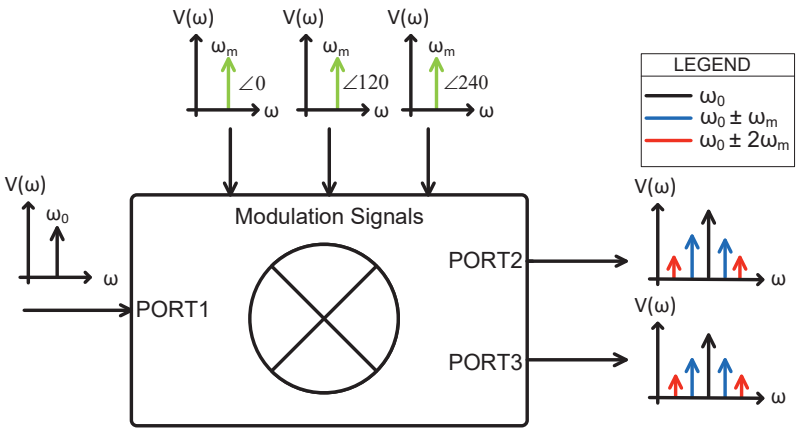

Fig. 1.5: *A frequency representation of the modeled input-output spectrum using an Harmonic Balance approach.*

- $i_i(\omega) = j\omega q_i(\omega)$
- $S_{11}(\omega) = 1 - 2\dfrac{Z_0 i_1(\omega)}{V_{in}(\omega)}$
- $S_{21} = \dfrac{2Z_0 i_2(\omega)}{V_{in}(\omega)}$
- $S_{31} = \dfrac{2Z_0 i_3(\omega)}{V_{in}(\omega)}$

It is worth noting at this point that thanks to the threefold symmetry of the circuit, the transfer function S_{31} it will be equal to S_{12} and so on. So a complete S-parameters representation of the AMB circulator can be found as a combination of just three transfer functions:

$$\begin{bmatrix} S_{11} & S_{21} & S_{31} \\ S_{31} & S_{11} & S_{21} \\ S_{21} & S_{31} & S_{11} \end{bmatrix} \tag{1.11}$$

The equations are found by verifying Eq. 1.10 for each n^{th} component of the charge at each harmonic.

The analytically found S-parameters can be written as a set of 8^{th} order polynomial rational functions and they were practically found on a symbolic calculator. The analytical solutions are rather lenghty, so it was chosen not to report the full transfer functions. Instead, a

contour plot can better describe the model, and it is shown in Fig. 1.7.

However, a *generalized impedance model* was found later in this work: it is described in Chap. 4, a compact analytical formula is provided, which of course also covers this circuit. Some important observations can be done by analyzing the model, nominally:

- The direction of propagation is *opposite* with respect of the direction of modulation. That is, if the delay is following a pattern $1 \rightarrow 2, 2 \rightarrow 3$, then the signal will be transmitted with a pattern $1 \rightarrow 3, 3 \rightarrow 2$.
- *Higher Q requires lower* δ. Clearly a lower δ will result in an improved linearity response, and, being the whole model based on a first order $C(V)$ expansion, this will also results in a better modeling of the circulator.
- The model valid as long as $\omega_m \ll \omega_{rf}$: when modeling the varactor as in Eq. 1.9, higher order IM products are neglected (nominally the *images* of the $V_m \times V_{rf}$), because it is possible to show that their ratio is proportional to ω_{rf}/ω_m. As ω_m approaches ω_{rf}, the model loses validity.
- For each choice of components, there is an optimal combination of ω_m and δ which optimizes the isolation. The optimal curve ω_m, δ is linear (Fig. 1.7).
- The bandwidth of the IL is proportional to the bandwidth of the IX, and both of them are proportional to the bandwidth of the LC resonator (thus inversely to its Q_L).
- As Q_L is increased, the dynamic response becomes slower, so that the modulation frequency ω_m can be decreased.

To test the limits of this model, a numerical analysis was run: a comparison of simulations and analytical model is reported in Fig. 1.6 for two different working points. While the model matches the simulations with good accuracy for small δ ($\simeq 10\%$), an error arises as δ increases.
Note that the main effect of this nonlinearity is in the shift of the center frequency of operation, while nonreciprocal transfer function shape is retained.

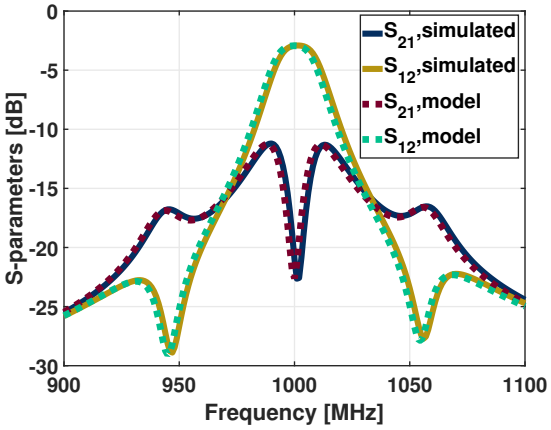

(a) *Model matching of circuit simulation for setup 1. (Transmission)*

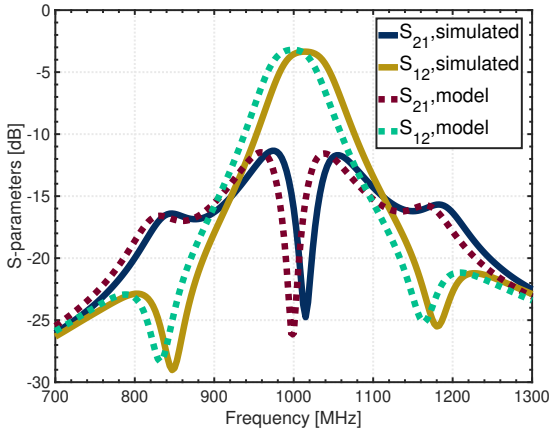

(b) *Model matching of circuit simulation for setup 2. (Transmission)*

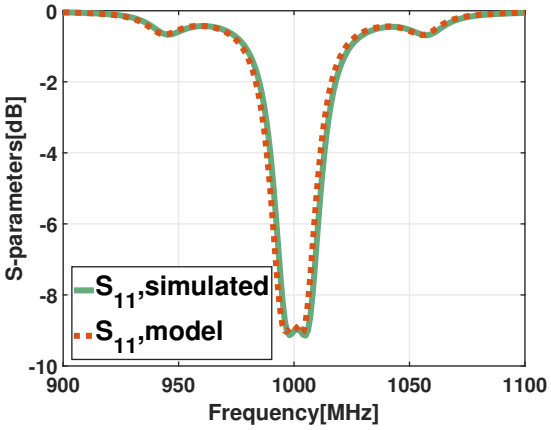

(c) *Model matching of circuit simulation for setup 1. (Reflection)*

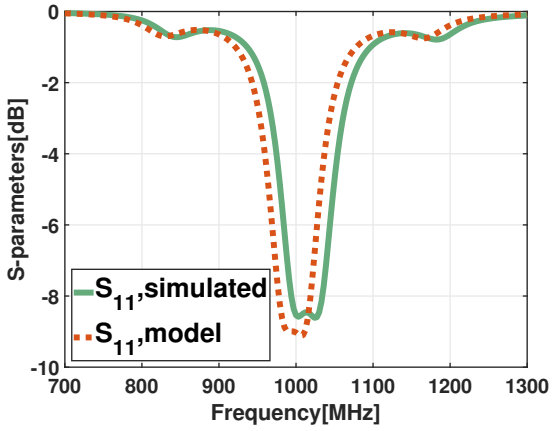

(d) *Model matching of circuit simulation for setup 2. (Reflection)*

Fig. 1.6: *Circuit model analysis for two setups:*
1. $\delta = 8\%, F_m = 50MHz, L = 500nH$ *(Fig. 1.6a,Fig. 1.6b)*
2. $\delta = 25\%, F_m = 150MHz, L = 150nH$ *(Fig. 1.6c,Fig. 1.6d)*

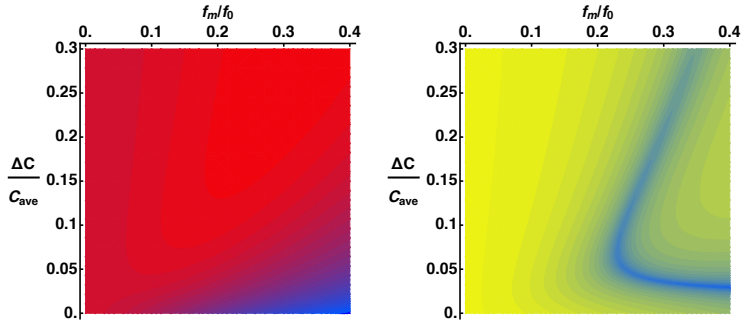

(a) *$Q_{loaded} = 12$ system model*

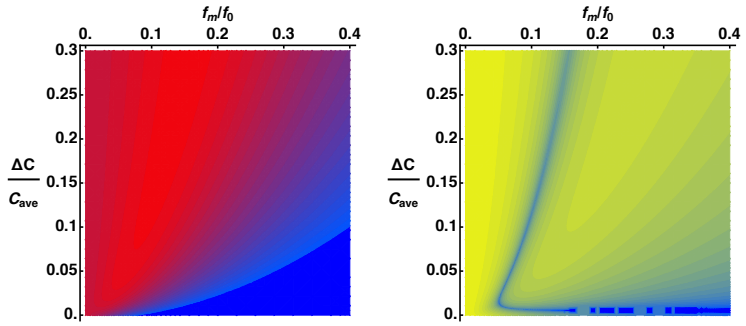

(b) *$Q_{loaded} = 60$ system model*

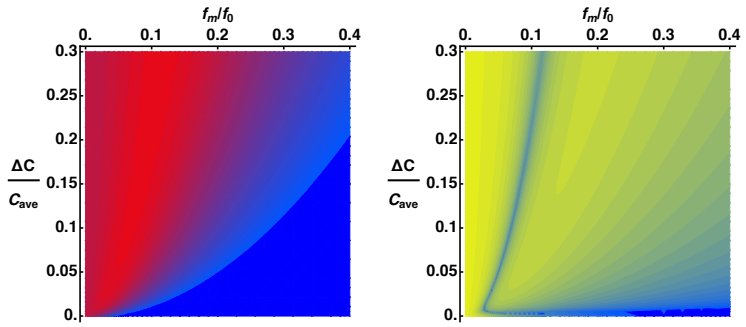

(c) *$Q_{loaded} = 120$ system model*

Fig. 1.7: *Analytical contours of Insertion Loss IL (on the right) and Isolation IX (on the left) for different conditions of Q. The red regions on the left in correspond to the minima of IL,while the blue regions on the right the maxima of IX. From these plots it is clear that there is an optimum point for each Q, and a quasi-linear region of suboptimal operation. The optimal ω_m/ω_0 scales down as Q increases.*

1.3 Breaking the limits of AMB circuits

Following to the first works results ([24, 25]), it is clear that one main issue with this class of networks is the relatively high IM product, close to the RF spectrum (note that, as discussed in the previous section, the first IM tones are found at $\omega \pm \omega_m$. A typical simulation result is commented in Fig. 1.8.
To make this circuits more appealing in the crowded RF environment, strategies were recently developed to counterbalance the delivery of power at IM tones.

The first strategy, reported in [27], in line with other similar solutions ([30, 31]) adopted in similar LPTV networks, is to actuate the AMB with two *complementary* networks, each of them operating with opposite phases, as shown in Fig. 1.9.

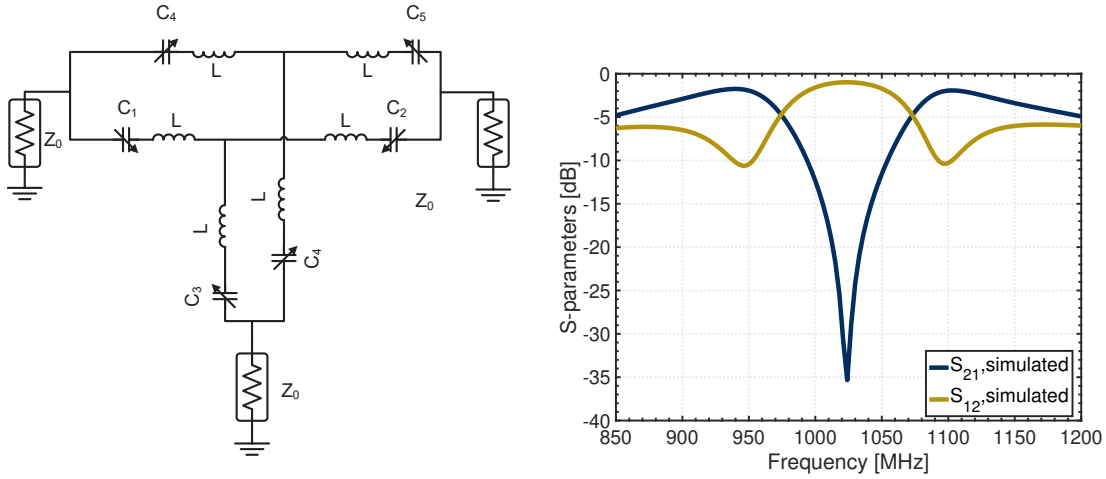

(a) *Schematic of differential AMB circuit.* ***(b)*** *Simulation results.*

Fig. 1.8: *Example of AMB differential Wye circuit with the following setup: Fm=150MHz, L=40nH,* $\delta = 30\%$

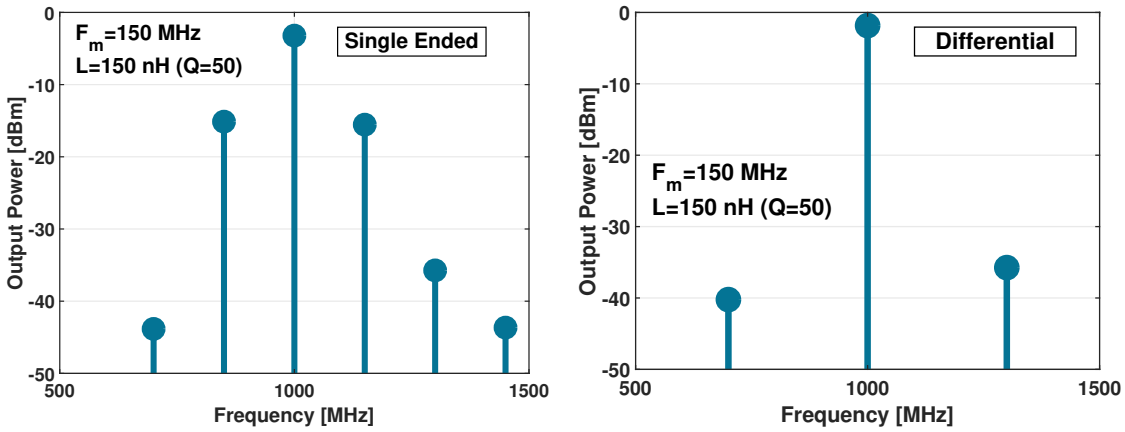

(a) *Simulated output spectrum of a Single ended AMB (Fig. 1.4)*

(b) *Simulated output spectrum of a Differential AMB (Fig. 1.8)*

Fig. 1.9: *Comparison of output spectrum for two different Wye Circuit.*

This kind of networks [27], referred to as *differential* to emphasize the similarities with conventional circuit with a point of simmetry[32, chap.12], are able to suppress *all* of the IM products, thus approaching a LTI behaviour from an input/output point of view.
This is achieved by driving the two dynamic components connected to each branch with out of phase signals. The AMB functionality is preserved since for each branch the driving signal pattern still follows Eq. 1.4.

However, it is worth noting that these differential networks are mainly conceived to suppress output tones produced by the modulation, not to suppress power-generated distortion (many other techniques are currently adopted to suppress distortions generated by the varactor, like the back-to-back operation descripted in [33]). To prove this point, two output spectra are compared in Fig. 1.9: a significant $\simeq$30dBc improvement of the IM suppression in the case of the differential circuit is simulated.

In the same work ([27]) a P1dB of 29dBm is reported, and more than 25dBc of first IM rejection was demonstrated ([34]) using this topology thus significantly improving the first experiments done on the AMB circuits, like the ones reported in the previous section.
In this last work, a detailed noise analysis is provided, which highlights that since this circuit reduces IM products, it will also reduce the impact of noise figure (NF) coming from them: for this reason, in an ideal scenario, the NF would be exactly equal to the IL. A NF=2.5dB is reported, for a IL<2dB.
It is necessary at this point to assess the fundamental limits of these topologies, once applied to higher and higher RF frequencies, up to the millimeter waves range:

- Inductor performances are critical. There are at least three critical aspects when using discrete (or distributed) inductors in this class of circuits:

- ▶ Q_{ind} should not limit the system damping, as discussed above, as this would degrade both static IL and dynamic response.
- ▶ The only way to push the modulation frequency ω_m as a smaller and smaller fraction of ω is to increase the system Q_L, thus using larger inductances.
- ▶ When implementing differential circuits, asymmetry is always an issue, thus any unavoidable mismatch between the components would degrade IM suppression and dynamic response of the stage.

After these considerations, if one could induce time modulation of high Q resonators center frequency, then this would solve all the limits given by the use of inductors.

- The use of varactor diodes has two main downsides:
  - ▶ They tend to show low power handling, introducing distortion and limiting the overall functionality of the system.
  - ▶ They require additional filters to be properly driven.
    This practical implementation aspect is detrimental for area considerations: more inductors (or more generally diplexer structures) are needed in order to prevent RF leakage in the modulation loop and to effectively superimpose a modulation signal V_m .

So using another component to induce a modulation would be clearly beneficial, or at least a viable option.

This work, in fact, as briefly explained in the introduction, has been focused in the modeling, the simulation and the experimental validation of a new class of AMB based circuits where

- Inductors are replaced by **Piezoelectric MEMS Resonators**, which, for reasons that will be clarified in the Sec. 2.1, can count on very repeatable and high Q resonant modes.
- Varactors are replaced by **Switched Capacitor Networks**, so to overcome linearity issues and simplify the modulation network. Arguments will be provided in Sec. 1.4.

1.4 Switched Capacitor LC implementation

As discussed in Sec. 1.3, it would be desirable to remove varactors from the circuit in Fig. 1.8. In order to do that, in this work it has been proposed to achieve this through CMOS switches in reflective-open configuration. As follows from Fig. 1.10 it is clear that the switching scheme induces very similar modulation patterns.

From a modeling point of view, this design technique imposes to take into account a large

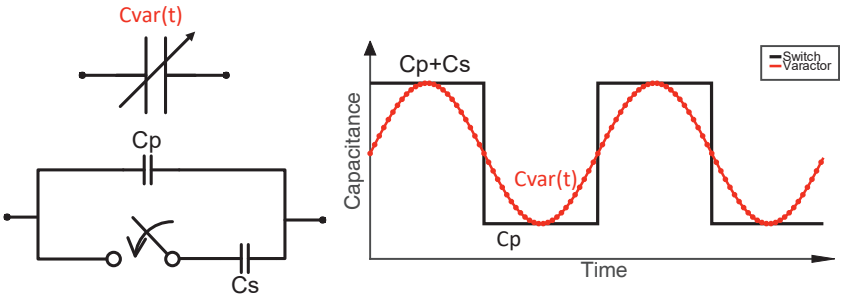

Fig. 1.10: *Comparison of two mechanism to induce capacitance variation in a periodic way. The solution based on switches contains a broader spectrum of modulation tones, but similar performance are expected in terms of S-parameters: for example compare the simulated results in Fig. 1.8 for an varactor based circulator, and the experimental results in Fig. 1.12 for a switch based circulator.*

number of intermodulation tones, so analytical modeling becomes unpractical. Simulation becomes more and more accurate as the number of tones increases, so the model based on sinusoidal modulation is not theorically sound anymore.

To prove that similar behaviour can be achieved in systems where the capacitive modulation is induced with a switched capacitor system, a PCB was designed and tested in the early stages of these works.

The measured performance of this circuit are reported in Fig. 1.12 where an optimal modulation frequency of 1.6MHz (10% of the carrier) guarantees more than 30dB of peak isolation and an IL of 3dB. The measured P1dB (12dBm) in Fig. 1.12b is very close to the rated P1dB of the switch (15dBm), thus suggesting that the linearity can be improved if the switch linearity is improved. A parametric plot of IL and IX is shown in Fig. 1.12c, so it can be seen that the optimal IX is achieved for a minimum IL.

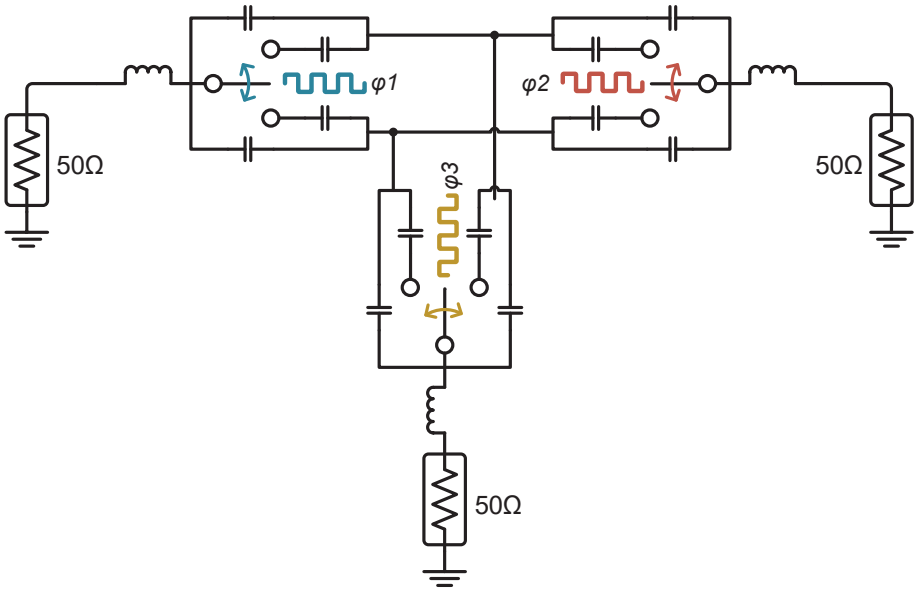

(a) *Schematic of the PCB.*

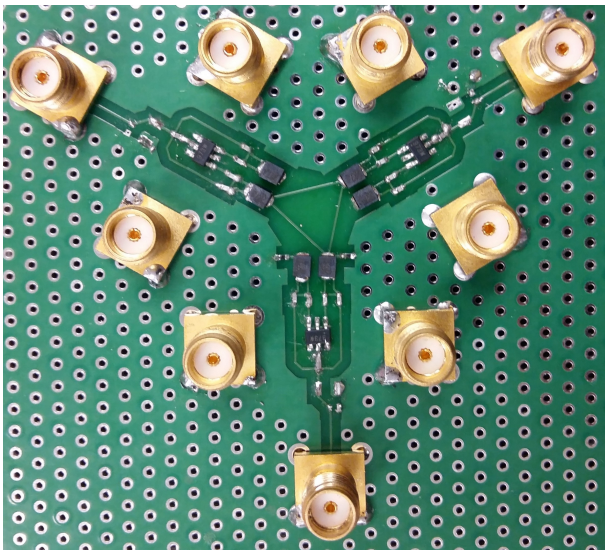

(b) *Picture of the PCB.*

Fig. 1.11: *Proposed implementation of a differential LC switched capacitor AMB circuit. The three SPDT switches in Fig. 1.11a are commutated with a 50% Duty Cycle, and a phase shift of $120°(T_m/3)$ between each other, so to operate in an Angular Momentum Bias fashion.*
A custom PCB was designed and implemented in Fig. 1.11b.

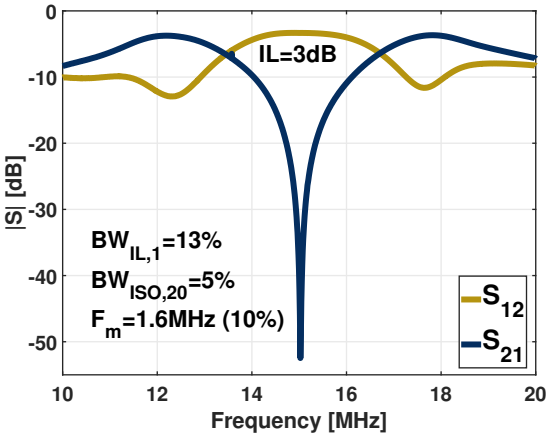

(a) *Measured Sparameters for circuit in Fig. 1.11, with Fm=1.6MHz.*

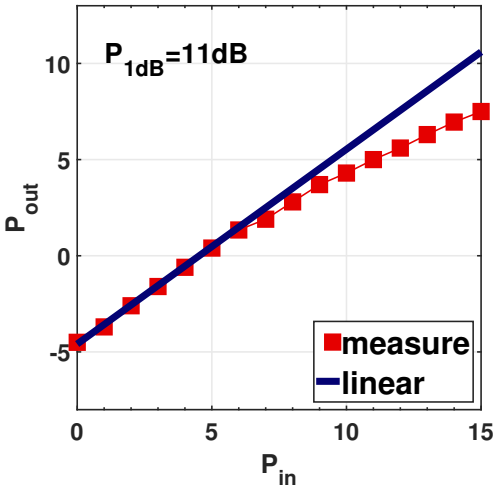

(b) *Input P1dB≈12dBm.*

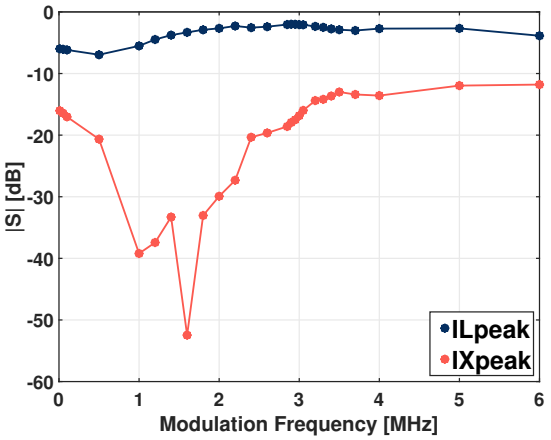

(c) *Parametric analysis of IL and IX peaks for various Fm.*

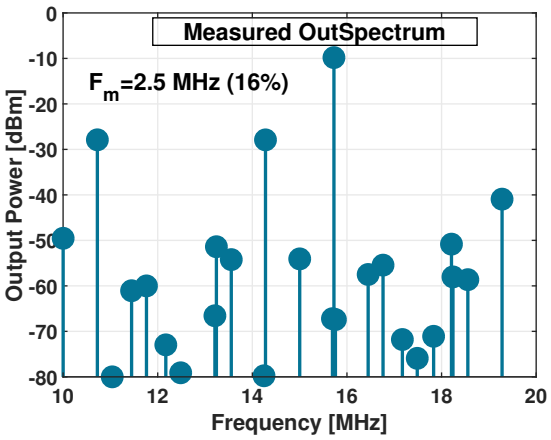

(d) *Output spectrum.*

Fig. 1.12: *Experimental results from the PCB in Fig. 1.11b with L= 2.7μH, Cs=47pF, Cp=27pF.*

Chapter 2

Piezoelectric MEMS RF resonators

2.1 Basics on Piezoelectricity

After analyzing in Chap. 1 the properties of circuits based on Angular Momentum Bias, the need of high quality factor (Q) in these circuit was highlighted. Having access to such components can lead to many advantages in this application, namely the possibility to minimize the power required by the circuit, thanks to the lower modulation frequency required when high Q resonators are employed (Fig. 1.7) and the possibility to miniaturize the system.
Piezoelectric MEMS resonators can serve this purpose, as their RF resonances typically exhibit a Q higher than passive discrete components, and their resonance frequencies are set by geometrical dimensions, so (in some cases that will be discussed later) different resonance frequencies can be obtained on the same chip. Moreover, circuit miniaturization can be achieved in a CMOS compatible process.
All of these aspects will be discussed in this chapter.

Materials showing piezoelectric properties have been engineered and adopted in a very large number of applications, as references in timing applications ([22, 35]), as sensors in a very broad range of domains and frequencies ([36, 37]) and as well as actuators in system control ([38]) and transducers for communication and energy harvesting ([39–41]).
The reason of the popularity of these materials is their unique feature of converting electrical energy in elastic energy and vice-versa. A simple explanation is graphically shown in Fig. 2.1: piezoelectric materials respond to electrical voltage generating stress.

For the purpose of analyzing resonators based on piezoelectric materials, a matrix approach will be necessary, since the electrical features of the resonator will depend on the *coefficient* of the piezoelectric tensor.

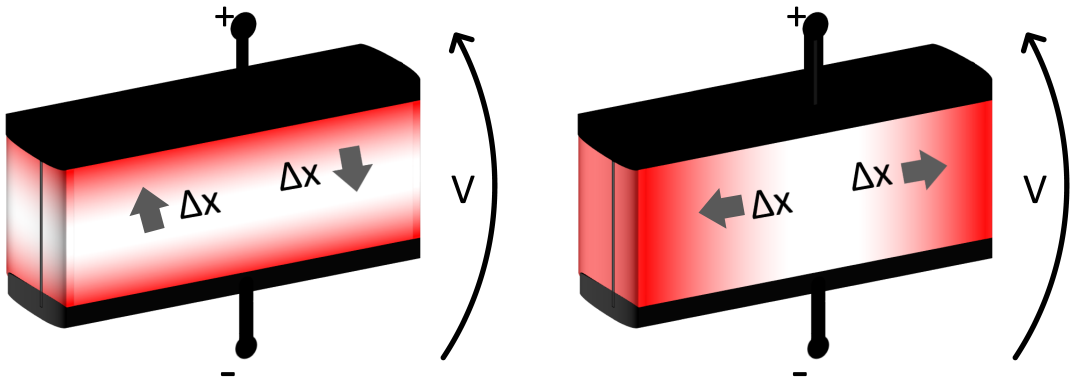

(a) *Example of a piezoelectric thickness excitation.*

(b) *Example of a piezoelectric lateral excitation.*

Fig. 2.1: *Basic idea of piezoelectric effect.*

A complete picture of a low frequency (that is for frequencies much lower than the resonance) piezoelectric modeling from an electro-mechanical point of view is reported in many texts ([42–44]), so just the main results are here reported.
Considering the already mentioned property of exhibiting mechanical stress $\vec{T}$ in response to an applied electric field $\vec{E}$ and vice-versa, one could write a set of equations where the two vectors $\vec{T}$ and $\vec{E}$ are respectively sources of electrical displacement $\vec{D}$ and strain $\vec{S}$:

$$\begin{cases} \vec{D} = d_1\vec{T} + \epsilon_r\vec{E} \\ \vec{S} = k_H\vec{T} + d_2\vec{E} \end{cases} \tag{2.1}$$

Where ϵ_r and k_H are respectively the material dielectric coefficient and the Hooke constant and the two tensors responsible for the coupling between physical domains d_1 and d_2 are referred to as *piezoelectric charge coefficients*, and measured in $[pC/N]$. One could easily verify that ,as $d_1, d_2 \to 0$ the equations become decoupled and the equations resembles classic electrical and mechanical tensor equations.

Interestingly, for most materials $d_1 = d_2 = d$ (thus the conversion mechanism has the same efficiency in both directions), so the equations can be simplified into the following:

$$\vec{S} = k_H(1 - k_t^2)\vec{T} + \frac{d}{\epsilon_r}\vec{D} \tag{2.2}$$

Where k_t^2, commonly referred to as *electromechanical coupling coefficient*, is defined as:

$$k_t^2 = \frac{d^2}{k_H\epsilon_r} \tag{2.3}$$

As seen in Eq. 2.2, k_t^2 is adimensional, at can be regarded as a normalized conversion efficiency term between the stress induced by elastic forces and electrical forces.

Similar energetic arguments explained in [43, Part II, Chap.5] would lead, in fact, to an alternative equivalent definition as:

$$k_t^2 = \frac{W_m}{W_m + W_e}$$

Which is exactly an efficiency conversion between the mechanic energy stored in the material W_m and the total energy $W_m + W_e$.

A complete equivalent two-port model in the Laplace variable s can be derived for a simpler one-dimensional problem, applying basic electrodynamic arguments derived in [42] the electrical domain variables $I(s)$ and $V(s)$ with the mechanical domain ones, the strain $S(s)$ and the stress $T(s)$:

$$\begin{bmatrix} I(s) \\ S(s) \end{bmatrix} = \begin{bmatrix} C_0 & sAd \\ \frac{d}{t} & k_H \end{bmatrix} \cdot \begin{bmatrix} V(s) \\ T(s) \end{bmatrix} \tag{2.4}$$

Where A is the area where the electric field is applied, t is the material thickness and

$$C_0 = \epsilon_r \frac{A}{t} \tag{2.5}$$

is the *static capacitance* in the direction of the applied field.

So from the analysis of this model it has been shown that when an electric field $V(s)$ is applied on a piezoelectric material, both a *capacitive* current is generated as

$$I(s) = sC_0V(s)$$

and a *mechanical* strain is generated as

$$S(s) = \frac{d}{t}V(s) \tag{2.6}$$

2.2 Piezoelectric MEMS resonators

As follows from the previous section, a mechanical strain is generated in a piezoelectric material when an electric field is applied.

A small digression has to be conducted on the *direction* of this strain: in fact the model in Eq. 2.4, even if formally displayed for a mono-dimensional case, can be easily extended in a three-dimensional case, as $\vec{d}$ is a 9x9 tensor, if all the longitudinal and torsional excitation are considered.
However, typically most materials show a certain simmetry, and a relevant piezoelectric effect only in given directions, so that the matrix can be reduced to a lower order.

The mechanism underlying the piezoelectric resonance is very similar to the one which regulates the mechanic resonance of every spring-mass-damper system[43, Part.2, chap.7]: if $u(t)$ is the displacement, ρ is the material density and E_p is the Young modulus, when a boundary condition can found for the wave equation (here simplified to a monodimensional case)

$$\rho \frac{d^2u}{dt} = E_p \frac{d^2u}{dx} \tag{2.7}$$

Then the mechanical solution will be a standing wave, the two forms of energy will tend to exchange power at the same rate so that the losses are minimized. As the reader could observe from equation Eq. 2.7, the specific solution (which is the resonance frequency and a spatial mode field), depends at least from:

- the piezoelectric coefficient d_{ij} (or the piezoelectric coefficients) actuating the mode.
- the geometry of the device.
- the material stiffness and density.

There is at the present moment a whole scientific community working on resonant modes in Piezoelectric devices, and many interesting works can be found for example in [45–48].

In any case of mode excitation, an electrical equivalent of these phenomena can be promptly derived both in the case of two-port excitation ([49]) that in the case of one-port excitation ([15]), and are reported in Fig. 2.2.
However, using two-port actuated resonators in RF front ends in very challenging and was not at object of this work, so just one port structure will be analyzed from now on.
The electrical models shown in Fig. 2.2 can be derived from a voltage/current link with the force/displacement mechanical quantities in Eq. 2.7 and Eq. 2.2.
The resulting equivalent electrical model, derived for example for one-port excitation in [43,

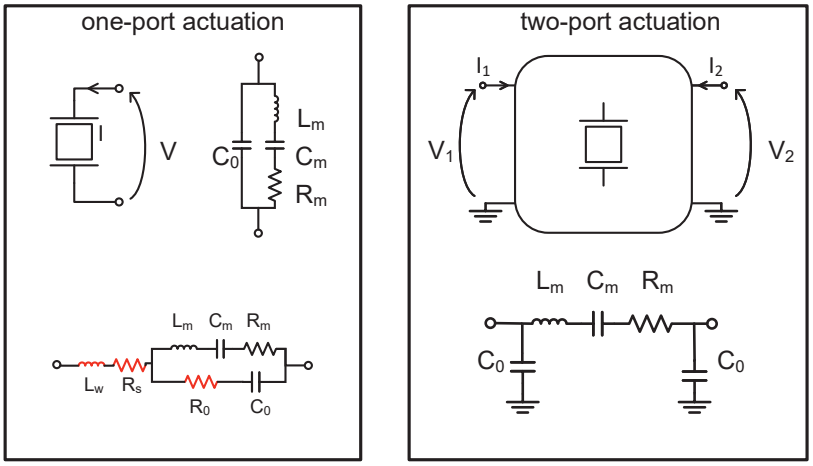

Fig. 2.2: *Electrical equivalent circuit of 1-port resonator (left) and 2-port resonator (right).*

Part 2, Chap.7], is here reported:

$$L_m = \frac{8}{\pi^2 \omega_0^2 k_t^2 C_0}$$
$$C_m = \frac{\pi^2}{8} \frac{k_t^2}{C_0}$$
$$R_m = \frac{8}{\pi^2} \frac{1}{\omega_0 C_0 k_t^2 Q}$$

Where L_m is the *motional inductance*, expression of the mass loading of the system, $C_m$is the *motional capacitance*, expression of the compliance of the system and R_m is the *motional resistance*, expression of the dissipative forces in the system.
C_0 is the static capacitance, corresponding to the actuation area as described in Sec. 2.1. Interesting, as one could observe comparing Eq. 2.8 with Eq. 2.2, C_m represents the motional, or better, vibrational actuation induced by the piezoelectric efficiency k_t^2, in fact it is indepedent on the resonance frequency and proportional to the conversion efficiency k_t^2.

Moreover, it could be noted that R_m is just another expression for the device quality factor Q, which is originated from *mechanical* and *electric* losses, but it is most commonly dominated by acoustic losses in the substrate [50].

A typical admittance curve is plotted in Fig. 2.3b, and, by manipulating the transfer function $Y_{res}(\omega)$, one can found the following results, under the assumptions of an underdamped

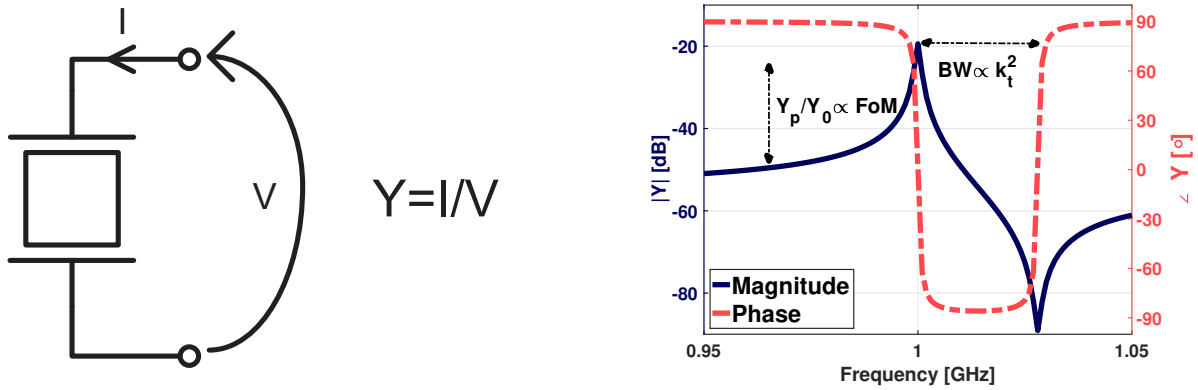

(a) ***(b)***

Fig. 2.3: *typical expected admittance response for MEMS piezoelectric resonators. Note that, once the resonance frequency is set, one devices can be characterized through its k_t^2 and its Figure of Merit(FoM).*

system (so assuming $Q \gg 1$):

$$Y(\omega_s^2) = \frac{1}{L_m C_m} \tag{2.9a}$$

$$\omega_p^2 = \frac{1}{L_m C_m \parallel C_0} \tag{2.9b}$$

$$Y\big|_{(\omega_s)} = Y\big|_{LF}\sqrt{1 + (\frac{8}{\pi^2}k_t^2 Q)^2} \tag{2.9c}$$

$$\frac{\omega_p}{\omega_s} = \sqrt{1 + \frac{8}{\pi^2}k_t^2} \tag{2.9d}$$

As follows from Eq. 2.9, the resonance peak magnitude in Fig. 2.3b is proportional to the product $k_t^2 Q$ which is called Figure Of Merit (FOM) of the resonator (Fig. 2.3b): for instance, in recent works ([45]) , resonators with a FOM greater than 100 have been demonstrated. For this class of high Q resonators:

$$\big|Y\big|_{peak} \propto \big|Y\big|_{LF} \cdot FoM \tag{2.10}$$

What is instead referred to as *bandwidth* of the resonator is the relative distance $\frac{\omega_p - \omega_s}{\omega_s}$, and it can be shown that is entirely dependent on the resonator k_t^2, which can be lead to another *working* definition for k_t^2:

$$k_t^2 = \frac{4}{\pi^2}\frac{\omega_p - \omega_s}{\omega_s} \tag{2.11}$$

This is an operational definition of k_t^2, since admittance peaks can be measured with very good accuracy using Virtual Network Analyzers. A more accurate resonator model, which includes metals resistance R_0, probe losses R_s and wirebonding finite-Q inductances (L_w are shown in Fig. 2.2, but from a functional point of view, there are four main parameters needed to describe the electrical response of a MEMS piezoelectric resonator: Q, k_t^2, C_0, ω_s.

To grasp of the physical numbers required to implement RF resonators, a target series resonance frequency of 1GHz was chosen, and the popular aluminum nitride AlN is chosen as a piezoelectric material. Several devices were laid out, fabricated and tested during this work, using AlN: even if this material is not among the ones with the highest piezoelectric charge coefficients, its deposition is compatible with CMOS process ([51]) thus making it appealing for the integration with CMOS circuitry.

Typical material performances can be compared with another popular piezoelectric material such as lithium niobate ($LNb0_3$) which is instead non CMOS compatible. A comparison can be assessed in Tab. 2.1.

Piezoelectric Coefficient [pmV^{-1}]	A_lN([52])	PZT([53])	LN_bO_3([54])
d_{33}	$5.7[\pm 15\%]$	$-374[\pm 30\%]$	-21
d_{31}	$2.5[\pm 15\%]$	$171[\pm 30\%]$	74
d_{15}	N.A	N.A	69.2
d_{22}	N.A	N.A	20.8

Tab. 2.1: *Comparison of piezoelectric coefficient for common materials used in MEMS technologies. Note that these numbers vary depending on crystal orientation, substrate conditions and testing apparatus, thus they are meant to be a first order estimate of these parameters.*

Two popular excitation modes are here reported as a case study: the Contour Mode Resonator (CMR) and the Bulk Acoustic Wave (BAW) resonators, also known with the commercial name of Film Bulk Acoustic Resonator (FBAR).

2.2.1 BAW

BAW devices are at the present moment the most reliable [47] resonant technology for communication applications based on piezoelectric devices. This class of devices are based on the so called *thickness* mode of vibration, as can be seen from Fig. 2.1a. In fact, acoustic vibration is induced in the Z axis, thus taking advantage of the d_{33}, which as can be seen in Tab. 2.1 is the highest for both AlN and PZT. As expected for a thickness mode, the thickness

of the device is going to determine the resonance frequency, according to:

$$f_s \propto \frac{1}{2T}\sqrt{\frac{E_p}{\rho}} \tag{2.12}$$

Thus, using for example the numbers from Tab. 2.1 the target resonance of 1GHz can be obtained with a thickness of approximately $5.3\mu m$, thus being compatible with thin film growth technologies. Unfortunately, as clear from Eq. 2.12, the resonance frequency is set by the film thickness, so it is impossible to realize devices with different resonance frequencies on the same wafer, without extra lithographic steps (thus increasing cost and decreasing reliability). However many techniques exists nowadays to achieve enough frequency shift to realize RF filters and duplexers ([47, 55]), and it is currently used in industry-level applications and thus constitutes the current state of the art in RF narrowband filter ([56]) together with Surface Acoustic Wave (SAW) technologies.

For the first application presented in this work (Sec. 3.3), FBAR technology constitutes a very good choice since single resonance frequency is required, spurious modes suppression is very well controllable, fabrication processes are mature and large actuation areas can be achieved with no significant degradation of Q, as will be discussed in the experimental section.

2.2.2 CMR

This class of resonators ([15]), known as *contour mode* or *lateral mode* ([48]) it is actually a container for many different modes of excitation, where the main difference with respect to BAWs is that the main coefficient that actuates the modes is a *transverse* coefficient, i.e. d_{31}. A transversal electric field $\vec{E}$ excites strains according to all the piezoelectric charge coefficients (Eq. 2.4) , the coefficient d_{31} will excite a stress on the *orthogonal* direction to the incident $\vec{E}$.

Generally lower k_t^2 is expected for these devices and so overall lower FOM than the FBAR counterpart (cfr. Tab. 2.1). Despite that, there is a growing attention to these modes, due to the *lithographic tunability* of the resonance frequency.
In fact it could be shown that for these lateral modes,

$$f_s \propto \frac{1}{2W}\sqrt{\frac{E_p}{\rho}} \tag{2.13}$$

Moreover, recent efforts ([45]) have shown that thanks two multi-dimensional modes higher

k_t^2 can be achieved, keeping a certain degree of tunability (30%) is shown in the previous work.

For the first topology proposed in Sec. 3.3, lateral modes are interesting mainly for the frequency tunability, which might lead to multi-band on-chip circulators. However the process was found to be too sensitive to fabrication errors and so no circulator was implemented using these devices. A new layout of resonators with wide frequency shift is currently being processed to implement the circuit proposed in Chap. 4.
For this other topology, where the frequency shift required between resonators is of the order of few %, this technology could be very beneficial, mainly because of reduced fabrication and design complexity with respect to the FBAR counterpart.

2.3 Fabrication Process

Different batches of MEMS resonators were fabricated during this work at the Kostas Research Institute clean room at Northeastern University. All the recipes have been fine-tuned for a 4μm AlN thin film process on a low-doped, high-resistivity polished 4-inches Si wafer.

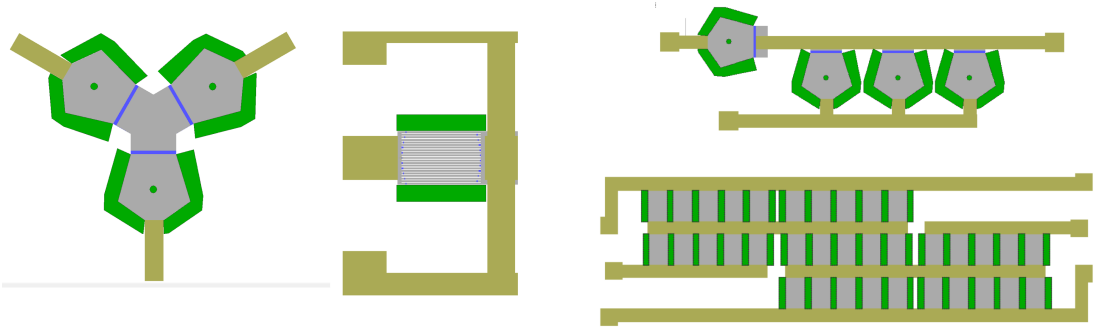

(a) *Layout of an FBAR Wye of resonators.*

(b) *Layout of a CLMR resonator.*

Fig. 2.4: *Some of the resonator laid out during this fab.*
The one on the right was used to implement a MEMS based circulator.

Each step will be analyzed in detail and pictures taken with an 50x magnification optical microscope will serve as a further description of issues and results.

Bottom Electrode Metalization. The first step consist in the photolithography of a 1.8μm positive resist spinned on a Si substrate. A promoter was spinned and baked on the wafer prior to the resist to ensure surface adhesion with the resist, and 1 min of the resist soft-baking at 115℃ dries the resist from water residuals. Photo Resist(PR) absorbance is increased as UV light is shined on the surface, so that the exposed part can be stripped off

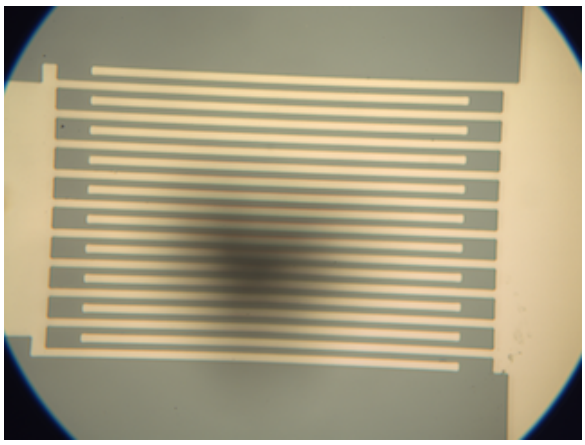

Fig. 2.5: *Picture of the patterned bottom electrode.*

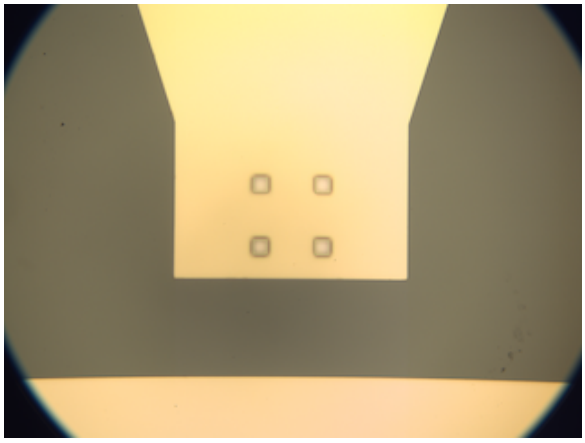

Fig. 2.6: *Picture of a lithographically defined via.*

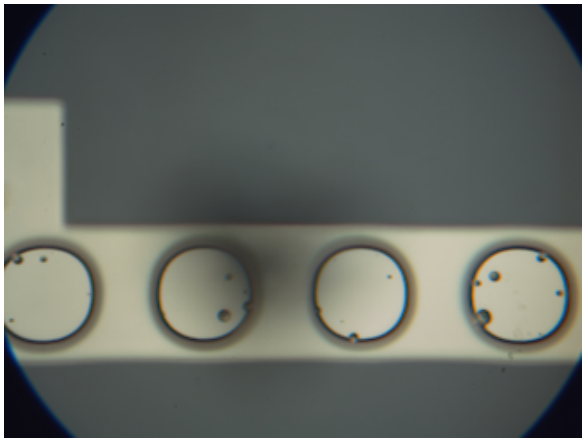

Fig. 2.7: *Picture of a wet etched via.*

with a chemical developer. Before the actual metal deposition, a stage of 0_2 plasma cleaning is required to remove additional organic material, which could contaminate the flatness and the uniformity of the wafer at this early stage. A 200 nm Pt layer was deposited on the wafer through thermal evaporation, and consequent lift-off removed the unexposed layer with PR. Double check of the deposited metal was performed with an interpherometric reflectometer (Nanospec).

AlN deposition. [002] oriented AlN is grown on top of the Si substrate in this stage. It is very critical in this stage that the metal traces underneath the AlN layer is uniform and flat, since any roughness or imperfect lift-off residual will increase the chance of local defects or deformation in the crystalline structure, which will strongly degrade the piezoelectric response in terms of k_t^2 ([51]).

Via Lithography and Etching. In order to access the bottom electrode, the AlN needs to be etched. Note that since a metallic contact needs to be created, a steep sidewall is not desired, so an isotropic etching is required. To create a mask a 2.7 μm PR is hard-baked

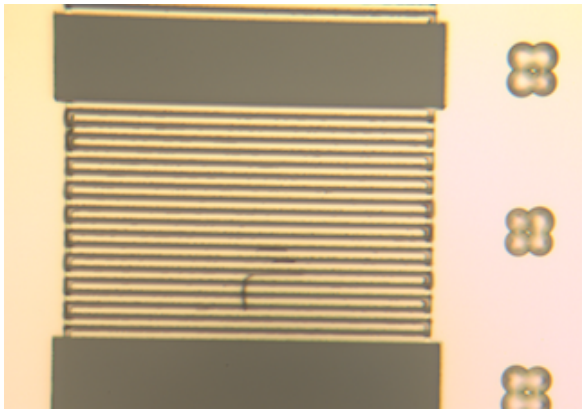

Fig. 2.8: *Picture of a TE metal layer.*

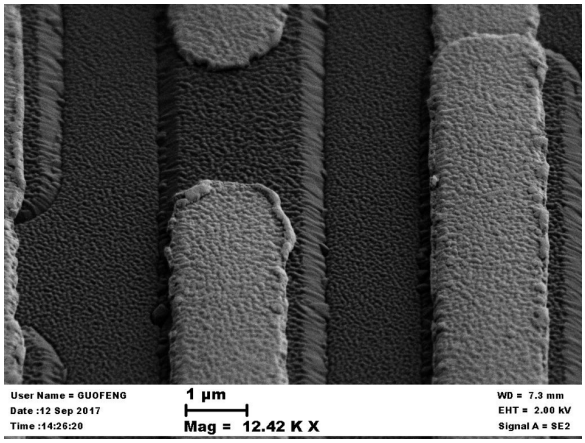

Fig. 2.9: *SEM detail of an aligned TE.*

after exposure overnight: in this way the unpatterned area will remain protected from the chemical etching that is performed in a phosphoric acid ($HP0_3$) solution.

Top Electrode Metallization. The upper electrode is now ready to be sputtered, after a lithographic process similar to the lower electrode. However here two main challenges arise: the metal stack will have to be deposited on the electrode and on the vias, so both of them have to be developed: this requires a delicate two step exposure where both timing have to be fine tuned. More importantly, as explained in Sec. 2.2, to reach RF resonance, finger pitch in the order of μm have to be fabricated, so submicrometric alignment is required. A Vernier scale ruler was adopted to achieve this result. A 300nm thick Pt was deposited with a 5nm Ti adhesion promoter layer. On top of that, a gold layer was deposited on the probing area, so to increase the chance of a successful wirebond and decrease the contact resistance.

AlN Trenches Etching. The AlN features have to be defined once that the resonator is

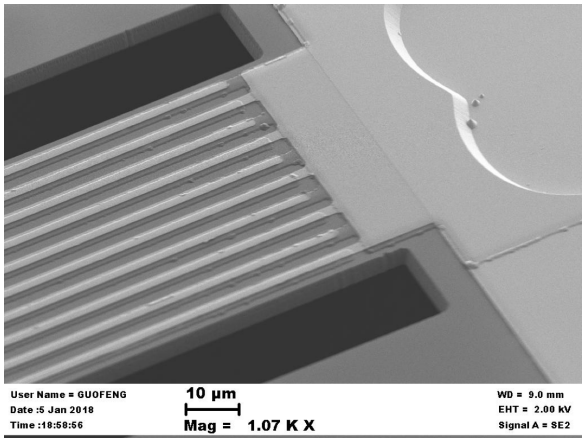

Fig. 2.10: *SEM picture of the AlN trench.*

defined: for this reason a very vertical sidewall is required, as many works ([50]) proved that finite-steepness is a reason of spurious modes and Q degrading. For this reason, a PR mask is not suitable, since the reflow that originates from the hard bake would compromise the dry etching. For this reason, a layer of silicon dioxide $Si0_2$ is deposited with a PECVD technique on the AlN surface, it is then selectively etched thanks to a highly anisotropic RIE process, so to be used as a sacrificial hard mask for the AlN etching. This is known to increase AlN surface roughness, which has a detrimental impact on Just now the AlN can be etched in Inductively Coupled Plasma (ICP) etcher.

Release. FBAR needs to be suspended to properly work in thickness mode vibration, and also CMR need to be suspended to confine the mechanical energy within the volume of the resonator (so effectively to increase its Q). Once the AlN is removed, the original Si substrate is now available to be etched away in a isotropic xenon difluorite(XeF_2) environment.

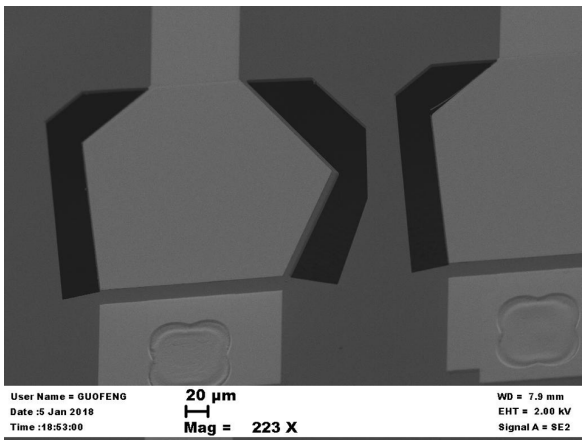

Fig. 2.11: *SEM picture of the FBAR used in the AMB cicuit.*

2.4 Resonators Characterization

Several devices were characterized and tested after the fabrication: in particular a wye of FBAR resonators was used to implement a circulator, as described in Chap. 3, and several resonators were used to study temperature sensitivity and DC bias sensitivity. Moreover, as explained in Sec. 1.1, nonreciprocal performances can be achieved when resonator tanks are modulated in time: thus DC biasing, thermal and optical actuation of a resonance frequency shift would be a viable[55] option to achieve nonreciprocity.

Frequency response for typical fabricated devices are shown in with parameters fitted from the model in Eq. 2.8. Note that in some cases (e.g. the CLMR shown) the effective Q is limited by the R_0 in the model, probably due to some adhesion imperfection in the via metallization.

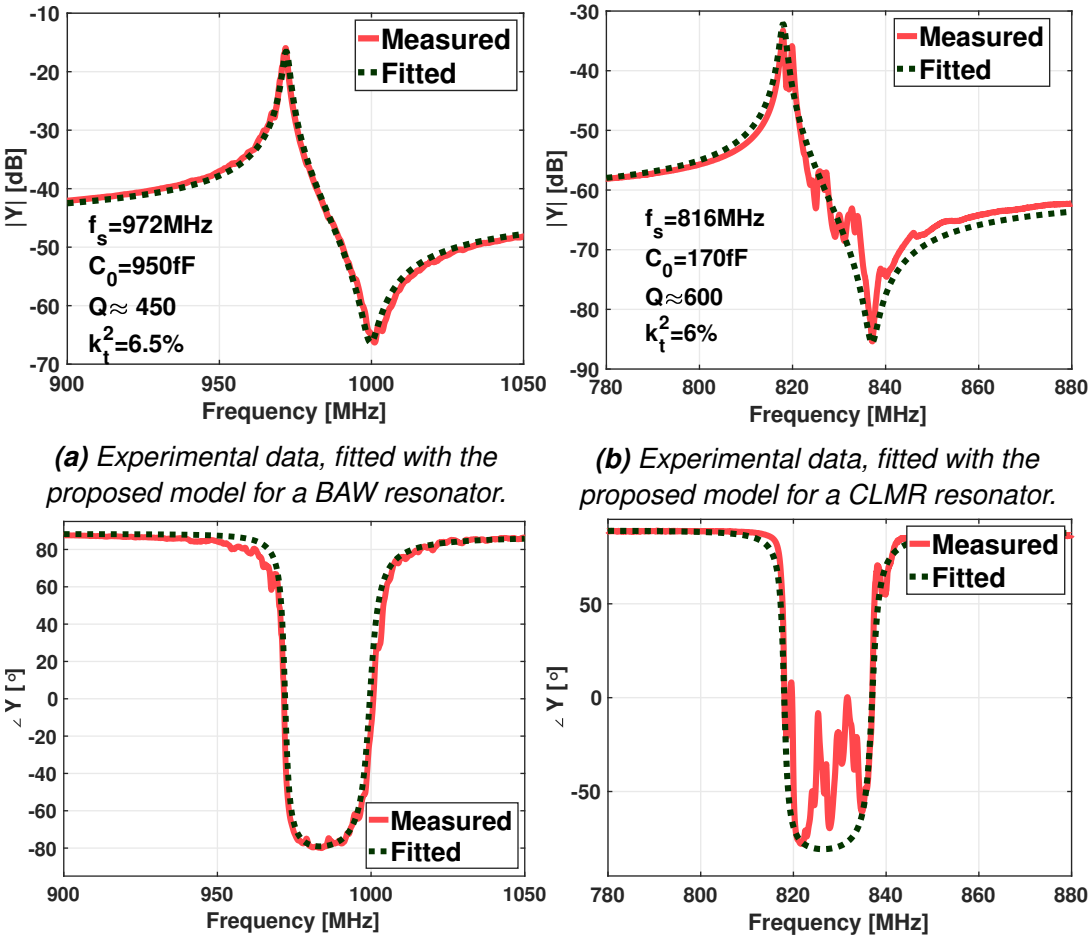

(a) *Experimental data, fitted with the proposed model for a BAW resonator.*

(b) *Experimental data, fitted with the proposed model for a CLMR resonator.*

Fig. 2.12: *Magnitude (top) and phase (bottom) admittance of fabricated devices during this work: as evident, the lateral mode device (right), even if interesting for the reasons in Sec. 2.2.2 was found to be unreliable and too much affected by spurious modes to be used in a system level design such an AMB circuit.*

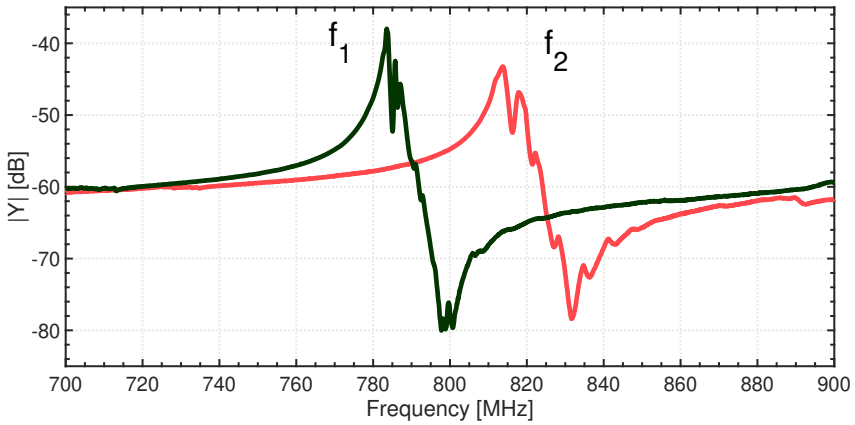

Fig. 2.13: *Fabricated devices with two different resonance frequencies, as predicted from the analysis in Sec. 2.2.2, with a pitch of* $W = 5.4\mu m$ *and* $W = 5\mu m$.

Since the AMB circuit requires three identical resonators connected as in Fig. 1.4, the BAW device solution was found to be more appealing, also considering the process tolerances and the early research stage in spurious mode suppression in CLMR technology.

However, on-chip multi resonance frequency was obtained after the process, as shown in Fig. 2.13.

A first attempt to induce a frequency modulation was assessed by using thermal and electrostatic actuation, as reported in [55]. However thermal and electric softening are not high enough to achieve the resonance frequency shift required in Angular Momentum Bias circuits, which will be shown in Sec. 3.1 to be in MHz range.

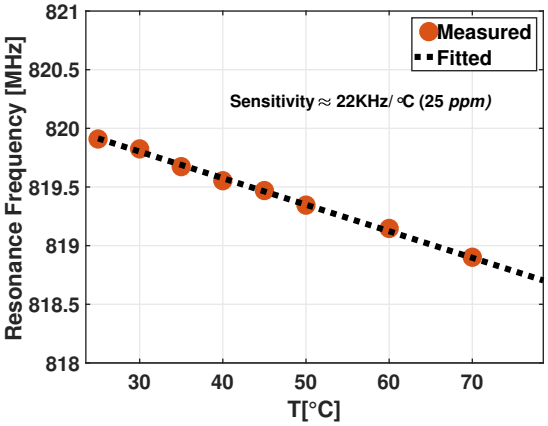

(a) *Resonance frequency shift as T is increased: sensitivity of 25 ppm was found.*

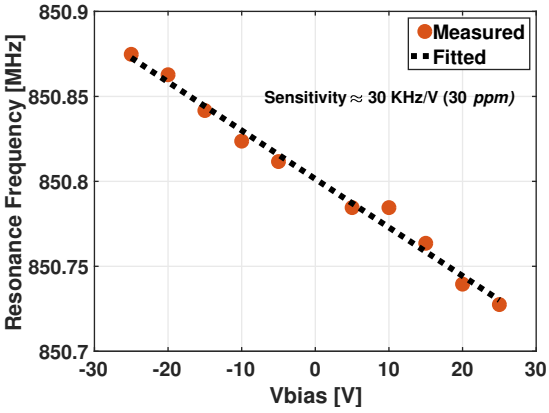

(b) *Resonance frequency shift as Vbias is increased: sensitivity of 30 ppm was found.*

Fig. 2.14: *Experimental collection of resonance frequency variation of the fabricated devices when Temperature (Fig. 2.14a) and DC bias (Fig. 2.14b) are changed for a 1 port CMR resonator.*

Chapter 3

Microacoustic Resonant Circulator

As shown in the previous chapters, Angular Momentum Bias (AMB) circuits show a trade off between the modulation frequency f_m and the Q_{loaded} of the system.
Specifically, it is always desirable to keep the lowest possible f_m, since the power consumption is typically scaling linearly with the latter. It is important to note that some other performances can be improved when requirements on modulation frequency are relaxed, such as linearity performances and image rejection. The first one is straightforward to asses: in standard CMOS switching techniques, the minimum power required to drive a switch with a C_g input capacitance with a V_{dd} square wave is typically found to be $P = C_g(V_{dd})^2 f_m$.

On the other hand, the image problem is a typical issue of modulated system in RF communication ([57, Chap.1]). If this aspect is negligible in the varactor excitation, it may become critical in switched excitation, as shown in the low-Q implementation in Fig. 1.12d. It is possible to see some tones folded from the "negative" side of the spectrum: these tones are less and less relevant as the ratio f_m/f_0 becomes smaller.
Moreover, as discussed in Sec. 1.3, the combination of MEMS technologies as resonant tanks and CMOS switches as Angular Momentum Bias actuation leads the way to a fully integrated, low-power, magnet less circulator.
This chapter describes the circuit analysis, the network modeling, the simulation and the testing results of a Microacoustic Resonant Circulator (MIRC).

3.1 Circuit Concepts in MIRCs

As reported in Sec. 2.2,piezoelectric RF MEMS resonator can count on Q values ranging in the thousand ranges, and in k_t^2 values ranging from 1% to 10%.
Moreover, as reported in [58] and as it will be shown throughout the discussion, the static capacitance C_0 and thus the MEMS area is typically set by matching conditions and in the order of

$$C_0 \approx \frac{1}{\omega_0 Z_0} \tag{3.1}$$

So for a reference 1GHz of central frequency, an electrical equivalent for an FBAR ($k_t^2 \approx 7\%$) MEMS resonator based on the model proposed in Eq. 2.4 would be:

Equivalent Lumped Component	Value
Motional Resistance (R_m)	2.8 Ω
Motional Capacitance (C_m)	56 fF
Motional Inductance (L_m)	445 nH
Parallel Resonance (f_p)	1.028 GHz

Tab. 3.1

As discussed in Sec. 2.2, actuating effective resonance frequency shift in piezoelectric MEMS resonator is an open challenge, expecially if one takes into account that a modulation speed in the $\approx 10MHz$ range is required.
It is very easy to observe, for example, that the sensitivity shown by typical devices fabricated in Sec. 2.3 which results in (Fig. 2.14) few *ppm* is not enough to cover the span required by this application. It will be found in fact, that shifts in the order of 2-3% will be required even in narrowband operation.
It is necessary to highlight that the parallel resonance, fundamentally due to the one port actuation, is the main source of losses and limitation for these class of circuits. This issue could be circumvented by using *two-port* excitation, as discussed in Sec. 2.2. However, in this case, the problem of how to excite a resonance frequency shift has not been solved, so the complete tractaction has been limited to the one-port case.

For this work, two main strategies were deployed to obtain a resonance frequency shift: a first one (Sec. 3.1.1) is a very simple network, which is lacking of inductors but it is inherently narrow band and tend to be lossy, at least when using AlN resonators. Another one instead (Sec. 3.1.2) relies on inductors to enhance the bandwidth of the MEMS resonator, thus allowing higher tunability.

Note that, like for Eq. 2.11, it is intended the *bandwidth* of the resonator as the relative distance from the series resonance to the parallel resonance, which is proportional to the

electromechanical coupling k_t^2.

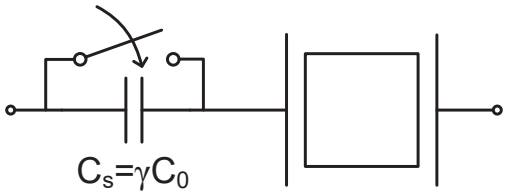

(a) *Schematic representation of a switched capacitor network that actively changes the capacitive load of the resonator in the switch OFF state, so to shift the resonance frequency.*

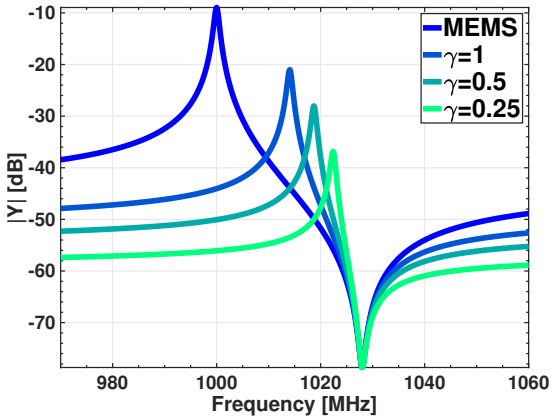

(b) *Numerical Simulation of the frequency shift associated to some typical $\gamma = C_s/C_0$ values. Note the characteristic admittance degradation described in Eq. 3.3.*

Fig. 3.1

3.1.1 Switched Capacitor Modulation Network

An first option that was proposed in this work relies on *capacitive* loading of the motional capacitance C_m: when the switch in Fig. 3.1 is closed the branch resonates at the nominal f_0 of the MEMS resonator.

When the switch is open, the switching capacitance C_s changes the reactive impedance thus effectively introducing a new resonant state $f_0^{(2)}$. Even if the values are relatively small, it is found that the f_0 shift can be controlled as a function of C_0, thus proving to be much more reliable, predictable and consistent shift.

Specifically, if one defines $\gamma = \dfrac{C_s}{C_0}$ in the schematic in Fig. 3.1, it is easy to find that, when the switch is in the ON state, the resonance frequency $f_0^{(2)}$ can be written as:

$$\frac{f_0^{(2)}}{f_0} = \sqrt{1 + \frac{8}{\pi^2}\frac{k_t^2}{1+\gamma}} \tag{3.2}$$

The result is indeed reasonable: if the switching capacitance C_s is much larger than C_0 ($\gamma \ll 1$) then the two states collapse into a single f_0 resonance. If viceversa C_s is much smaller than C_0 ($\gamma \to 0$), then the resonance is canceled and the two states again collapse in a purely capacitive response.

It is important to notice that this modulation scheme introduces different losses in the two states of operations: in fact, if the admittance during the ON state of the switch $\left|Y_{peak}\right|$ are limited essentially by the $FoM \propto k_t^2 Q$ as described in Eq. 2.8 of the resonators, in the OFF state a γ dependent reduction of admittance $\left|Y_{peak}^{(2)}\right|$ can be modeled.

With classic impedance manipulation, it is possible to find:

$$\left|Y_{peak}^{(2)}\right| = \left(\frac{\gamma}{1+\gamma}\right)^2 FoM \cdot Y\Big|_{LF} \tag{3.3}$$

Interestingly, once the FoM of the resonator is assessed, it is possible to evaluate the impact of the *relative admittance degradation* with a simple factor χ:

$$\frac{\left|Y_{peak}^{(2)}\right|}{\left|Y_{peak}\right|} = \chi = \frac{\gamma^2}{(1+\gamma)^2} \tag{3.4}$$

To have a grasp of the frequency variations of interest, some numbers are reported Tab. 3.2 for a $k_t^2 = 7\%$ and $C_0 = 3.2pF$:

γ	$\mathbf{f_s^{(2)}/f_s}$	**Admittance Degradation**	**Switching Cap**
1	1.4%	12 dB	1 pF
0.5	1.8%	19 dB	0.5 pF
0.25	2.2%	27 dB	0.25 pF

Tab. 3.2

As clear, a significant trade-off is imposed between obtaining the necessary frequency shift while maintaining a low admittance degradation factor.

As a rule-of-thumb design derived from the model in Fig. 1.7, for a $L_m = 450nH$ an optimal design region would be the couple $f_m/f_0 = 1.6\%$ and $\Delta C/C_{ave} = 4\%$ so that, if one assumes $\Delta\omega/\omega_0 \approx \Delta C/(2Cm)$, then the design optimum should require $\gamma \approx 0.25$.

This will result in extra losses and/or sub optimal nonreciprocal response, as will be highlighted in the simulation section.

3.1.2 Enhanced Switched Capacitor Modulation Network

Another approach, which can relax the constraints described in the previous configuration is the one shown in Fig. 3.2, where the main idea is to use a *shunt* inductor to the resonator,

so to move away the parallel resonance which is highly detrimental for the MIRC.

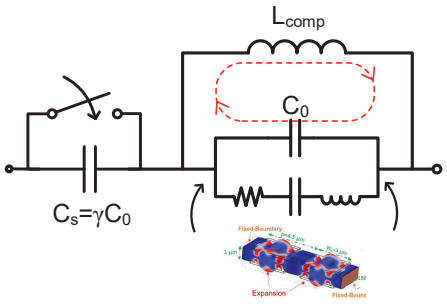

(a) *Schematic representation of a modified switched capacitor network where the inductor effectively enhances the resonator bandwidth so to increase the resonance frequency shift and minimize the admittance degradation χ.*

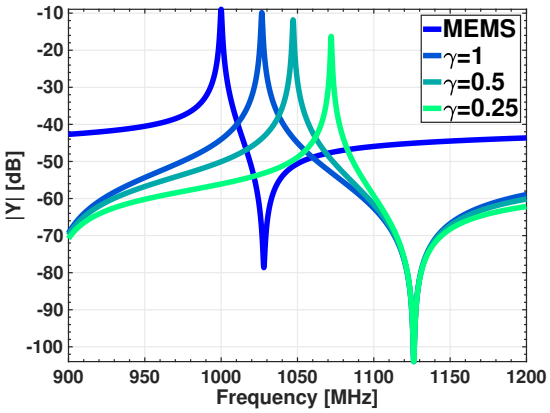

(b) *Numerical Simulation of the frequency shift associated to some typical $\gamma = C_s/C_0$ values for this modified network. Note that that the admittance degradation is considerably lower than in Fig. 3.1*

Fig. 3.2

A rule of thumb for the design of the inductor can be expressed as follows: if the L_{comp} is found to be in *parallel* resonance with the static C_0 of the MEMS at the same *series* resonance of the device, then in the neighbour frequencies the whole device can be seen as a *perfect* series resonator, thus extending the bandwidth.

A full analysis of the impedances into play would reveal that the *maximum* bandwidth extension (where for bandwidth is intended the distance between a series and a parallel resonance) it is found exactly for the condition

$$L_{comp} = \frac{1}{\omega_0^2 C_0} \tag{3.5}$$

For example, for a $C_0 = 3.2pF$ one would need an $L_{comp} = 8nH$. In the proposed experiments with a $C_0 \simeq 1pF$ a discrete $25nH$ inductor was used.
By looking at Fig. 3.3 it can be observed that the inductor introduces an additional zero in the $|Y|$ curve. The condition Eq. 3.5 corresponds to the point where the the MEMS resonance is the median point between the two zeros. Also in this case the overall bandwidth depends on the k_t^2, but the characteristic relation can be written as

$$\frac{f_z}{f_0} = \frac{1}{2}\left(\sqrt{\frac{8}{\pi^2}k_t^2} + \sqrt{4 + \frac{8}{\pi^2}k_t^2}\right) \tag{3.6}$$

It is possible now to compare Eq. 3.6 with Eq. 2.9 to have a grasp of the bandwidth

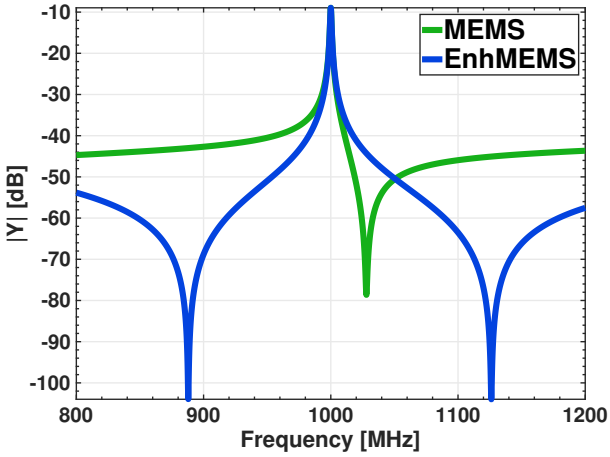

Fig. 3.3: *Bandwidth increased according to Eq. 3.6: for example, for a resonator with k_t^2=7%,which has a 3% fractional BW, this will result in a enhanced BW of 12.5%.*

enhancement: while in the *simple* case of a MEMS resonator a fractional bandwidth of 2.8% is associated to a $k_t^2 = 7\%$, for an *enhanced* resonator a 12.6% can be predicted.

It is crucial to observe at this stage that the circulator losses and the dynamic response will not be affected by the inductor L_{comp}, since it is supposed to work in a frequency span where it is actually behaving as an open circuit. Moreover is not in series to the signal path, so it cannot introduce resistive losses due to the finite-Q, like in the LC circulator analyzed in Sec. 1.2.

Also in this case it is possible to derive an analytical expression for the resonance frequency shift in the OFF state of the switch as a function of the ratio $\gamma = \frac{C_s}{C_0}$:

$$\frac{f_0^{(2)}}{f_0} \approx (1 + \frac{\pi^2}{16}\frac{k_t^2}{\gamma})$$

Tab. 3.3 reports typical χ values, so that one can compare them with the values found in Tab. 3.2.

γ	Relative Frequency Shift	Admittance Degradation	Switching Cap
1	2.6%	0.8 dB	1 pF
0.5	4.7%	2.8 dB	1.5 pF
0.25	7.2%	7.3 dB	0.25 pF

Tab. 3.3

3.2 Simulations and MEMS based designs

Assessing the optimal performances of these switching circuits requires at least a couple of expedients in SPICE engines as simulation tools.

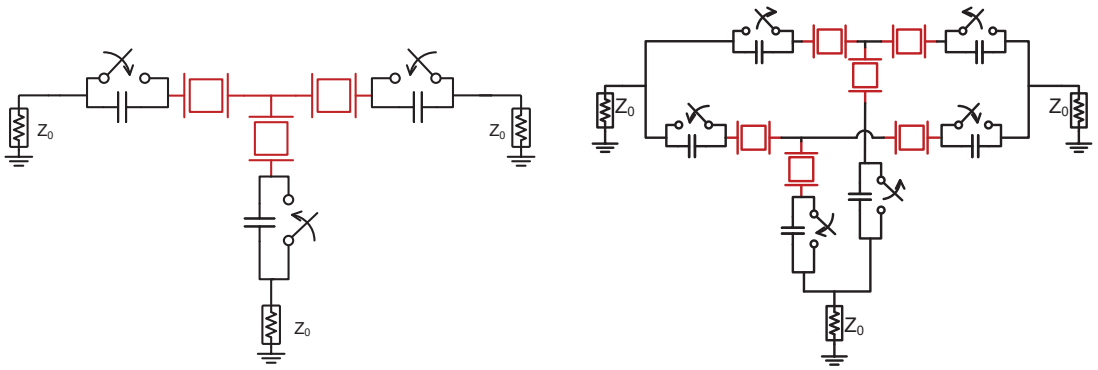

(a) *Single Ended version of a MIRC* ***(b)*** *Differential version of a MIRC*

Fig. 3.4: *Two different implementations of a MIRC*

An Harmonic Balance (HB) engine simulator was chosen, so to have a direct representation of the system response in the frequency domain, as every common RF application.

This system can be effectively regarded to as a double frequency converter (Fig. 1.5) which upconverts the signal at the first port, and down converts it at the second port. This process can easily generate a number of intermodulation products (IM), as discussed in Sec. 1.4, and the minimum number of harmonics required by the HB engine to correctly assess the S-parameters of the system may vary accordingly to all the design parameters.

So a number of rule of thumb actions were taken when trying to evaluate the performances in the simulation stage, also according to the MEMS technologies that were planned to use at this stage:

1. $Q = 1000$ and $k_t^2 = 7\%$ for a $FoM = 70$. These are worst case scenario for state of the art MEMS resonators based on FBAR technologies (Sec. 2.2.1).
   When instead using lateral vibration modes (Sec. 2.2.2) these values are slightly optimistic: even if similar values were shown ([45]) these technology is not yet mature enough to guarantee reliable performances.

2. negligible R_0, R_s (Fig. 2.2) was assumed. These values are often relevant for very large devices devices ([59]) where the stray elements might become comparable to the motional resistance R_m of the resonator. Careful layout, extra metal layers as described in Sec. 2.3 and large vias can mitigate the impact of this issue.

3. The switches were approximated with an ideal nonlinear component as reported in [60],with about a 10^5 ratio of ON/OFF resistances.

4. A minimal number of 20 harmonics were taken into account for each switch voltage control signal, and at least 15 tones were use to simulate IM products.

5. The resonator actuation area (proportional to the physical capacitance C_0 can be chosen taking into account the relations discussed in Sec. 2.2. Specifically, a $C_0 = 900fF$ guarantees a $L_m = 500nH$ and $R_m = 3\Omega$, which is a good compromise between low static loss and high Q operation ($Q_{load} = 60$).

Throughout the rest of the work, differential implementations of AMB circuit will be presented: the resulting performances can be quite similar in terms of nonreciprocal contrast, but the differential version clearly shows lower IL and better spectral purity thanks to the cancellation mechanism discussed in Sec. 1.3.

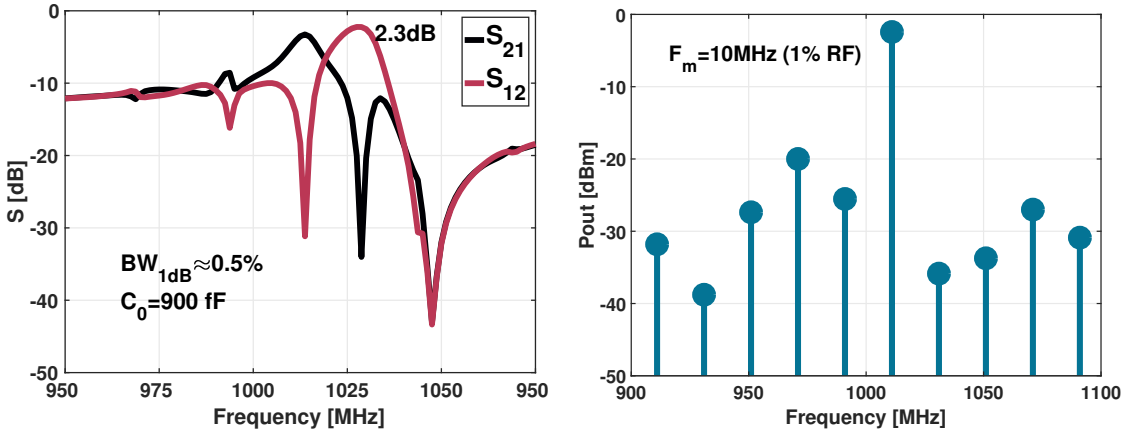

(a) *S-parameters simulated in Differential Wye configuration.*

(b) *Transmission Output Spectrum for* $P_{in} = 0dBm$.

Fig. 3.5

Some typical results are shown in Fig. 3.5, and they display already the main drawback of this circuit: the high frequency admittance zero, which as discussed in Sec. 2.2 is originated by the one port actuation of the mechanical resonance mode, is limiting the bandwidth of nonreciprocal operation to a fraction of the k_t^2. In this specific simulation a -1dB IL bandwidth(BW) of about 5MHz is shown, thus recasting a 0.5% fractional BW, which is definitely too small for any communication application.

This limit cannot be overcome with this circuit, unless having access to a higher k_t^2 technology.On top of that, this circuit has another critical parameter: in recent fabrication processes it has emerged that the increase of actuation area of laterally vibrating MEMS resonators has a negative impact on the quality factor of the device ([46]). This is a major limitation for

CMR MEMS devices, which is one factor currently prohibiting the access of this technology in the RF filtering market.

This issue, however, can be assessed using a simple $\Delta - \Gamma$ conversion of the main core of each of the two complementary branches.In fact, by just arranging the resonators in a Δ configuration rather than the previously proposed Γ, the capacitance C_0 can be reduced by a factor 3 without affecting any of the other performances. Note, in fact, that a *static* impedance equivalence between the two circuits exists: the simulations in Fig. 1.4 show very similar response, both in terms of bandwidth of operation and typical Insertion Loss.

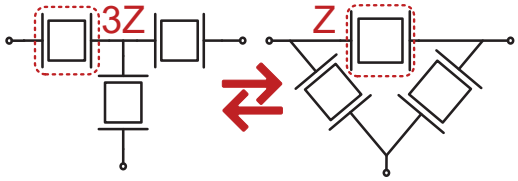

(a) *MEMS resonators: $\Delta - \Gamma$ conversion.*

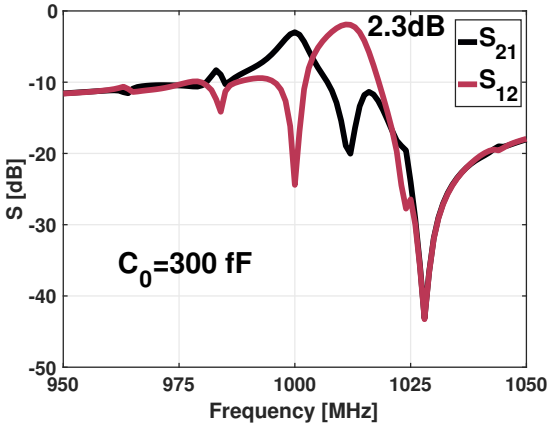

(b) *Simulated S-parameters for differential Δ MIRC.*

Fig. 3.6

This is an easy way to spare a third of area consumption, with no power consumption increase and at the only cost of increasing of a factor 3 the switching capacitance C_s.

Note also that, despite the values predicted by the model in Fig. 1.7, the modulation frequency here used is sensibly smaller of the optimal one predicted for a $Q_{loaded} \approx 60$ (about 0.5% predicted versus 0.1% simulated) .This is some hint that the zero generated by the electromechanical coupling (whose distance from the resonance, as shown in Sec. 2.2 is proportional to k_t^2) further decreases the requirements in terms of modulation frequency.

However the main limitation for these kind of topologies remains the bandwidth limitations introduced by the high frequency admittance zero. This is really the reason why the S-parameters are so distorted with respected to the results obtained experimentally in other topologies based on switched LC circulators (Fig. 1.12). As explained in Sec. 3.1, an easy solution which still relies on high-Q MEMS resonators is the one based on shunting the resonator with an inductor, so to move to higher frequencies the in-band zero. The mechanism is evident from the numerical result shown in Fig. 3.3, where a bandwidth extension can be found thanks to the upshifting of the admittance zero, according to Eq. 3.6.

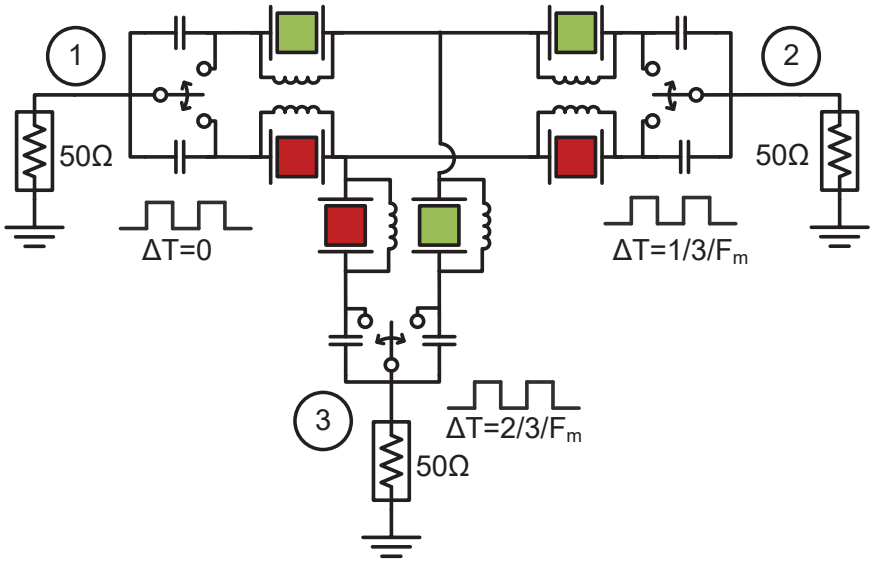

Fig. 3.7: *Complete schematic of the differential Wye Circulator based on enhanced MEMS resonators.*

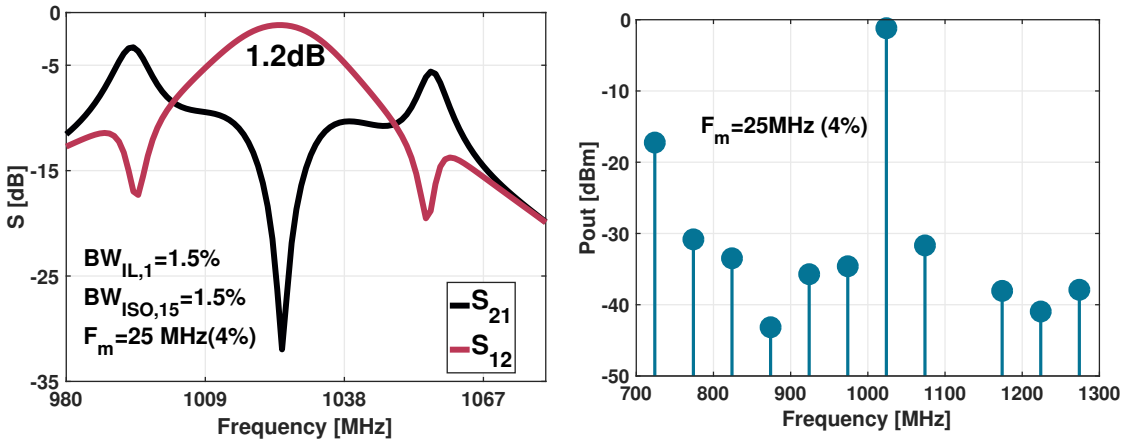

Fig. 3.8: *S-parameters and output spectrum simulated for the circuit in Fig. 3.7*

.

As a result of that, this simple circuit shows a very promising result, almost compatible with communication bandwidth and easily scalable to higher and higher frequencies.

As explained in [4, 13], a suppression of IM products of less than 20Bc is not enough for mobile communications, as these output tones would be radiated into the channel, causing jamming and inevitably degrading the SNR of already faint RF signals, as discussed in the introduction. Moreover, any asymmetry, frequency mismatch or component mismatch will inevitably degrades all the performances, specifically the IM rejection and the three port symmetry.

For these reasons MEMS resonators in RF domain are gaining more and more attention as basic building blocks for RF filtering ([46, 47, 61]) due to their high skirt steepness, which is a direct consequence of their typical high-Q antipeak, strong near-band suppression, and low IL, which is inversely proportional to the resonator FoM. These properties were found during this work to be necessary to further suppress the IM products generated by the circuit, but this last step will be assessed in the following chapter.

After a first period when the model of the circulator discussed in Sec. 1.2 was developed and the different topologies for the MEMS based circulators were explored through intense simulations across diverse platforms, this work was focused on realizing circuits on PCB to effectively test the performances predicted in the simulations exposed in the previous sections.

Some first preliminary experiments confirmed the critical aspect that simulations could not grasp during the first stage of the work. Among them, some of the most critical issues when trying to implement such circuits in a discrete components PCB were:

Switch Technology.

The requirements for switches employed in this circuit are very stringent.
In all of the implementations, Single Pole Double Throw (SPDT) topologies were adopted to fulfill with differential topology (i.e. Fig. 3.6).
Following from the discussion and the numbers required by the simulations in Sec. 3.2 these performances have to be met:

- Reflective Open topology. This represents a first issues, because for switches with cutoff frequencies above 2GHz most of the commercially available devices are either *absorptive* or *reflective short*(Fig. 3.9). The first one essentially display a 50 Ω termination for the isolated branch, the second one displays a Short Circuit (SC) to ground behaviour in the off state.

- Insertion Loss. At least two switches are present in the RF transmission path, so each of them will contribute to circuit loss, at least from the finite switch R_{ON} and the nonideal input matching. Typical IL for the best compliant devices were found to be from 0.5dB to 1.5dB, mainly because of non ideal matching to 50 Ω, so expected losses from the switch are expected to be from 1dB to 3dB.

- Off State Resistance. To prevent RF current to flow into the off state branch in all the circuit presented, a significant OFF state resistance is required. In simulations a conductivity modulation in the 10^4 was used, while the best values of Off state TX are in the 60dB range, corresponding to a 10^3 order of magnitude. However this value is not so critical in 50 Ω systems.

- Switching speed. This is really the most critical parameter for MIRC: the switch has to provide a very good IL at RF frequencies, and it has to be able to change state at a switching rate in the 25 MHz range (Fig. 3.8). To ensure low switching losses, a reasonable requirement for the switch rise-time should be in the nanosecond range. This highly limits the choice of switches available on-the-shelf ([62–64]) resulting in extra-loss induced by the switch risetime.

- Power Handling. This is another very critical parameter in RF applications: the switch R_{on} has to be kept constant (and much smaller than 50 Ω for input voltages approaching the FET threshold. For this reason a large C_{gs} is required, and a *gate resistance* R_g in the $k\Omega$ range is typically placed in series to the gate(Fig. 3.9 so to *float* the RF voltage across the FET gate-to-source junction. This clearly poses a limit to the switching speed, hence the trade off with switching speed as highlighted above.

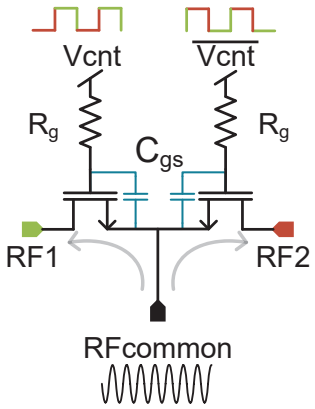

***(a)** Schematic of a Reflective Open Switch.*

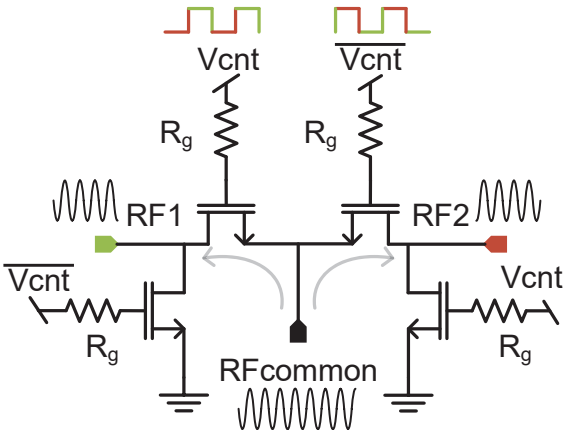

***(b)** Schematic of a Reflective Short Switch.*

***Fig. 3.9:** Different Implementations of RF Switches.*

To better emphasize the parasitics introduced by the switches in the ON state, a fitting of the ON state S-parameters was derived in the TX path. As can be seen in Fig. 3.10 the switch parasitics (the *parasitic capacitance* in particular) are not only comparable to the MEMS capacitances, but can be dominant when combined as in the MIRC schematic.

PCB design.

This system naturally behaves better when the physical dimensions of the lines connecting the components are very small: in fact in the inner core of the MIRC it is not possible to guarantee a 50 Ω matching across the whole region of operation, since the switching system inherently modifies the system impedance in a time-variant

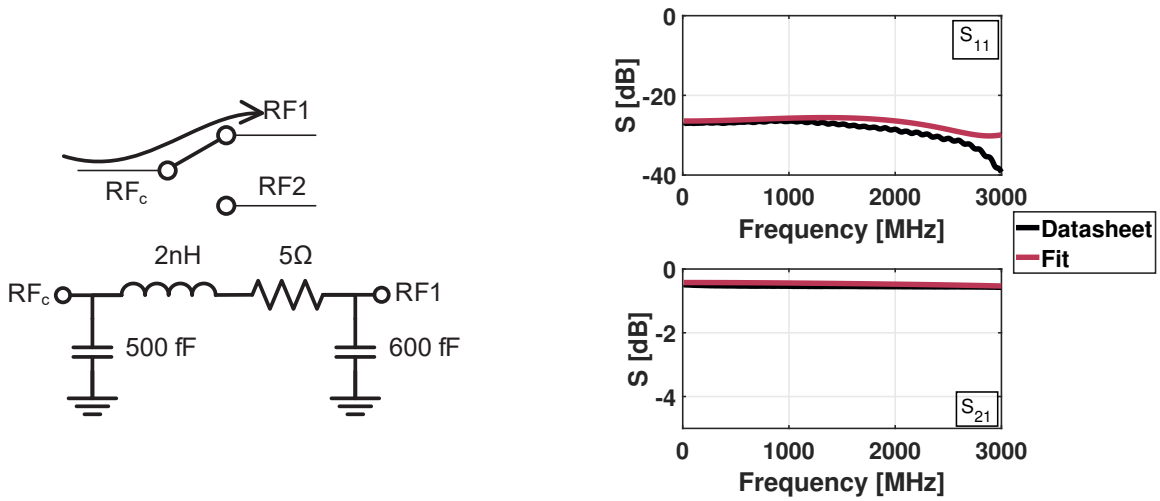

Fig. 3.10: *First order fitting for a RF SPDT switch in the TX path. As will be evident during the experimental result discussion, switch parasitics, being comparable to the MEMS capacitances in the circuit can significantly degrade the circuit performances (Fig. 3.14a).*

fashion (differently from the previous varactor based implementations). So very careful design is needed from the PCB traces, and minimizing traces length is a critical issue in the switching network. On top of that, to maximize the circuit simmetry, it was chosen to implement the two branches on *two sides* of the same PCB. The two branches were connected through circular vias.

Another size constraint was represented by the minimum feature that could be diced in the cleanroom: being a user-operated process, chip-processing is not possible, so the minimum feature that can be diced is around *1cm x 1cm*. This will result in unavoidable extra losses and parasitic inductance resulting from the long wirebonds needed. In order to provide solid ground to both sides of the PCB (implemented with just 2 metallizations, top-bottom metal on a Roger dielectric) a grounded coplanar waveguide trace was chosen.

MEMS characterization.

During the layout, three resonators were arranged as shown in Fig. 2.4, in a convenient way to be used in the configuration shown in Fig. 3.4. Unfortunately this prevented the characterization of each single resonator, which was a potential loss of information about the actual performance of each MEMS device. Similar devices were tested to have a rough estimation of the performance in that area of the wafer, so we extracted initial values comparable to the ones shown in Fig. 2.12a.

System-Level Modeling.

From the schematics proposed in Sec. 3.2, it is clear that to have reliable and realistic simulation, a complete simulation platform would be required: being the switch the

time-variant element, a detailed model of the device from a technology level (which is a FET on GaAs substrate for most available switches) should be accessible.
Moreover, an EM simulator was needed to optimize the PCB traces and evaluate the impact of the PCB on the circuit performances.

To sum up, a complete and reliable simulation platform was not achieved when trying to simulate the complete response of the dynamic PCB, mainly for the lack of access to a technology based model of the RF switch. Two implementations are going to be shown: a first one (Fig. 3.11a) based on the FBAR resonators fabricated during this work, operating around 1GHz, and another one (Fig. 3.11b) based on FBAR resonators provided by Broadcom, operating around 2.5 GHz.

Note that for both the implementations, inductors were actually placed in *Delta* configuration, so not to avoid to access the central node where all the MEMS are connected. Once again, the $\Delta - \Gamma$ conversions easily semplify a very tedious problem (cfr. Fig. 3.6a).

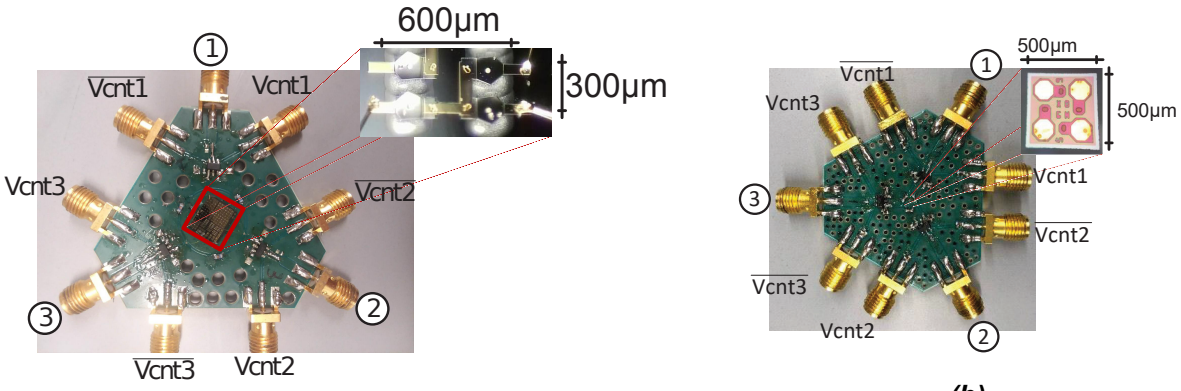

Fig. 3.11: *Pictures of two implemented PCB of a MIRC, the first with the in-house built resonators fabricated as discussed in Sec. 2.3, the other one based on commercially available FBAR resonators provided by Broadcom.*

3.3 Experimental Results

3.3.1 Implementation 1: MIRC using fabricated resonators

As briefly mentioned above, one of the practical difficulties of implementing a MIRC starting from fully in-house fabricated devices is the actual testing of resonators laid out in Fig. 2.4, since they cannot be singularly tested with calibrated sources. The only possible way is to de-embed the measures from three port static S-parameters of the circulator, already mounted on the PCB.
This actually limits the degree of control on the effective performances to a very mild fitting. Also note that it is impossible to discriminate small f_s variation across the two different chips realized to implement this circuit.

The results of the fitting are shown in Fig. 3.13, and it is clear that with these level of losses the performances will not be as performing as the ones predicted in the simulation in Sec. 3.2. The Q is significantly smaller than the expected results, and spurious modes will degrade the whole frequency response in the dynamic simulations, but this is very hard to predict from simulations.

However, after many trial and error implementations, with different switches and different switched capacitors, the best performances obtained are shown in Fig. 3.14a. Note that for all the implementations of MIRC the measured input reflection is always under the -15dB in the bandwidth of operation.

It was possible to collect multiple datas that were rearranged to highlight trends and possible issues ignored during the simplified simulation environment. The results are shown in Fig. 3.14.

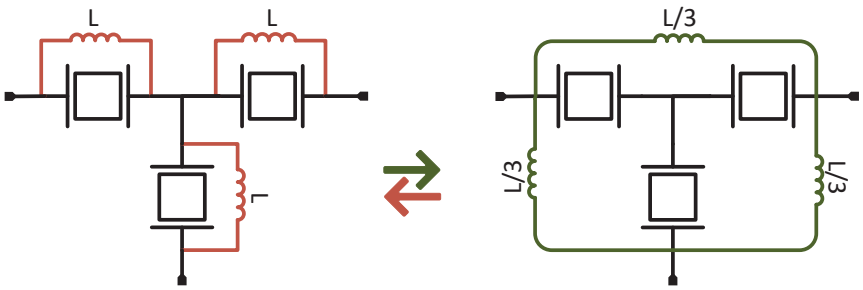

Fig. 3.12: *Schematic of the practical implementation of the MIRC cores in the PCBs implemented in Fig. 3.11. Once again the $\Delta - \Gamma$ conversions are very useful when implementing these three port devices.*

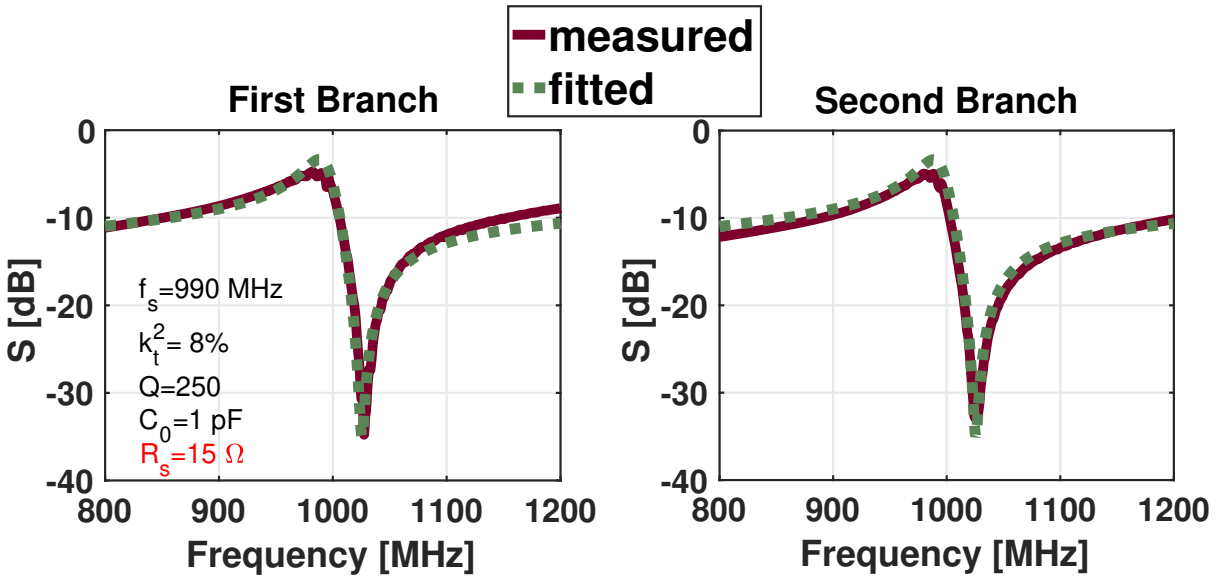

Fig. 3.13: *Static S-parameters, measured to have a grasp of the performances associated to the resonators used in this first MIRC. The resulting performances can be confronted with the ones in Fig. 2.12a. The Q is significantly low (almost a factor 3 lower than the single structure tested with calibrated probes). This might be due to the long wirebonds necessaries to access the devices, or to PCB losses, or to some device-level via malfunctioning.*

The linear trend highlighted in the model discussed in Fig. 1.7 is clearly visible in the Isolation scatter for both the implementations, while the optimal condition for the Insertion Loss is unclear, probably to switch parasitics that interfere with the dynamic response of the circuit.

As Fig. 3.12 highlights, to implement the second topology proposed in this chapter, referred to as *enhanced resonator* topology, it is required just to add inductors to the same PCB. An highQ Coilcraft inductor ([20]) with a $\simeq 23nH$ inductance was used to resonate out the C_0 as discussed in Sec. 3.1 to enhance the resonator bandwidth. The results are shown in Fig. 3.15a. Note that the IL peak is increased of about 0.5dB in the case where the *enhanced resonator* is used, in a similar way of what was described in the simulations run in Sec. 3.2.

Also for this second topology, based on *enhanced resonators*, a parametric analysis was performed, and the peaks of IL and ISO were compared in the scatter shown in Fig. 3.15. As expected, trends are very similar in the two cases, but obtained bandwidth in this case (Fig. 3.15a) is larger, and so is the modulation frequency.

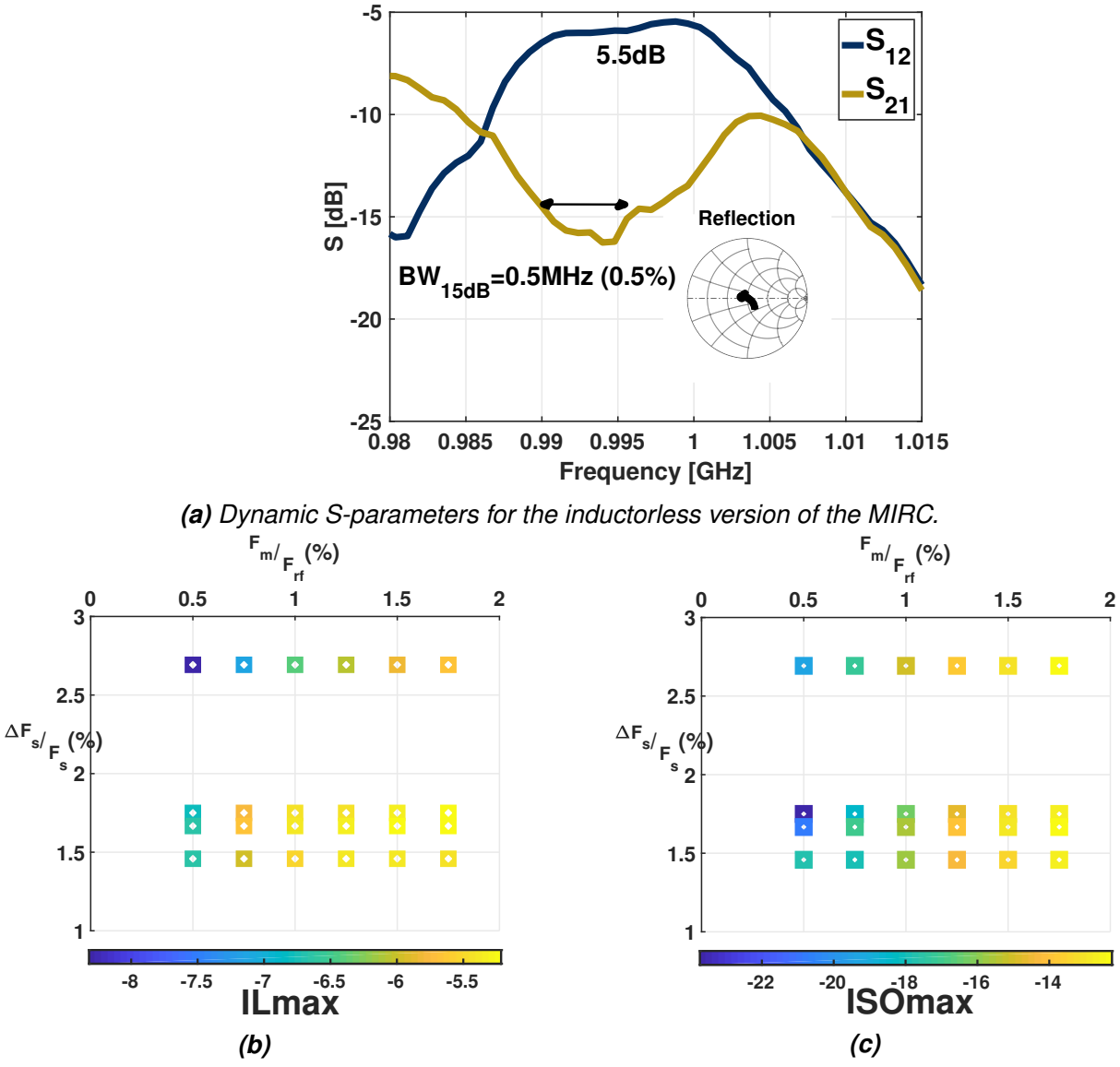

(a) *Dynamic S-parameters for the inductorless version of the MIRC.*

(b) ***(c)***

Fig. 3.14: *Scatter plot of the measured peaks of Insertion Loss(IL) and Isolation(ISO) for various conditions of modulation frequency and switched capacitor for the inductorless circuit.The quantity $\Delta F_s/F_s$ is evaluated starting from Eq. 3.2 by knowing the switched capacitor. Typical S-parameters are reported in Fig. 3.15a. Here, a capacitor of 1pF is switched at a switching speed of 10MHz (1%of the RF frequency) to obtain an effective 15dB isolation of 5MHz, corresponding to the 17% of the resonator bandwidth.*

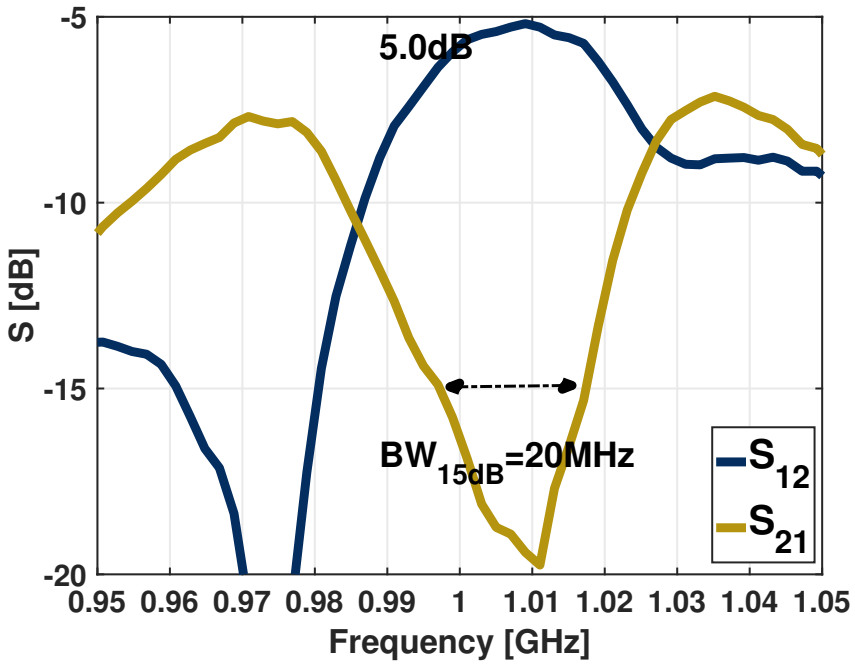

(a) *Dynamic S-parameters for the enhanced version of the MIRC.*

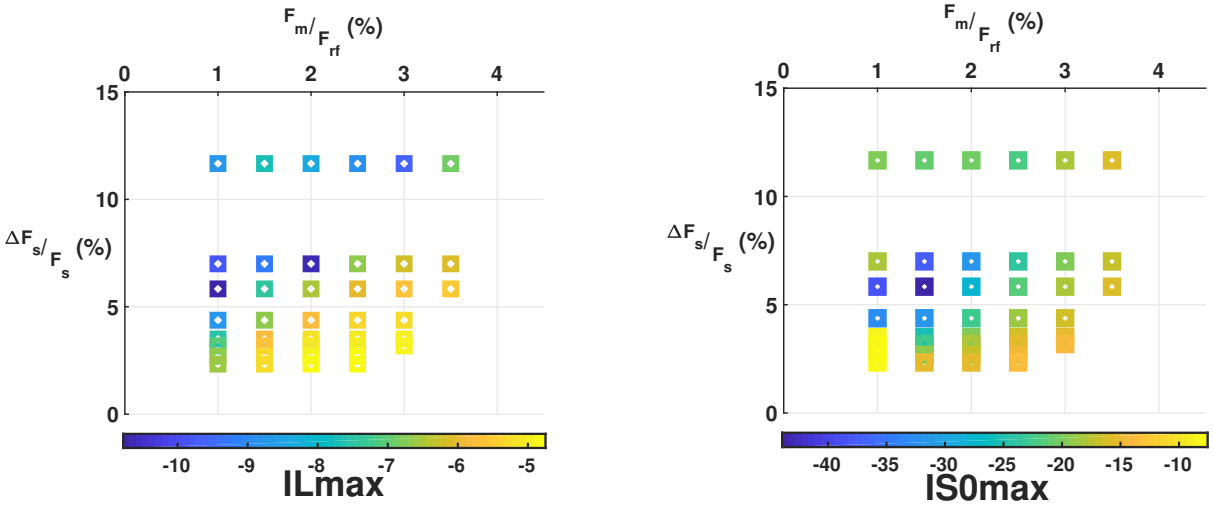

(b) ***(c)***

Fig. 3.15: *Scatter plot of the measured peaks of Insertion Loss and Isolation for various conditions of modulation frequency and switched capacitor in the* enhanced resonator *topology. The quantity $\Delta F_s/F_s$ is evaluated starting from Eq. 3.6 in the case with inductor by knowing the switched capacitor. S-parameters for $f_m = 25MHz$ are reported in Fig. 3.15a. Here,a capacitor of 1pF is switched at a switching speed of 20MHz (2%of the RF frequency) to obtain an effective 15dB isolation of 20MHz, corresponding to 75% of the resonator bandwidth.*

3.3.2 Implementation 2: MIRC using commercial resonators

When searching high power handling resonators that could fit our applications, we had the chance to work with some of the state-of-the-art FBAR resonators, provided by a wordwide renowed MEMS company, Broadcom INC[65].

These devices were found to be significantly linear, as will be shown later, they had almost no evident spurious tone (as can be seen in Fig. 3.16) and they displayed less than 3MHz f_s spread around the central frequency. For this reasons they were the best candidate so far for a MIRC.

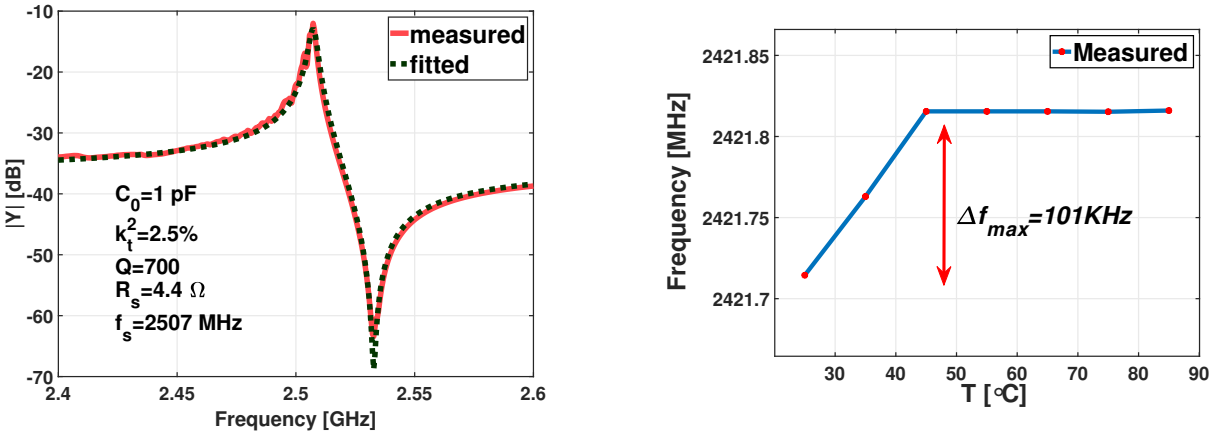

Fig. 3.16: *Fitting of a temperature-compensated Broadcom FBAR operating at 2607MHz. Several wye connected resonator like this one were provided for this application, and despite the poor k_t^2 (probably due the temperature compensation) an overall good performance can be obtained in terms of loss, thanks to the high Q of the system (almost four times larger than the one obtained in our in-house process).*

Moreover, the chips were diced in an industry level facility, so they had a very small footprint, so that a smaller PCB was designed for this purpose, allowing to reach even lower losses and shorter wirebonds.

However our testing tools to drive the IC switches have a limited maximum output frequency (50MHz), so as the device resonance moves to higher frequencies, limited capabilites to actually drive the switches can affect switching losses and sytem overall symmetry. In fact, a close-to-the-edge 40MHz square wave signal was required in this implementation. Even if constituting just 1.5% of the RF frequency, the simmetry of the system was not found to be satisfactory (Fig. 3.17). Like in all of the other cases, extra losses are associated to the switch R_{on} (0.5dB to 1dB each), finite risetime losses and PCB losses for an overall 2dB extra losses with respect to the ideal simulations.

The results of the enhanced MIRC are shown respectively in Fig. 3.17 and Fig. 3.18.

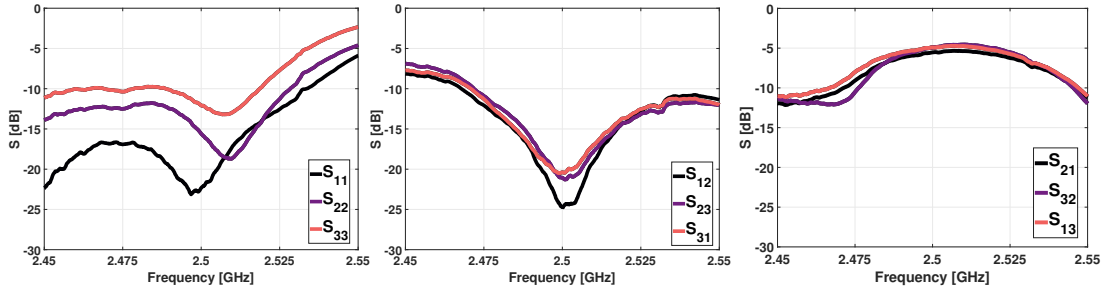

(a) *Reflection performances for the MIRC* ***(b)*** *Isolation performances for the MIRC* ***(c)*** *Insertion Loss(IL) performances for the MIRC.*

Fig. 3.17: *Full characterization of Three Ports S-parameters for the second implementation of a MIRC.*

As instead some small manual tweaking of the driving phases (in the order of $\Delta\phi \pm 10°$) was explored, very good performance were observed.

This is either a hint of a slight asymmetry in switches, or some tolerances in the discrete components used in the PCB, or the correction of a systematic error of the instrumentation, operated at the boundaries of operation: this last results obtained after manual tweaking are shown in Fig. 3.18a.
Moreover, linearity and TX spectrum tests were performed on this device, once it was realized that the power handling performances were interesting, as reported in Fig. 3.16. This results are really promising for these technology, displaying a real potential to meet the demanding specifications of communication network market. As follows from Sec. 1.3, the output spectrum (Fig. 3.18b) displays a significant rejection of the odd order IM products (the closest is as low as -30dBc), thanks to the differential configuration proposed in Fig. 3.7. However the rejection is not optimal, mainly for asymmetries in the circuit discussed in Fig. 3.17, and the even order IM products generated by the switches are not attenuated at all. This constitutes one of the main problems of this circuit, as the IM tones would be radiated in air, and, even if attenuated by the nonreciprocal transfer function, will be found also at the RX input.
The P1dB=28dBm displayed by this circuit (Fig. 3.18c) reveals one of the main advantages of using MEMS resonators and IC switches instead of varactors, as proposed at the beginning of this work. In fact, as long as the MEMS operates in a linear region and the GaAs switch is designed to handle enough power, this circuit will provide an overall good I/O linearity. Note that this value of P1dB is very close to the one reported in the datasheet of the switch ([63]), thus suggesting that the MEMS could handle even more power before introducing significant distortions.
As shown in Fig. 3.18, the main remaining limitation of this circuit remains the suppression

of even order IM tones. This task will be covered in the last chapter of this work, where a circuital solution is proposed to employ RF MEMS filters in conjunction with Angular Momentum Bias cores so to combine in single, miniaturized devices the functionalities required by OFDM communication systems and nonreciprocal transmission in a Quasi-LTI regime.

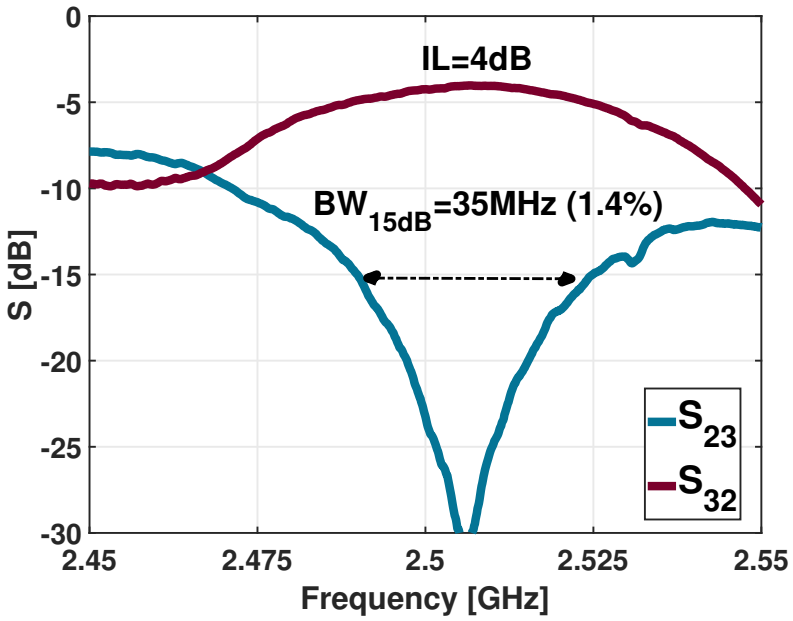

(a) *Best performances achieved with a enhanced bandwidth MIRC.*

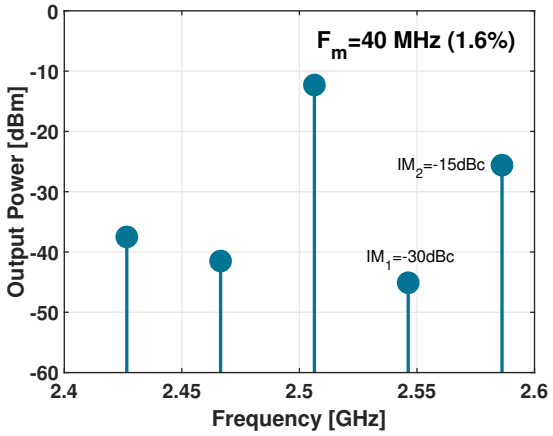

(b) *Output TX spectrum for an input power P_{in}=-10dBm.*

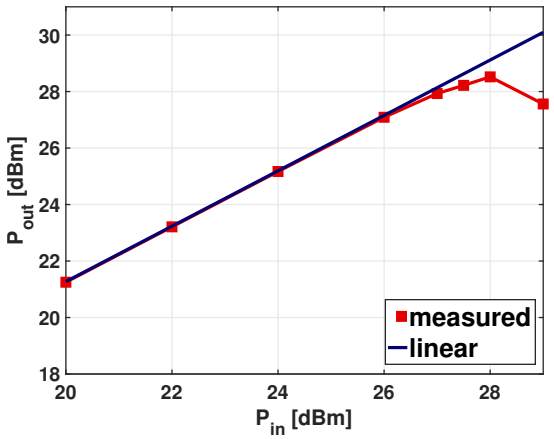

(c) *Measured P1dB performances for the MIRC.*

Fig. 3.18: *Characterization of linearity and output spectrum for the MIRC implemented with Broadcom Resonators. S-parameters are also reported for these test conditions: fractional bandwidth and operating regional (modulation frequency 1.5% and $\gamma = 0.5$ are in close proximity to the values predicted in Fig. 3.5a for a $k_t^2 \approx 2.5\%$.*

Chapter 4

Quasi LTI Channel Selective MEMS Circulator

As highlighted in Chap. 3, the main limitations of AMB circuits in practical applications, especially when the goal is to enable Full Duplex communication systems, are the output Inter Modulation(IM) tones produced by the switched-capacitor network.
Differential configurations, like the one proposed in Fig. 1.8 for varactor based implementations and the one shown in Fig. 3.12 for MEMS based implementations, strongly reduces odd-order IM tones ($\omega \pm \omega_m, \omega \pm 3\omega_m$...) but, as evident from the experimental results in Fig. 1.12, and Fig. 3.18b the first even order IM tone can be found as low as 15dBc.

It has to be noted that a perfect cancellation was predicted in [27] for the varactor excitation of Angular Momentum Bias effect, since in that case just odd order tones are excited by the sinusoidal modulation: the situation is slightly different when AMB is excited thanks to a switched capacitor modulation, that is a *square wave* modulation (Fig. 1.10).
In this chapter, a possible solution employing MEMS piezoelectric filters ([46, 58]) to minimize those distortions is presented: as will become clear, the filter will be used not only as a channel-select component, thus increasing the IM rejection, but also its poles will be subject to *spatiotemporal modulation* in the characteristic AMB fashion discussed in Chap. 1 .
When the filter is realized in MEMS technologies and high Figure of Merit (FoM) (Sec. 2.2) can be achieved, characteristic ultra low modulation frequency ω_m and low Insertion Loss (IL) can be achieved , thus preserving the features of MIRCs discussed in Chap. 3.

4.1 MEMS based Channel-Select Filters

The modeling of RF filters based on MEMS devices is a topic of interest for MEMS community ([58, 66, 67]) and it represents nowadays one of the most promising MEMS applications in RF filtering .
In many works like [58], detailed modeling of RF bandpass filters for small fractional bandwidths (2-3%) is reported, based on the so-called *ladder* filter topology (Fig. 4.1a).
Some notes about the behavior of these filters will be here reported, since their unique features, in conjunction with the details about frequency modulation in AMB circuits, will be the key to understand how Channel-Select MEMS Circulator (CMC) operates. As shown in Fig. 4.1, implementing on-chip RF filters based on MEMS resonators requires the capability of tuning the center frequency of the resonator by a quantity comparable to the typical k_t^2, tipically 2 to 7 %.
This is the main reason why lateral modes of vibration (Sec. 2.2.2) could be determinant in this context.
Typical trends and S-parameters of this class of RF filters are shown in Fig. 4.1c, as k_t^2 and Q are assumed constants for the different resonators.

Some of the main features of these filters are reported in Fig. 4.1.

50 Ω matching.

For the in-band transmission the input stage matching has an optimal value for

$$\frac{1}{\omega_0 \sqrt{C_{0,1} C_{0,2}}} = 50\Omega \tag{4.1}$$

where ω_0 is the center frequency of the bandpass, $C_{0,1}, C_{0,2}$ defined as in Fig. 4.1a.

In Band Losses & Bandwidth.

Q	**I.L**(peak)
200	2.3 dB
500	1.0 dB
1000	0.4 dB
2000	0.2dB

Tab. 4.1

When the 50 Ω condition is satisfied, the IL just depends on the FoM of the resonators, thus ultimately being limited by the *motional resistance* of the resonators. The Insertion Loss

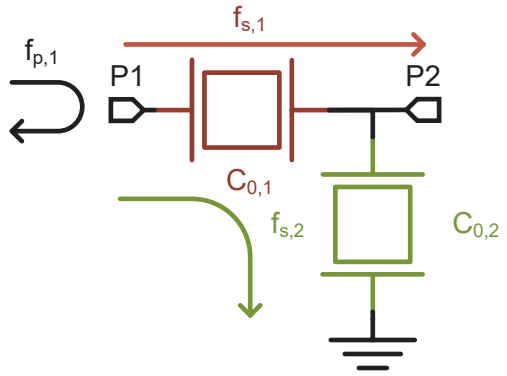

(a) *Basic block of a MEMS RF ladder filter.*

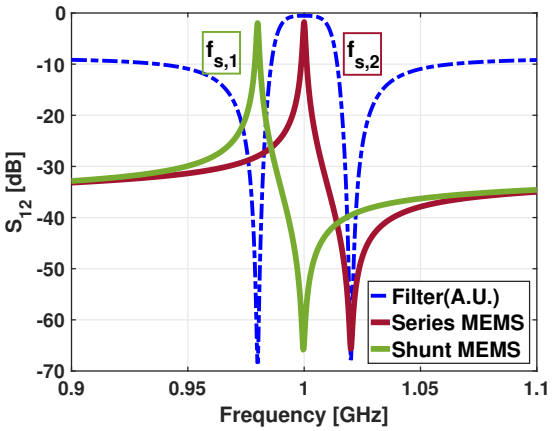

(b) *Schematic representation of MEMS resonances in Ladder Filters*

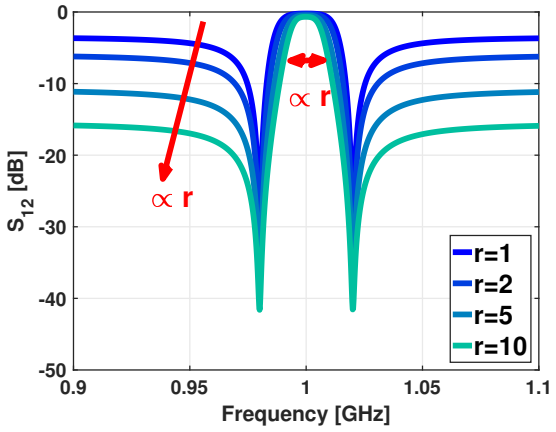

(c) *Impact of the capacitance scaling $r = C_{0,2}/C_{0,1}$ on the filter bandwidth and the out of band rejection.*

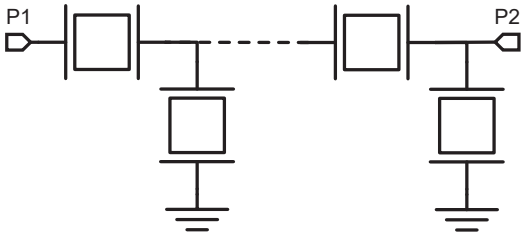

(d) *Cascading more ladder stages can further increase out of band rejection.*

Fig. 4.1: *Operation of ladder MEMS filters.$f_{s,1}$ and $f_{s,2}$ are respectively the resonance frequencies for the series and the shunt resonators, $C_{0,1}$ and $C_{0,2}$ respectively the electrostatic capacitances of the series and shunt resonators. As the ratio $r = C_{0,2}/C_{0,1}$ increases, the out-of-band rejection increases as in Eq. 4.2. The filter BW is limited by $2k_t^2$ as can be seen in Fig. 4.1b.*

(IL) is inversely proportional to the resonators Figure of Merit (FoM),for a given material and resonance mode(so a certain k_t^2), IL are inversely proportional to the resonator Q. Typical numbers for $r = 5, C_{0,1} = 1.4pF, k_t^2 = 5\%$ are reported in Tab. 4.1.

As in Fig. 4.1b, the bandwidth is limited to a fraction of $8/\pi^2 k_t^2$ (in Eq. 2.11) that is the normalized difference between the lower notch and the upper notch.

Out of band rejection. Out of band, the MEMS filter looks like a capacitors network, and it is easy to show that its response is so that:

$$S_{12}(\omega)\big|_{out} = \frac{1}{(1+r)^N} \tag{4.2}$$

Thus cascading N stages of unit identical ladder cells (like in Fig. 4.1d) it is possible to obtain arbitrary out of band rejection [58].
This choice sets a trade off with the IL of the filter, since the RF path will flow through more resonators and thus will show overall higher motional resistance R_m (Eq. 2.8).

Guard band notches. As shown in Fig. 4.1, MEMS filters show two typical notches at the edges of the TX bandwidth. The schematic in Fig. 4.1a reveals a key features of these notches: the one at the lower edge of the bandwidth corresponds to the *series* resonance of the shunt resonator, thus the impedance seen from the port approaches a *short circuit* (SC), while the one at the upper edge corresponds to the *parallel* resonance of the series resonator, thus the impedance seen from the port approaches an *open circuit* (OC) .
This feature is of main interest in the CMC design, as it will become evident in Sec. 4.2 that the SC condition can be effectively used to decouple the RF path from the IM path in the parametric circuit.

4.2 Non reciprocal filter modeling

As a first attempt to solve the problem of IM leakage to the RF ports in AMB circuits (for example in Fig. 3.7) one might add a passive, highly frequency selective two port network at each port, so to filter out the unwanted frequency components resulting from the switching network. Interestingly, this approach was found to be disastrous: no nonreciprocity is observed in a switched LC network (at least in the single ended implementation) if a passive filter is juxtaposed at the ports like in Fig. 4.2a.
The reason is that the behaviour of the system response is related to the overall impedance seen from the central node to each ground *at each single IM frequency*. It is not possible, in fact, to treat this system like an LTI system where stages can be cascaded so that their frequency response can be superimposed. Following from this argument, it is quite intuitive to observe that if no IM current can be generated and flow through the central node, no parametric modes can be excited, ultimately resulting in a reciprocal response.
At a first glance, this might seem a fundamental limit for the operation of this system, that might prevent the implementation in real case scenarios, where narrow bandwidths are required in communication channels and thus piezoelectric filters represent the natural filtering solutions at RF frequencies. It is a very common scenario to have reflective open loads in out of band filtering systems, thus no IM current could be generated.

Moreover, describing the system in Fig. 4.2a through the same analytical approach proposed in Sec. 1.2 it is not a viable solution, as too many nodes are involved in the real circuit and it would be difficult to obtain any insight from such a model.
Instead, with some algebraic manipulations a it is possible to recast the terms in the same model to find a very compact expression:

$$S_{12}(\omega) = S_{12,static}(\omega)\cdot \left\{1 + j\frac{\delta^2}{2}\left[\frac{j+\sqrt{3}}{\delta^2 + 4C_{ave}^2\omega^2 Z_{br}(\omega)Z_{br}(\omega-\omega_m)} + \frac{j-\sqrt{3}}{\delta^2 + 4C_{ave}^2\omega^2 Z_{br}(\omega)Z_{br}(\omega+\omega_m)}\right]\right\} \tag{4.3a}$$

$$S_{21}(\omega) = S_{21,static}(\omega)\cdot \left\{1 + j\frac{\delta^2}{2}\left[\frac{j+\sqrt{3}}{\delta^2 + 4C_{ave}^2\omega^2 Z_{br}(\omega)Z_{br}(\omega+\omega_m)} + \frac{j-\sqrt{3}}{\delta^2 + 4C_{ave}^2\omega^2 Z_{br}(\omega)Z_{br}(\omega-\omega_m)}\right]\right\} \tag{4.3b}$$

In these equations, $\delta = \Delta C/C_{ave}$ is the so called *modulation depth*, it has the same meaning as in Eq. 1.9 and it is essentially the induced capacitance variation on the varactor, and C_{ave} is the unmodulated capacitance. ω is the input and output frequency of the linearized system, for which a nonreciprocal scattering parameter (S_{12},S_{21}) characterization is given. $Z_{br}(\omega \pm \omega_m)$ is the *branch* impedance, looking from the central node to each ground as in

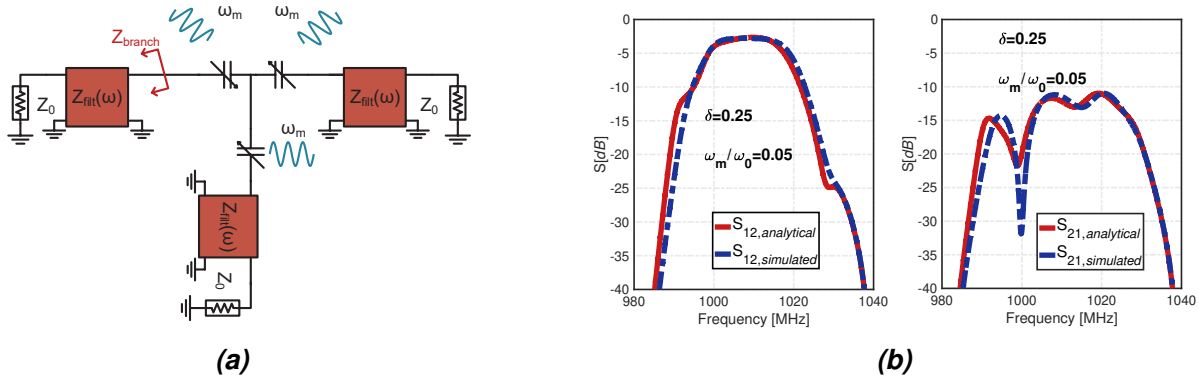

(a) ***(b)***

Fig. 4.2: *In Fig. 4.2a the generalized AMB schematic is presented. In Fig. 4.2b a validation of he proposed analytical model with Harmonic Balance simulations shows very good agreement for* $\delta = 0.25$.

Fig. 4.2, and $S_{12,static} = S_{21,static}$ is the non modulated response of the system (which is the response for $\delta = 0$).

No easy espression is here reported for the reflection coefficient S_{11}, but in this case it is not indeed a main concern: in fact, as long as no significant IM power is lost and low IL is expected, the input reflection is expected to be low. Moreover, all of the filtering systems that will be considered are statically 50 Ω matched.
The model here shown is of great help in understanding the behaviour of this system, and reveals the *parametric* effect induced by the varactor sinusoidal excitation.
Among the observations that could be done on those formulas, it is worth noting at this point at least the following:

- This is an extended (yet more compact and useful) model for the system described in Sec. 1.2, which is a special case off Eq. 4.3 when

$$Z_{br}(\omega) = j\left(\frac{\omega}{\omega_0^2 C_{ave}} - \frac{1}{\omega C_{ave}}\right) + Z_0 \tag{4.4}$$

  thus completing the analytical modeling proposed in Chap. 1.

- As expected from qualitative observations, for $Z_{br} \to \infty$ no nonreciprocal response can be achieved: this means that *at least* one IM product has to flow through the central node.

- One could recognize a *generalized* loaded Q for the dynamic system in the factors $C_{ave}\omega^2 Z_{br}(\omega \pm \omega_m)$.

- $S_{12,static}$ clearly depends also on $Z_{br}(\omega)$: this confirms that *all* of the static network connected to the central note can be subject to AMB modulation.

This model opens the way to a generalization of the Angular Momentum Bias circuit to a whole new class of circuits, where for instance *multi pole* excitation of nonreciprocal response can be achieved.
Moreover, when having access to MEMS technologies to obtain large out of band rejection (as in Eq. 4.2) and the nonreciprocal response can be controlled thanks to characteristic *high-Q* notches, strong nonreciprocity can be achieved with ultra-low modulation frequency, and at the same time very good IM rejection is expected even in the case where the varactor is replaced by a switch.
Thus the MEMS ladder filter structures described in Sec. 4.1 are perfect candidates for the following reasons:

- Fractional bandwidths in the order of k_t^2 percents are compatible with ultra-low modulation frequencies (of the same order of k_t^2.
- Out-of-band rejection up to 50dB can be achieved with mm^2 area consumption ([68]).

A possible design is proposed in Fig. 4.3, correlated with a schematic representation of the mixing currents in the dynamic operation of the circuit. In the following sections simulations results based on that filter design will be discussed, and an experimental result obtained using Surface Acoustic Wave (SAW) filter and switched capacitors will be presented.

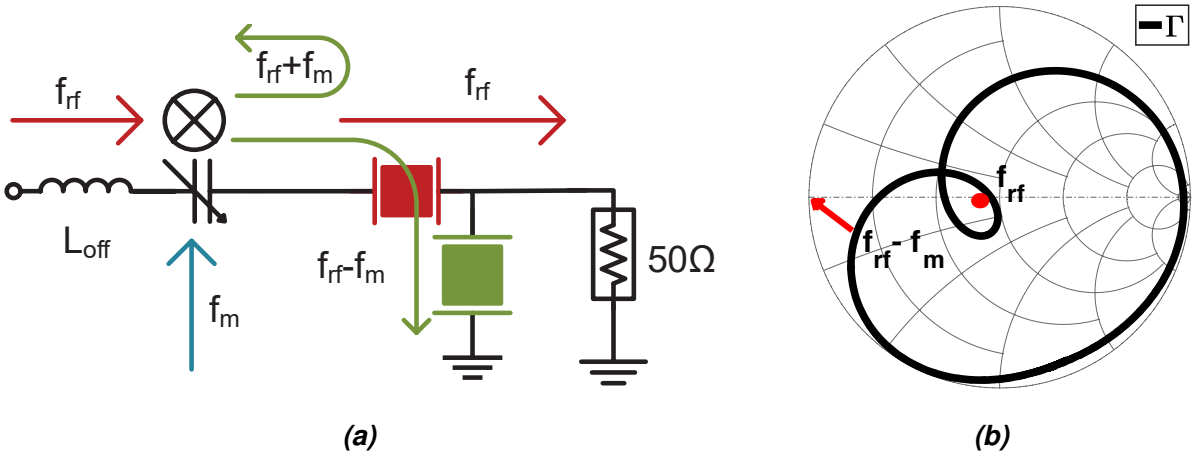

Fig. 4.3: *Frequency conversion in AMB circuits when ladder filter poles are introduced. In Fig. 4.3a the IM path and RF path is highlighted: thanks to the MEMS notches, just the RF path is found at the output, while the first IM tones are confined within the AMB core. In Fig. 4.3b instead, static S_{11} for a 2 ladder stage filter is displayed on the Smith chart: the the optimal f_m approaches the condition of minimal impedance at the IM frequency.*

4.3 Simulations and Experimental Results

A first question around this system regards the equivalence between circuits where Angular Momentum Bias is excited respectively through varactors or switched capacitor networks like in Fig. 1.10.

Preliminary simulations were run to confirm this. Results are reported in Fig. 4.5. Regarding the simulation setup, similar consideration as in Sec. 3.2 can be done.
These results show reasonably similar trends in the two cases, and minimal extra-IL (less than 1dB) are associated to the switching network (at least as long as ideal switches are considered). This is consistent with the analysis performed in Sec. 4.2: if losses are not associated to reactive components and IM products, then they will not be expected in this stage of the simulations.
The filter was modeled as a single stage ladder with a $C_0 = 3pF$ and a ratio $r = 1$ to ensure minimal losses. Note that for the TX RF path during the dynamic operation the filter structure is not symmetric, thus the response will not resemble the S_{21} in the passive ladder filter. However isolation peaks are significantly lower in the switched capacitor case, while the bandwidths are comparable.

However, the output spectrum for these systems still shows $\approx 25dBc$ of even IM tones, due essentially to poor out-of-band rejection.
In fact, as r is increased, the motional resistance increases according to Eq. 2.8 thus compromising the IL of the CMC.

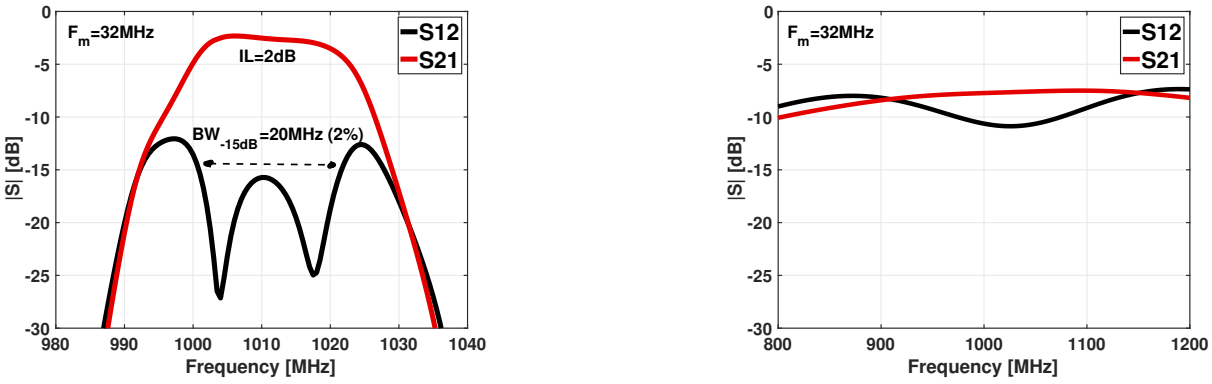

Fig. 4.4: *Harmonic Balance Simulations of varactor-excitated AMB CMC (Fig. 4.4a). A comparison with the same circuit when the filter is removed (Fig. 4.4b) stresses the point that when the modulation frequency F_m approaches the condition reported in Fig. 4.3b strong nonreciprocity can be achieved thanks to MEMS multi-pole high Q modulation, in a regime where the LC counterpart would be strongly suboptimal.*

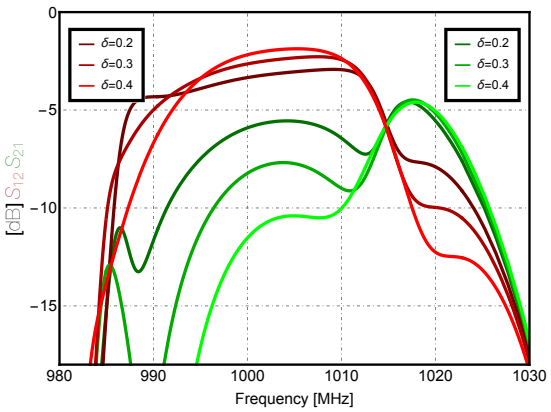

(a) *Analitycal results.*

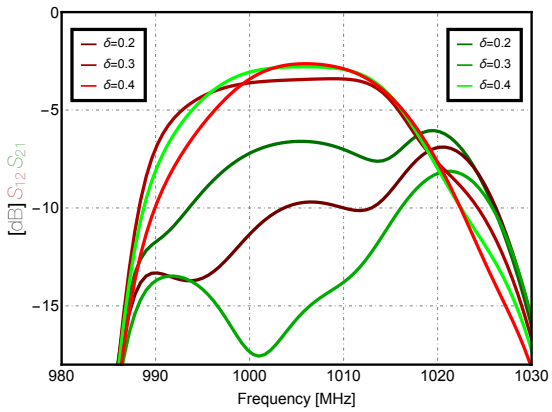

(b) *Harmonic Balance results.*

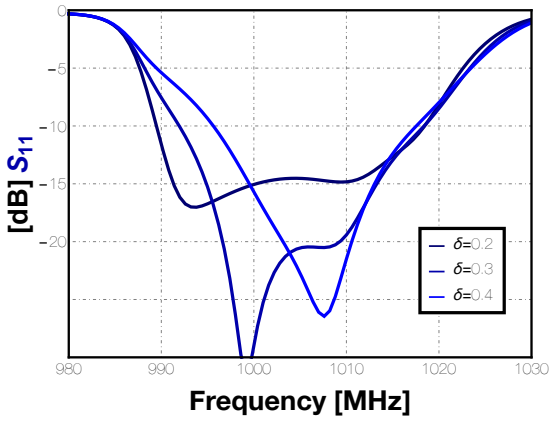

(c) *Harmonic Balance solutions for S_{11} in switched capacitor AMB topology.*

Fig. 4.5: *Comparison of analytical results for varactor excitation in Fig. 4.5a with simulated switched capacitor system in Fig. 4.5b. While trends looks similar, nonreciprocal contrast in switched capacitor simulation is smaller.*
Bandwidths are instead comparable, and so are losses.
Note instead that the input matching is overall lower than 15dB across different modulation depths δ, confirming the qualitative arguments in the discussion in Sec. 4.2.

To prove the point that very low Total Harmonic Distortion can be achieved, a circuit based on Fig. 4.2 was implemented on PCB. (Fig. 4.6b)
Note that for this implementation a Surface Acoustic Wave filter was chosen operating at 870MHz, with a low fractional bandwidth ($\approx 1\%$) due to typical low electromechanical coupling k_t^2 of these technology. This filter was chosen for its out-of-band rejection approaching 50dB, even with a IL$\approx 2dB$.
For the switched capacitor network, a commercial GaAs reflective open SP2T RF switch (HMC194A from Analog Devices) ([62]) was used.
The custom microstrip PCB was implemented (Fig. 4.6b) so to minimize the spacing between the modulation network and the RF ports. Most of the area is occupied by the switch and thin lines were designed so to absorb the small inductance required by the design.
However, the on-state GaAs non idealities were found to be very detrimental for the dynamic operation of the switched capacitor network: both the parasitic capacitances to ground and the series inductance of the switch are degrading d the IL of the circuit resulting in 3dB extra IL with respect to the initial simulations. For references on the switch modeling, see Sec. 3.2.
All the experimental results are shown in Fig. 4.7. As a result of the experimental modulation frequency F_m sweep (Fig. 4.7c and Fig. 4.7d) it is clear that an optimum of 15MHz (1.7% of RF frequencies) will result both in the minimum IL and the maximum of nonreciprocal contrast.
At the same time this condition will guarantee the minimum Total Harmonic Distortion (THD) condition (Fig. 4.7d) as it approaches 40dB (0.01%).
More than 10 dB of contrast between the counter propagating RF waves were observed, with an 8dB peak Insertion Loss measured across the bandwidth of the SAW filter. Except for the extra losses ($\simeq 3dB$) due to switches packaging and poor PCB design, all of the datas confirms the trends discussed in Sec. 4.2 and simulations done with the static filter S-parameters.

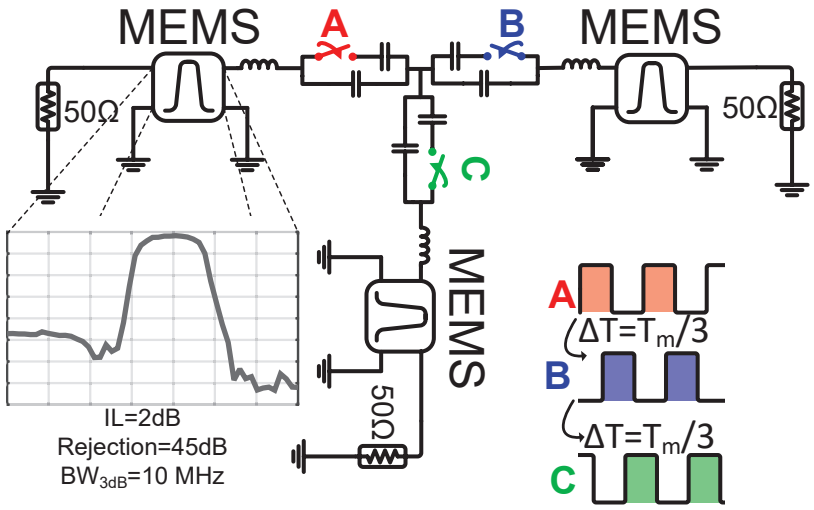

(a) *Schematic of the Quasi LTI Magnetless circulator.*

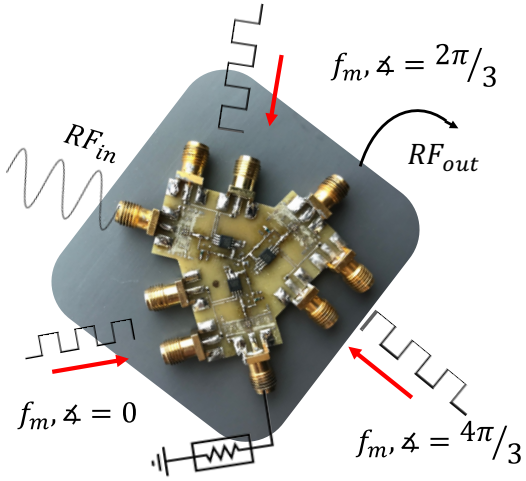

(b) *Picture of the realized microstrip PCB.*

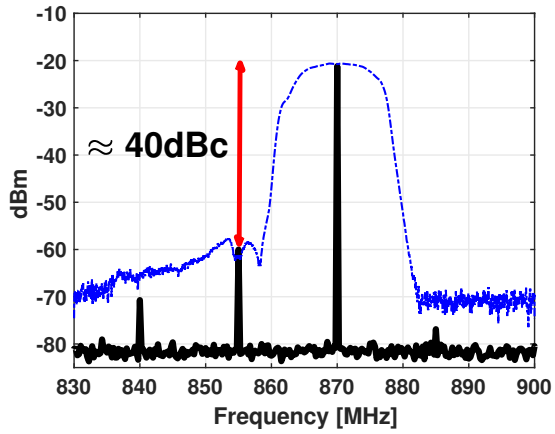

(c) *Measured output spectrum for* $P_{in} = -10dBm$.

Fig. 4.6

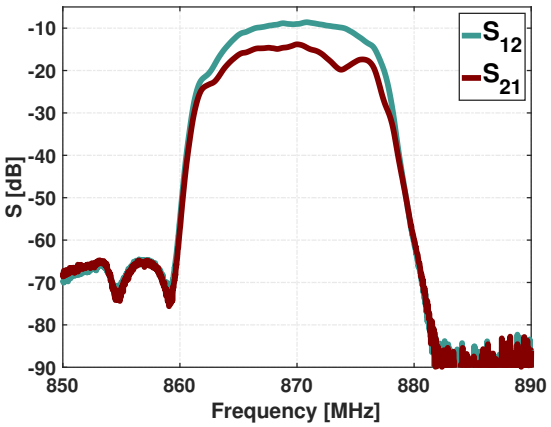

(a) *Nonreciprocal transmission in the implemented CMC.*

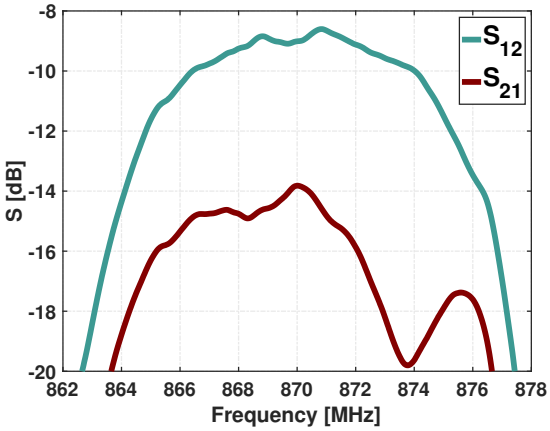

(b) *Zoom of the CMC transfer function.*

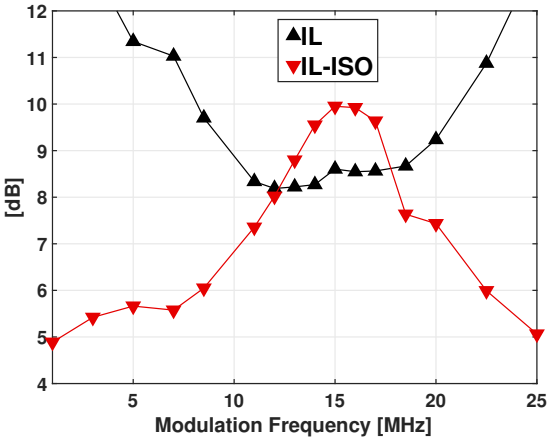

(c) *Insertion Loss (IL) and contrast (IL-ISO) peaks for different F_m.*

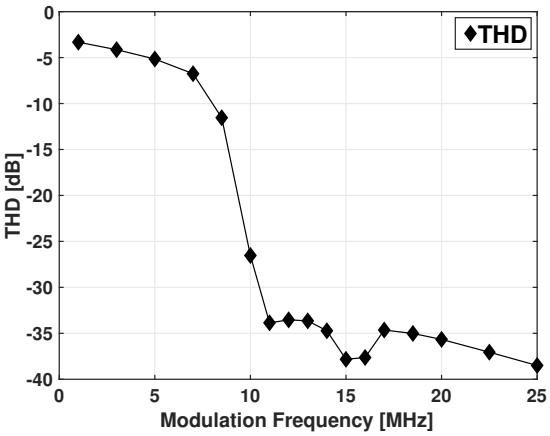

(d) *THD of the circuit for different modulation frequencies F_m.*

Fig. 4.7

Conclusion

A detailed analysis of the Angular Momentum Bias concept was covered as a strategy to achieve nonreciprocal transmission in resonant magnetless three ports networks. All the critical aspects of practical implementation at RF frequencies were presented, as well as solutions to overcome those limitations thanks to switched capacitors networks and MEMS resonators.
For this purpose, custom MEMS resonators were designed at 1GHz and fabricated for this purposes. Nonreciprocity was demostrated using those components with sub mm^2 footprint. Experimental proofs show more than 20dB of contrast, 1.5% fractional bandwidth, good agreement with circuit modeling and simulations.
Moreover, a novel approach was introduced and experimentally demostrated to further overcome the output distortion of these networks, thanks to the use of MEMS resonators arranged in ladder filter structure.
This work, however, covers just the first steps of the exploration of this circuit.
To reach better performances, next steps of circuit optimization include:

MEMS and switches co-design.

The main practical limitations to circuit loss for this work was the lack of access to integrated technologies for custom CMOS/GaAs switch design and simulation. By having access to those, PCB implementation related issues would be removed, more reliable simulation can be performed and even more appealing miniaturized circuits can be implemented.

Custom high power handling MEMS resonator design.

Further work on lateral mode resonators can lead to a new state of the art in power handling structures for single-chip ,multi-frequency channel select miniaturized circulators.

Network optimization.

A generalized modelfo for arbitrary three port networks was proposed. Numerical and analytical efforts will be investigated starting from that model in order to further optimize nonreciprocal contrast in multi-pole MEMS circulators.

List of Figures

List of Tables

Bibliography

[1] R. Takei and T. Mizumoto, "Design and simulation of silicon waveguide optical circulator employing nonreciprocal phase shift," *Japanese Journal of Applied Physics*, vol. 49, no. 5R, p. 052 203, 2010. [Online]. Available: http://stacks.iop.org/1347-4065/49/i=5R/a=052203.

[2] E. Schloemann, "Integrated dc/rf design of dual-ferrite circulators," *IEEE Transactions on Magnetics*, vol. 33, no. 5, pp. 3430–3432, Sep. 1997, ISSN: 0018-9464. DOI: 10.1109/20.617967.

[3] B. v. Liempd, B. Hershberg, K. Raczkowski, S. Ariumi, U. Karthaus, K. F. Bink, and J. Craninckx, "2.2 a +70dbm iip3 single-ended electrical-balance duplexer in 0.18um soi cmos," in *2015 IEEE International Solid-State Circuits Conference - (ISSCC) Digest of Technical Papers*, 2015, pp. 1–3.

[4] D. Bharadia, E. McMilin, and S. Katti, "Full duplex radios," *SIGCOMM Comput. Commun. Rev.*, vol. 43, no. 4, pp. 375–386, Aug. 2013, ISSN: 0146-4833. DOI: 10.1145/2534169.2486033. [Online]. Available: http://doi.acm.org/10.1145/2534169.2486033.

[5] T. Dinc, A. Chakrabarti, and H. Krishnaswamy, "A 60 ghz cmos full-duplex transceiver and link with polarization-based antenna and rf cancellation," *IEEE Journal of Solid-State Circuits*, vol. 51, no. 5, pp. 1125–1140, 2016, ISSN: 0018-9200. DOI: 10.1109/JSSC.2015.2507367.

[6] A. Setiawan, Y. Y. Maulana, Y. Sulaeman, T. Praludi, and Y. Taryana, "Design of 3 ghz stripline ferrite circulator for radar applications," in *2017 International Conference on Radar, Antenna, Microwave, Electronics, and Telecommunications (ICRAMET)*, 2017, pp. 154–157.

[7] D. Pozar, *Microwave Engineering, 4th Edition*. Wiley, 2011, ISBN: 9781118213636.

[8] N. Sturcken, R. Davies, H. Wu, M. Lekas, K. Shepard, K. W. Cheng, C. C. Chen, Y. S. Su, C. Y. Tsai, K.-J. Wu, J. Y. Wu, Y. C. Wang, K. C. Liu, C. C. Hsu, C. L. Chang, W. C. Hua, and A. Kalnitsky, "Magnetic thin-film inductors for monolithic integration with cmos," *2015 IEEE International Electron Devices Meeting (IEDM)*, pp. 11.4.1–11.4.4, 2015.

[9] S. Tanaka, N. Shimomura, and K. Ohtake, "Active circulators & the realization of circulators using transistors," *Proceedings of the IEEE*, vol. 53, no. 3, pp. 260–267, Mar. 1965, ISSN: 0018-9219. DOI: 10.1109/PROC.1965.3683.

[10] G. Carchon and B. Nanwelaers, "Power and noise limitations of active circulators," *IEEE Transactions on Microwave Theory and Techniques*, vol. 48, no. 2, pp. 316–319, Feb. 2000, ISSN: 0018-9480. DOI: 10.1109/22.821785.

[11] S. Qin and Y. E. Wang, "Broadband parametric circulator with balanced monolithic integrated distributedly modulated capacitors (dmc)," in *2016 IEEE MTT-S International Microwave Symposium (IMS)*, May 2016, pp. 1–4. DOI: 10.1109/MWSYM.2016.7540321.

[12] S. Qin, Q. Xu, and Y. E. Wang, "Nonreciprocal components with distributedly modulated capacitors," *IEEE Transactions on Microwave Theory and Techniques*, vol. 62, no. 10, pp. 2260–2272, Oct. 2014, ISSN: 0018-9480. DOI: 10.1109/TMTT.2014.2347935.

[13] T. Dinc, A. Nagulu, and H. Krishnaswamy, "A millimeter-wave non-magnetic passive soi cmos circulator based on spatio-temporal conductivity modulation," *IEEE Journal of Solid-State Circuits*, vol. 52, no. 12, pp. 3276–3292, Dec. 2017, ISSN: 0018-9200. DOI: 10.1109/JSSC.2017.2759422.

[14] N. Reiskarimian, J. Zhou, and H. Krishnaswamy, "A cmos passive lptv nonmagnetic circulator and its application in a full-duplex receiver," *IEEE Journal of Solid-State Circuits*, vol. 52, no. 5, pp. 1358–1372, May 2017, ISSN: 0018-9200. DOI: 10.1109/JSSC.2017.2647924.

[15] M. G. Rinaldi, C. Zuniga, and G. A. Piazza, "5-10 ghz aln contour-mode nanoelectromechanical resonators," *2009 IEEE 22nd International Conference on Micro Electro Mechanical Systems*, pp. 916–919, 2009.

[16] R. Fleury, D. L. Sounas, C. F. Sieck, M. R. Haberman, and A. Alù, "Sound isolation and giant linear nonreciprocity in a compact acoustic circulator," *Science*, vol. 343, no. 6170, pp. 516–519, 2014, ISSN: 0036-8075. DOI: 10.1126/science.1246957. eprint: http://science.sciencemag.org/content/343/6170/516.full.pdf. [Online]. Available: http://science.sciencemag.org/content/343/6170/516.

[17] D. L. Sounas, C. Caloz, and A. Alù, "Giant non-reciprocity at the subwavelength scale using angular momentum-biased metamaterials," *Nature Communications*, vol. 4, Sep. 2013, Article. [Online]. Available: http://dx.doi.org/10.1038/ncomms3407.

[18] D. L. Sounas and A. Alù, "Angular-momentum-biased nanorings to realize magnetic-free integrated optical isolation," *ACS Photonics*, vol. 1, no. 3, pp. 198–204, Mar. 2014. DOI: 10.1021/ph400058y. [Online]. Available: https://doi.org/10.1021/ph400058y.

[19] *High power circulator with 20 db isolation from 380 mhz to 460 mhz, 1000 watts and sma female*, Pasternak, 2016. [Online]. Available: hhttps://www.pasternack.com/images/ProductPDF/PE8422.pdf.

[20] *Rf high-frequency inductors*, CoilCraft, 2015. [Online]. Available: https://www.coilcraft.com/pdfs/0403hq.pdf.

[21] R. E. Collin, *Field Theory of Guided Wave*. Jan. 1991, vol. 14.

[22] H. Bhugra and G. Piazza, *Piezoelectric MEMS Resonators*, ser. Microsystems and Nanosystems. Springer International Publishing, 2017, ISBN: 9783319286884. [Online]. Available: https://books.google.com/books?id=hYLgDQAAQBAJ.

[23] R. Abdolvand, B. Bahreyni, J. E. .-.-Y. Lee, and F. Nabki, "Micromachined resonators: A review," *Micromachines*, vol. 7, no. 9, 2016, ISSN: 2072-666X. DOI: 10.3390/mi7090160. [Online]. Available: http://www.mdpi.com/2072-666X/7/9/160.

[24] N. A. Estep, D. L. Sounas, and A. Alù, "Magnetless microwave circulators based on spatiotemporally modulated rings of coupled resonators," *IEEE Transactions on Microwave Theory and Techniques*, vol. 64, no. 2, pp. 502–518, Feb. 2016, ISSN: 0018-9480. DOI: 10.1109/TMTT.2015.2511737.

[25] A. Kord, D. L. Sounas, and A. Alu, "Magnet-Less Circulators Based on Spatiotemporal Modulation of Bandstop Filters in a Delta Topology," *IEEE Transactions on Microwave Theory Techniques*, vol. 66, pp. 911–926, Feb. 2018. DOI: 10.1109/TMTT.2017.2757470. arXiv: 1709.08131.

[26] N. A. Estep, D. Sounas, and A. Alu, "On-chip non-reciprocal components based on angular-momentum biasing," pp. 1–4, May 2015.

[27] A. Kord, D. L. Sounas, and A. Alù, "Differential magnetless circulator using modulated bandstop filters," in *2017 IEEE MTT-S International Microwave Symposium (IMS)*, Jun. 2017, pp. 384–387. DOI: 10.1109/MWSYM.2017.8058574.

[28] H. D'Angelo, *Linear time-varying systems: analysis and synthesis*, ser. Allyn and Bacon series in electrical engineering. Allyn and Bacon, 1970. [Online]. Available: https://books.google.it/books?id=yaE8AAAAIAAJ.

[29] B. R. Gray, "Design of rf and microwave parametric amplifiers and power upconverters," PhD thesis, Georgia Institute of Technology, Canada, 2012. [Online]. Available: https://smartech.gatech.edu/bitstream/handle/1853/43613/Gray_Blake_R_201205_phd.pdf?sequence=1&isAllowed=y.

[30] T. Dinc, M. Tymchenko, A. Nagulu, D. Sounas, A. Alu, and H. Krishnaswamy, "Synchronized conductivity modulation to realize broadband lossless magnetic-free nonreciprocity," *Nature Communications*, vol. 8, no. 1, p. 795, 2017, ISSN: 2041-1723. DOI: 10.1038/s41467-017-00798-9. [Online]. Available: https://doi.org/10.1038/s41467-017-00798-9.

[31] M. M. Biedka, R. Zhu, Q. M. Xu, and Y. E. Wang, "Ultra-wide band non-reciprocity through sequentially-switched delay lines," *Sci Rep*, vol. 7, p. 40 014, Jan. 2017, 28059132[pmid], ISSN: 2045-2322. DOI: 10.1038/srep40014. [Online]. Available: http://www.ncbi.nlm.nih.gov/pmc/articles/PMC5216411/.

[32] P. Gray, *Analysis and Design of Analog Integrated Circuits, 5th Edition*. Wiley Global Education, 2009, ISBN: 9781118313091. [Online]. Available: https://books.google.com/books?id=YRAcAAAAQBAJ.

[33] M. Roy, R. J. Ward, and J. A. Higgins, "Sic varactor based tunable filters with enhanced linearity," in *2008 IEEE Topical Meeting on Silicon Monolithic Integrated Circuits in RF Systems*, 2008, pp. 163–166.

[34] A. Kord, D. L. Sounas, and A. Alù, "Pseudo-linear time-invariant magnetless circulators based on differential spatiotemporal modulation of resonant junctions," *IEEE Transactions on Microwave Theory and Techniques*, vol. 66, pp. 2731–2745, 2018.

[35] C. Zuo, N. Sinha, J. V. d. Spiegel, and G. Piazza, "Multi-frequency pierce oscillators based on piezoelectric aln contour-mode mems resonators," in *2008 IEEE International Frequency Control Symposium*, 2008, pp. 402–407.

[36] M. A. Ahmad and S. Ahmed, "Heart-rate and pressure-rate determination using piezoelectric sensor from the neck," in *2017 4th IEEE International Conference on Engineering Technologies and Applied Sciences (ICETAS)*, 2017, pp. 1–5.

[37] S. Lee, A. Reuveny, J. Reeder, S. Lee, H. Jin, Q. Liu, T. Yokota, T. Sekitani, T. Isoyama, Y. Abe, Z. Suo, and T. Someya, "A transparent bending-insensitive pressure sensor," *Nature Nanotechnology*, vol. 11, p. 472, Jan. 2016, Article. [Online]. Available: http://dx.doi.org/10.1038/nnano.2015.324.

[38] R. Corman, O. Nedelcu, and D. Dobrescu, "Design and simulation of a piezoelectric sensor with applications in image stabilization," in *2016 International Semiconductor Conference (CAS)*, 2016, pp. 85–88.

[39] K.-W. Chen, J.-S. Chen, Y.-L. Yeh, Y.-D. Chen, and C.-L. Yang, "Self-powered batteryless wireless communication systems for internet of things based on piezoelectric energy harvester," in *2015 IEEE MTT-S International Microwave Symposium*, 2015, pp. 1–3.

[40] X. Jiang, H. Y. Tang, Y. Lu, E. J. Ng, J. M. Tsai, B. E. Boser, and D. A. Horsley, "Ultrasonic fingerprint sensor with transmit beamforming based on a pmut array bonded to cmos circuitry," *IEEE Transactions on Ultrasonics, Ferroelectrics, and Frequency Control*, vol. 64, no. 9, pp. 1401–1408, 2017, ISSN: 0885-3010. DOI: 10.1109/TUFFC.2017.2703606.

[41] C. Gould and R. Edwards, "Review on micro-energy harvesting technologies," in *2016 51st International Universities Power Engineering Conference (UPEC)*, 2016, pp. 1–5.

[42] A. Ledoux, “Theory of piezoelectric materials and their applications in civil engineering,” PhD thesis, Massachusetts Institute of Technology, USA, 2011. [Online]. Available: https://dspace.mit.edu/handle/1721.1/66839.

[43] H. Bhugra and G. Piazza, *Piezoelectric MEMS Resonators*, ser. Microsystems and Nanosystems. Springer International Publishing, 2017, ISBN: 9783319286884. [Online]. Available: https://books.google.com/books?id=hYLgDQAAQBAJ.

[44] N. Bassiri-Gharb, “Piezoelectric and acoustic materials for transducer applications,” in, A. Safari and E. K. Akdogan, Eds. Boston, MA: Springer US, 2008, ch. Piezoelectric MEMS: Materials and Devices, pp. 413–430, ISBN: 978-0-387-76540-2. [Online]. Available: https://doi.org/10.1007/978-0-387-76540-2_20.

[45] C. Cassella, G. Chen, Z. Qian, G. Hummel, and M. Rinaldi, “Cross-sectional lamé mode ladder filters for uhf wideband applications,” *IEEE Electron Device Letters*, vol. 37, no. 5, pp. 681–683, 2016.

[46] G. Chen, C. Cassella, T. Wu, and M. Rinaldi, “Single-chip multi-frequency wideband filters based on aluminum nitride cross-sectional lamé mode resonators with thick and apodized electrodes,” in *2018 IEEE Micro Electro Mechanical Systems (MEMS)*, 2018, pp. 775–778.

[47] R. Ruby, P. Bradley, J. Larson, Y. Oshmyansky, and D. Figueredo, “Ultra-miniature high-q filters and duplexers using fbar technology,” in *2001 IEEE International Solid-State Circuits Conference. Digest of Technical Papers. ISSCC (Cat. No.01CH37177)*, 2001, pp. 120–121.

[48] Y. Yang, A. Gao, R. Lu, and S. Gong, “5 ghz lithium niobate mems resonators with high fom of 153,” in *2017 IEEE 30th International Conference on Micro Electro Mechanical Systems (MEMS)*, 2017, pp. 942–945.

[49] M. Rinaldi, C. Zuniga, C. Zuo, and G. Piazza, “Ultra-thin super high frequency two-port aln contour-mode resonators and filters,” in *TRANSDUCERS 2009 - 2009 International Solid-State Sensors, Actuators and Microsystems Conference*, 2009, pp. 577–580.

[50] J. Segovia-Fernandez, M. Cremonesi, C. Cassella, A. Frangi, and G. Piazza, “Anchor losses in aln contour mode resonators,” *Journal of Microelectromechanical Systems*, vol. 24, no. 2, pp. 265–275, 2015, ISSN: 1057-7157. DOI: 10.1109/JMEMS.2014.2367418.

[51] Q. Chen, “Fabrication and characterization of aln thin film bulk acoustic wave resonator,” PhD thesis, Sep. 2006. [Online]. Available: http://d-scholarship.pitt.edu/8460/.

[52] M. A. Ahmad and R. Plana, “Piezoelectric coefficients of thin film aluminum nitride characterizations using capacitance measurements,” *IEEE Microwave and Wireless Components Letters*, vol. 19, no. 3, pp. 140–142, 2009, ISSN: 1531-1309. DOI: 10.1109/LMWC.2009.2013682.

[53] *Measurements of piezoelectric coefficient d33 of lead zirconate titanate thin films using a mini force hammer*, 2013. [Online]. Available: https://depts.washington.edu/solgel/documents/pub_docs/journal_docs/2013/VIB-11-1084_Published.pdf.

[54] R. S. Weis and T. K. Gaylord, "Lithium niobate: Summary of physical properties and crystal structure," *Applied Physics A*, vol. 37, no. 4, pp. 191–203, Aug. 1985, ISSN: 1432-0630. DOI: 10.1007/BF00614817. [Online]. Available: https://doi.org/10.1007/BF00614817.

[55] H. Campanella, "Tunable fbars: Frequency tuning mechanisms," in *The 40th European Microwave Conference*, 2010, pp. 795–798.

[56] *Fbar filter*, https://www.qorvo.com/products/d/da006106.

[57] B. Razavi, *RF Microelectronics*. Upper Saddle River, NJ, USA: Prentice-Hall, Inc., 1998, ISBN: 0-13-887571-5.

[58] G. Piazza, P. J. Stephanou, and A. P. Pisano, "Single-chip multiple-frequency aln mems filters based on contour-mode piezoelectric resonators," *Journal of Microelectromechanical Systems*, vol. 16, no. 2, pp. 319–328, 2007, ISSN: 1057-7157. DOI: 10.1109/JMEMS.2006.889503.

[59] J. D. Larson, P. D. Bradley, S. Wartenberg, and R. C. Ruby, "Modified butterworth-van dyke circuit for fbar resonators and automated measurement system," in *2000 IEEE Ultrasonics Symposium. Proceedings. An International Symposium (Cat. No.00CH37121)*, vol. 1, 2000, 863–868 vol.1.

[60] Keysight, *Switchv (voltage controlled switch)*, Update, 2009. [Online]. Available: http://edadocs.software.keysight.com/pages/viewpage.action?pageId=5509000.

[61] P. M. Smith, "Saw devices for communications applications," *Canadian Journal of Electrical and Computer Engineering*, vol. 15, no. 3, pp. 97–100, 1990, ISSN: 0840-8688. DOI: 10.1109/CJECE.1990.6591466.

[62] A. Devices, *Hmc194a rf switch*, Datasheet, 2017. [Online]. Available: http://www.analog.com/media/en/technical-documentation/data-sheets/hmc194a.pdf.

[63] MAcom, *Maswss0166rf switch*, Datasheet, 2017. [Online]. Available: http://cdn.macom.com/datasheets/MASWSS0166.pdf.

[64] Skyworks, *As179-92lf rf switch*, Datasheet, 2017. [Online]. Available: http://www.skyworksinc.com/uploads/documents/AS179_92LF_200176H.pdf.

[65] *Broadcom inc*. [Online]. Available: https://www.broadcom.com/.

[66] G. M. Rebeiz, *RF MEMS: theory, design, and technology*. John Wiley & Sons, 2004.

[67] G. M. Rebeiz, K. Entesari, I. C. Reines, S. j. Park, M. A. El-tanani, A. Grichener, and A. R. Brown, "Tuning in to rf mems," *IEEE Microwave Magazine*, vol. 10, no. 6, pp. 55–72, 2009, ISSN: 1527-3342. DOI: 10.1109/MMM.2009.933592.

[68] Qualcomm, *B4316 saw filter*, Datasheet. [Online]. Available: https://en.rf360jv.com/inf/40/ds/ae/B4316.pdf.